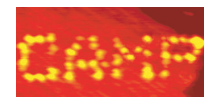

A Closer Look at the TiO₂(110) Surface with STM

Anders Rønnaau

Center for Atomic-scale Materials Physics
Interdisciplinary Nanoscience Center
Department of Physics and Astronomy
University of Aarhus, Denmark

PhD thesis
July 2003

This thesis is submitted to the Faculty of Science at the University of Aarhus, Denmark, in order to fulfill the requirements for obtaining the PhD degree in Applied Physics. The studies have been carried out under the supervision of Prof. Flemming Besenbacher in the scanning tunneling microscopy group at the Department of Physics and Astronomy from January 2001 to July 2003. The thesis is submitted one year before planned with the full acceptance of Prof. Besenbacher.



Contents

Summary	vii
List of Publications	ix
1 Introduction	1
1.1 Introduction	2
1.2 Motivation	2
1.3 Outline	3
2 Scanning Tunneling Microscopy	5
2.1 Introduction	6
2.2 Basic Principles of STM	6
2.3 The Aarhus STM	8
2.4 Theory of STM	9
2.5 Imaging Adsorbates	10
2.6 Working with Ultra High Vacuum	12
2.7 Alternative Experimental Methods	12
3 Rutile Titanium Dioxide	15
3.1 Introduction	16
3.2 Bulk Rutile TiO ₂	16
3.2.1 Geometric Structure	17
3.2.2 Electronic Structure	17
3.2.3 Bulk Defects	19
3.3 The Rutile TiO ₂ (110) Surface	19
3.3.1 Defects on the TiO ₂ (110) surface	20
3.3.2 Bridging Oxygen Vacancies	20
3.3.3 Preparation of the Surface	21
3.4 STM on TiO ₂ (110)	21
3.5 Density Functional Theory on TiO ₂ (110)	23
3.6 Adsorption of Small Molecules on TiO ₂ (110)	24

3.6.1	H ₂ and H	25
3.6.2	O ₂ and O	25
3.6.3	H ₂ O and OH	26
3.6.4	CO	27
4	Oxygen Vacancy Diffusion on TiO₂(110)	29
4.1	Introduction	30
4.1.1	Room Temperature Observations	30
4.1.2	Low Temperature Observations	32
4.2	Diffusion Mechanism	35
4.3	Conclusion	38
5	Vacancy-Vacancy Interactions on TiO₂(110)	39
5.1	Introduction	40
5.2	The Pair Distribution	41
5.3	Static Distribution	43
5.4	The Effective Potential	45
5.4.1	Vacancy Coverage	45
5.5	Monte Carlo Simulations	46
5.6	The Pair Potential	50
5.7	Surface Energy	53
5.8	DFT Calculations	53
5.9	Conclusion	54
6	Au on TiO₂	57
6.1	Motivation	58
6.2	Growth of Au Clusters on TiO ₂ (110)	59
6.3	Growth Model	63
6.4	Conclusion	65
7	Thermal Activation of O₂ Molecules on TiO₂(110)	67
7.1	Introduction	68
7.2	Diffusion Characteristics	68
7.3	Thermal Activation	69
7.4	Diffusion Mechanism	73
7.5	Dissociation in Vacancies	74
7.6	Conclusion	75
8	Vanadium Oxide Nanoclusters on Au(111)	77
8.1	Motivation	78
8.2	The Model Substrate	79
8.3	Experimental Details	82
8.4	Preparation of V _x O _y Nanoclusters on Au(111)	82
8.5	Characterization	83
8.5.1	Quadratic Phase	84
8.5.2	Hexagonal Phase	85

8.6	Discussion	85
8.6.1	Quadratic Phase	87
8.6.2	Hexagonal Phase	88
8.7	Conclusion	88
9	Summary	91
9.1	Conclusion	92
9.2	Outlook	92
9.3	Acknowledgements	93
	Bibliography	95

Summary

The thesis presents new findings that provide further insight into some of the fundamental processes occurring on the TiO₂(110) surface.

High-speed, high-resolution scanning tunneling microscopy reveals a surprising adsorbate-mediated diffusion mechanism of oxygen vacancies on the rutile TiO₂(110) surface. Adsorbed oxygen molecules mediate vacancy diffusion through the loss of an oxygen atom to a vacancy and the sequential capture of an oxygen atom from a neighboring bridging oxygen row, leading to an oxygen vacancy diffusion pathway strictly perpendicular to the bridging oxygen rows.

A detailed statistical analysis of the discrete spatial distribution of vacancies reveals an anisotropic long-range repulsive interaction up to 6 lattice sites along the bridging oxygen rows. The 2-dimensional pair potential describing the interaction between individual pairs of vacancies is found through Monte Carlo simulations. Entropic effects due to packing of vacancies on the surface are investigated, and the anisotropic pair potential is discussed in terms of electrostatic effects and surface reconstructions.

Bridging oxygen vacancies are shown to be the active nucleation sites for Au clusters on the rutile TiO₂(110) surface. Individual oxygen vacancies and Au clusters are resolved in high-resolution STM images. A direct correlation is found to exist between a decrease in density of vacancies and the amount of Au deposited. DFT calculations confirm that the oxygen vacancy is indeed the strongest Au binding site. The Au clusters are found to contain an average of 3 Au atoms per vacancy trapped underneath the cluster, leading to a new growth model for the Au/TiO₂(110) system involving vacancy-cluster complex diffusion.

The diffusion of oxygen molecules adsorbed on the TiO₂(110) surface is studied at temperatures between 120 K and 250 K. The diffusion is shown to be limited by charge transfer from the conduction band of the surface to the molecule. This charging is critically dependent on the local band bending at the surface and the position of the chemical potential.

Investigations of a model system consisting of vanadium oxide nanoclusters on the Au(111) surface are presented. Vanadium oxide nanoclusters synthesized by deposition in a background pressure of O₂ and annealed in UHV are found in a quadratic and a hexagonal phase.

List of Publications

- [I] *Oxygen-Mediated Diffusion of Vacancies on the TiO₂(110) Surface*,
R. Schaub, E. Wahlström, A. Rønnaau, E. Lægsgaard, I. Stensgaard, and F. Besenbacher, Science **299**, 377 (2003).
- [II] *Bonding of Gold Nano-Clusters to Oxygen Vacancies on Rutile TiO₂(110)*,
E. Wahlström, N. Lopez, R. Schaub, P. Thostrup, A. Rønnaau, C. Africh, E. Lægsgaard, J. K. Nørskov, and F. Besenbacher, Phys. Rev. Lett. **90** 2, 026101 (2003).
- [III] *Long-Range Repulsive Vacancy-Vacancy Interactions on Rutile TiO₂(110)*,
A. Rønnaau, R. Schaub, E. Wahlström, E. K. Vestergaard, E. Lægsgaard, I. Stensgaard, and F. Besenbacher, In preparation.
- [IV] *Thermal Activation of Oxygen Molecules on a Reducible Metal Oxide Surface*,
E. Wahlström, A. Rønnaau, R. Schaub, E. K. Vestergaard, M. Vestergaard, E. Lægsgaard, I. Stensgaard, and F. Besenbacher, In preparation.
- [V] *The Details of the Oxygen Chemistry on TiO₂(110)*,
R. Schaub, E. K. Vestergaard, E. Wahlström, A. Rønnaau, E. Lægsgaard, I. Stensgaard, and F. Besenbacher, In preparation.

CHAPTER 1

Introduction

The $\text{TiO}_2(110)$ surface plays a prominent role in the understanding of metal oxide surfaces and their different behavior from pure metal surfaces. This chapter will motivate a closer look at the fundamental processes happening on the $\text{TiO}_2(110)$ surface and give an outline of the thesis.

1.1 Introduction

Nanotechnology is the scientific striving towards total control of atoms, molecules and larger atomic structures including surfaces and bulk material. This control at the most basic level does not, however, come without difficulty, and at this point basic science is struggling to understand even the simplest building blocks and how they interact. Once this understanding is secured, nanotechnology will be apt to affect every aspect of human life, from the way we produce energy to the way we cure diseases.

Controlling the physical and chemical properties of materials requires detailed knowledge about the behavior of the atoms and their interplay with other atoms in their surroundings. It also requires a type of materials that will allow the manipulations to result in a broad range of properties.

Metal oxides are proving to be a very interesting group of materials in that respect, because they cover the entire range of properties available; some are high TC superconducting while other are insulators, some are magnetic others not, and both their optical and mechanical properties vary a great deal. Metal oxides are currently used as high temperature superconductors, as low rejection medical implant surface structuring, as corrosion passivation, in gas sensing, in photo-electrolysis, in heterogeneous catalysis, as physical filters in sun screen and a large number of other applications [1]. The length of this list is extraordinary, and the diversity in the metal oxide properties of course stems from the diversity and complexity of the materials. This is one of the reasons why metal oxide surfaces are less well understood than metal surfaces. Another reason arises from the insulating properties of most metal oxides, since most surface analysis tools are based on electrons or ions impacting on the surface, giving a problem with charging.

Recently the $\text{TiO}_2(110)$ system has become one of the model systems for understanding the metal-promoted metal-oxide catalysts, because TiO_2 becomes conductive upon a slight reduction of the bulk. The catalytic activity of nanometer-sized gold particles on rutile $\text{TiO}_2(110)$ has spurred a number of investigations using TiO_2 as substrate for nanometer-sized Au, Ag, Pd, Pt and Ir islands [2–8], and the photocatalytic activity of titanium dioxide [9] has opened up for the investigations of photo-induced surface reactivity [10, 11]. Accordingly the rutile $\text{TiO}_2(110)$ surface has been thoroughly investigated to explain its chemical and catalytic activity [1]. Many of the studies link enhanced surface reactivity with the presence of vacancies in the bridging oxygen rows. Examples of such vacancy-correlated surface processes are adsorption of H_2 , CO and O_2 [12] as well as the dissociation of H_2O [13] and O_2 [10, 12, 14]. Vacancies have also been found to promote chemical reactions on the $\text{TiO}_2(110)$ surface [15], as well as they are considered as one of the active sites responsible for the photo-chemical activity of the $\text{TiO}_2(110)$ surface [10].

1.2 Motivation

The present work originally set out with the intent to study the effect of high pressures of CO and O on the Au/ $\text{TiO}_2(110)$ system [16]. The goal was to contribute to the increasing understanding of the model system catalyst in order to affect the way the industry

understands and develops the industrial catalysts.

As the work began, it soon became clear that one of the fundamental problems of the system was the lack of understanding of even the most basic (and indicatively the most important) features on the surface, the bridging oxygen vacancies. How do they react with each other and with gases and adsorbates, how are they created and annealed, and why are there always around 6-8% of them on the surface? These questions seem to be the foundation for a proper description of the TiO₂(110) surface, and without this understanding, the investigations of all more complicated systems will suffer.

The study of the TiO₂(110) surface with the fast, high-resolution scanning tunneling microscopes that were used in the current investigations, has given rise to a huge number of observations that were never reported before. One can imagine a photographer taking night time photos of big cities, who is for the first time able to resolve the single cars that previously got smeared out into long lines of white and red lights because of the prolonged exposure time. Scanning 3-10 times faster than commercial STM's and with a very high resolution, we have been able to resolve surface processes in both time and space, and this has added an additional layer of information about the TiO₂(110) system to previous investigations.

The STM images and movies have revealed processes that can not be identified with any surface averaging technique, and priority has been given to the identification of the different species and processes observed. Without chemical specificity, this process is part puzzle solving and atom counting, and part reinterpreting the data of previous publications to explain the different models, we have proposed along the way. The grand puzzle is being solved, not piece by piece, but as a whole where all the pieces have to fit together at the same time.

This thesis reports on four studies, each of which is a significant contribution to the understanding of the vacancies on the TiO₂(110) surface and their interaction with each other, with adsorbates from the gas phase and with Au atoms and clusters. It is the hope that the work will contribute to the development of a new understanding of TiO₂, which will affect all aspects of technological applications.

1.3 Outline

This thesis has been structured to describe the TiO₂(110) system and the insights that have been gained about it in the most instructive way, and while this is not necessarily the chronological way, it is intended to guide the reader through the insights that have been gained throughout the thesis work.

Chapter 2 introduces the scanning tunneling microscope (STM), describing the principle of operation, the inner workings of the STM and the theory that form the basis for understanding the tunneling phenomena.

Titanium dioxide, which is the substrate of choice in most of the present investigations, is introduced in chapter 3. The properties of both the bulk and the (110) surface are described with emphasis on the point defects, which play a major role in the current work. Density functional theory calculations in relation to the TiO₂(110) surface are discussed, and finally the adsorption of small molecules on the TiO₂(110) surface is

reviewed.

The oxygen-mediated diffusion of bridging oxygen vacancies is described in chapter 4. Experimental observations of the diffusion is complemented with an atomistic model, which describes the interaction between oxygen molecules and vacancies leading to diffusion of the vacancy.

With a less dynamic view point, the pair interaction between vacancies on the surface is studied in chapter 5. The pair potential is found through Monte Carlo simulations and a discussion of entropic effects concludes the chapter.

Chapter 6 concerns the adsorption of Au atoms and the nucleation and growth of Au clusters on the $\text{TiO}_2(110)$ surface. A growth model is proposed based on the experimental observations and backed up by density functional theory.

Chapter 7 concludes the $\text{TiO}_2(110)$ part of the thesis with observations of the thermally activated diffusion of oxygen molecules. The investigations of the rate diffusion at different vacancy densities on the surface lead to a band-bending dependent model of the diffusion of charged molecules, and an explanation for the molecular dissociation in the vacancies seen in chapter 4 is proposed.

Preliminary work on a different, but related, catalyst model system is reported in chapter 8. Vanadium oxide nanoclusters are synthesized on the $\text{Au}(111)$ surface, where the reconstruction of the surface layer is shown to act as nucleation sites. Two cluster types are characterized.

The thesis is concluded by a short conclusion and an outlook in chapter 9. Acknowledgements are also found here.

CHAPTER 2

Scanning Tunneling Microscopy

The scanning tunneling microscope (STM) is the main tool employed in the experiments in this thesis. This chapter describes the general operating principles of the STM, the design of the Aarhus STM and the theories behind the STM.

2.1 Introduction

The scanning tunneling microscope was invented in 1982 by Gerd Binnig and Heinrich Rohrer [17], and revolutionized the field of surface science. This was because it was the first surface analysis technique to image surfaces in real space and with atomic resolution¹. The inventors received the Nobel prize as early as 1986, acknowledging the impact of the technique [18]. Since then, now 20 years old, scanning tunneling microscopy has gone through the initial development phases to reach maturity, and is now being used as a standard tool in many groups around the World [19].

STM is a very powerful instrument as a *local* probe on the surface, and systems like the one studied here, where the local structure of the surface is a key element, could not have been performed using large area averaging techniques like Auger, LEED, XPS etc.

In this chapter, I will describe the principle of the STM, the inner workings of the Aarhus STM, and describe some of the basic theoretical ideas that form the basis for the scanning tunneling microscope. At the end of the chapter is a short introduction to the experimental setup.

2.2 Basic Principles of STM

The principle of the STM is rather simple (see figure 2.1). A sharp metal tip (often tungsten) is brought into close proximity ($z \sim 5 \text{ \AA}$) of a conducting surface. This way the conducting electrons obtain an appreciable probability for tunneling through the vacuum gap which separates the two electrodes.

Applying a voltage between tip and surface causes a tunneling current to flow from filled tip states into empty sample states or vice versa, depending on the polarity of the bias voltage. The resulting tunnel current is of the order of $I_t \sim 1 \text{ nA}$ and has a strong (exponential) dependence on the tip-sample separation. As a rule of thumb, an increase in separation of 1 Å results in a decrease in the tunnel current of one order of magnitude. This is also the reason why one might reasonably expect to achieve atomic resolution in the STM. If e.g., a tip atom protrudes half a bond length further toward the surface than any other atoms in the tip, this apex atom will carry almost the entire tunnel current, and hence the tip can be considered a very localized probe (see figure 2.2). Apart from the exponential dependency on the distance between tip and surface, the high resolution of the STM is made possible by the high stability of piezos to control displacements to a precision of less than 0.1 Å.

Normally the STM is used in the *constant current mode*. The tip is raster-scanned over the surface, and an electronic feedback loop controls the height of the tip over the surface, so the tunneling current is held constant. The height of the tip (actually the voltage applied to the z translator piezo) then gives a topographic map of the (local electronic) surface structure [20, 21].

¹apart from Field Ion Microscopy, which has a number of inherent drawbacks and limitations.

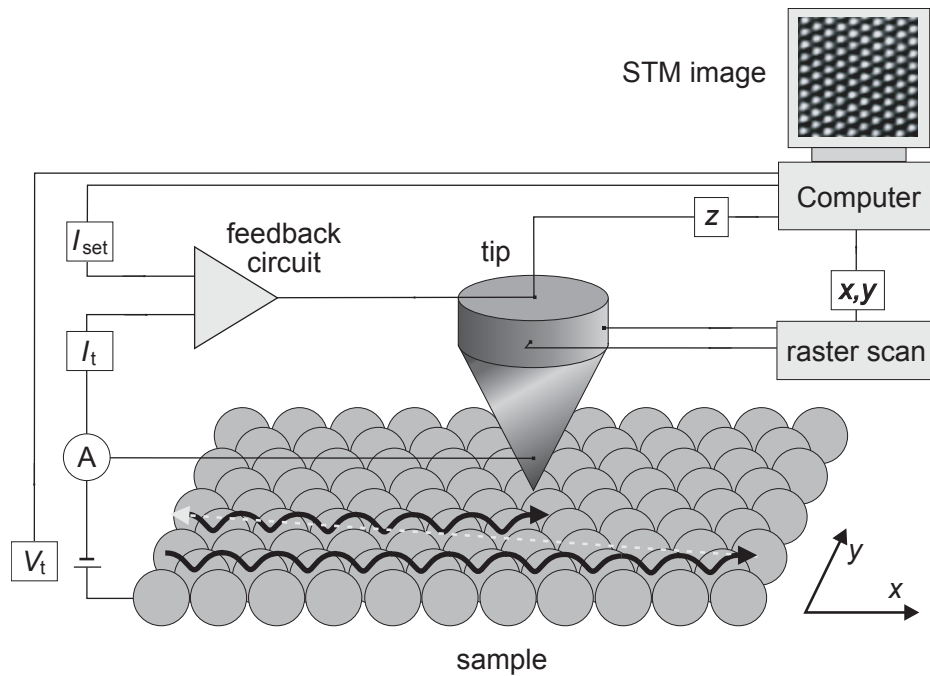


Figure 2.1: (a) The principle of operation of the STM. While the tip is raster-scanned over the surface, a feedback loop controls the height of the tip so the tunneling current is constant. The height of the tip is imaged on the computer as a surface plot.

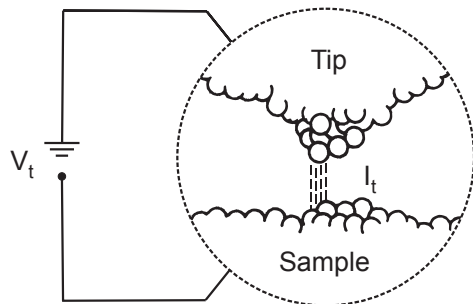


Figure 2.2: Schematic illustration of the tip-sample tunnel junction during STM operation. The ability of the STM to achieve atomic resolution is explained by the strong z -dependence of the tunneling current, whereby essentially all the current flows to or from the single outermost atom protruding from the tip.

2.3 The Aarhus STM

The Aarhus STM was originally designed and constructed by Erik Lægsgaard and co-workers in 1988 [21], and was at the time the fastest STM in the world due to its compact size, which also leads to high mechanical stability and vibrational resistance. The cylindrical design gives a very high thermal stability when operating the STM at different temperatures, since the total thermal expansions are radial and thus minimized in the center, where the tip is placed. Figure 2.3 illustrates the construction of the Aarhus STM.

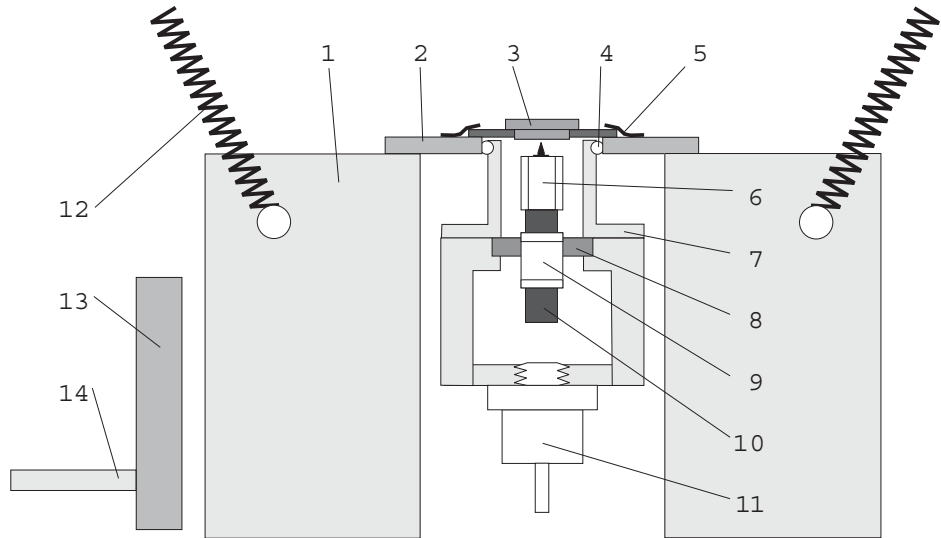


Figure 2.3: Cross-sectional side view of the Aarhus STM. Legend: (1) Al cradle; (2) top plate; (3) sample in sample holder; (4) quartz balls; (5) leaf springs; (6) scanner piezo tube and tip; (7) STM housing; (8) ceramic disc; (9) inchworm piezo tube; (10) SiC rod; (11) Zener diode; (12) suspending spring; (13) coldfinger; (14) liquid nitrogen feedthrough.

The sample in the sample holder (3) is held tight by two leaf springs (5) onto the top plate (2), which is electrically and to a certain degree thermally isolated from the rest of the STM by 3 quartz balls (4), that have a low heat conductance. The top plate is attached to the Al cradle (1), which is suspended in the chamber in low frequency spring (12). Cooling the Al cradle with liquid nitrogen (14) enables us to control the temperature of the sample between ~ 100 K and ~ 400 K, while the STM housing (7) can be counter-heated with a zener diode (11) to stabilize the STM temperatures around RT.

In the interior of the STM, the tube scanner (6) consists of a piezo-electric tube with a single common electrode on the inside and 4 independent electrodes on the outside

making it possible to control not only the x and y (outside electrodes) deflections, but also the stretching/contraction along the z axis (inside electrode). The electronic feedback loop controls the applied voltages, keeping the tunneling current constant, and the voltages are used to generate the topographic STM images. The piezos are the practical foundation for the STM technology, because this is the only way to precisely control positioning at sub-Ångström scale. A voltage of 1V applied to an outside electrode of the tube scanner will deflect the tip $\sim 50 \text{ \AA}$.

The tube scanner rests on a SiC rod which slides inside another piezo tube, the inchworm (9), used for the coarse approach of the tip to the sample. This whole unit is connected to the housing by a ceramic disk (8).

This design provides insulation against mechanical vibrations in two ways. The tight connection of the STM unit and the sample protects against low-frequency vibrations as the whole assembly vibrates as one with no effect on the tip-sample distance. High-frequency insulation is achieved by springs supporting the heavy Al cradle which houses the STM. Together they yield an efficient vibrational insulation against incoming mechanical excitations. The very compact STM possesses (x-y direction) and longitudinal (z direction) resonance frequencies as high as 8 kHz and 90 kHz, respectively, reducing the sensitivity of the STM to external vibrations.

The Aarhus STM has previously been shown to be capable of imaging a variety of metal surfaces at high speed and resolution [22, 23], and recently thin overlayers of Al_2O_3 on NiAl(110) were investigated in the group [24].

The TiO_2 surface is imaged with atomic resolution on routine basis, enabling us to record several hundred high resolution movies, collecting more than 100,000 single STM images with a sampling time down to 0.2 sec/image.

2.4 Theory of STM

To describe the 3 dimensional tunneling problem between tip and sample exactly, detailed knowledge of the wave functions on both tip and sample and the interaction between the two would be needed. The tip is never well described and the general approach to the problem is to consider a simplified system assuming that tip and sample are almost non-interacting [20].

In the Tersoff-Hamann [25] approach, which is based on Bardeen's [26] transfer-hamiltonian, the tip is modelled as a locally spherical potential well with eigenfunctions ψ_μ which overlap with the surface eigenfunctions ψ_ν . In first order perturbation theory the tunneling current I_t is

$$I_t = \frac{2\pi e}{\hbar} \sum_{\mu\nu} f(E_\mu)[1 - f(E_\nu + eV_t)] |M_{\mu\nu}|^2 \delta(E_\mu - E_\nu), \quad (2.1)$$

where $f(E)$ is the Fermi function, E_i refers to the eigen-energies of the respective wave functions in the absence of tunneling, and $M_{\mu\nu}$ is the tunneling matrix element between the tip states ψ_μ and the surface states ψ_ν . The first two terms connect filled and empty states on either side of the barrier where the surface states are moved up or down in

energy by the applied voltage (eV_t). Energy conservation through elastic tunneling is ensured by the delta function. Bardeen showed how $M_{\mu\nu}$, which connects many-particle states before and after tunneling of an electron through a vacuum barrier, is given by

$$M_{\mu\nu} = \frac{-\hbar^2}{2m} \int_{S_0} d\vec{S} \cdot (\psi_\mu^* \nabla \psi_\nu - \psi_\nu \nabla \psi_\mu^*), \quad (2.2)$$

where the integration is over any surface separating the two sides at the vacuum region. Applying this approach to surface waves decaying exponentially into vacuum overlapping a spherical S wave from the outer tip atom, Tersoff and Hamann found a simple expression for the tunneling current

$$I_t \propto V_t \sum_\nu |\psi_\nu(\vec{r}_0)|^2 \delta(E_\nu - E_F), \quad (2.3)$$

where the sum is the local density of states (LDOS) which is evaluated at the center of the tip (\vec{r}_0). This implies that using the STM in a constant current mode, the images will reflect the topography of the LDOS of the surface projected to the position of the tip apex.

The surface states, ψ_ν , decays exponentially into vacuum,

$$|\psi_\nu(\vec{r}_0)|^2 \propto \exp\left(\frac{-\sqrt{8m\phi}}{\hbar}(R + d)\right), \quad (2.4)$$

where ϕ is the average of the two work functions, R is the radius of curvature of the tip and d is distance from tip to surface. This exponential decay in the region between sample and tip is illustrated in figure 2.4.

The exponential decay is used to show that

$$I_t \propto V_t \exp\left(\frac{-\sqrt{8m\phi}}{\hbar} d\right), \quad (2.5)$$

where the exponential dependence on distance clearly shows why atomic resolution is possible. If there is only one atom at the end of the tip, it will carry the main part of the tunneling current.

Assuming an s-wave for the tip, the current can thus be related to a property of the surface alone and hence the interpretation of (low-bias) constant-current STM images is straightforward: they reflect the contour of constant LDOS at the Fermi level. This theory of course breaks down when the tip-sample distance is so small that the assumption of no interaction between tip and sample breaks down.

2.5 Imaging Adsorbates

When using the STM, it is important to keep in mind that the STM images the LDOS of the surface. On clean metal surfaces, the image most often reflects the physical topography of the surface [27], but when adsorbates and/or oxide surfaces are involved,

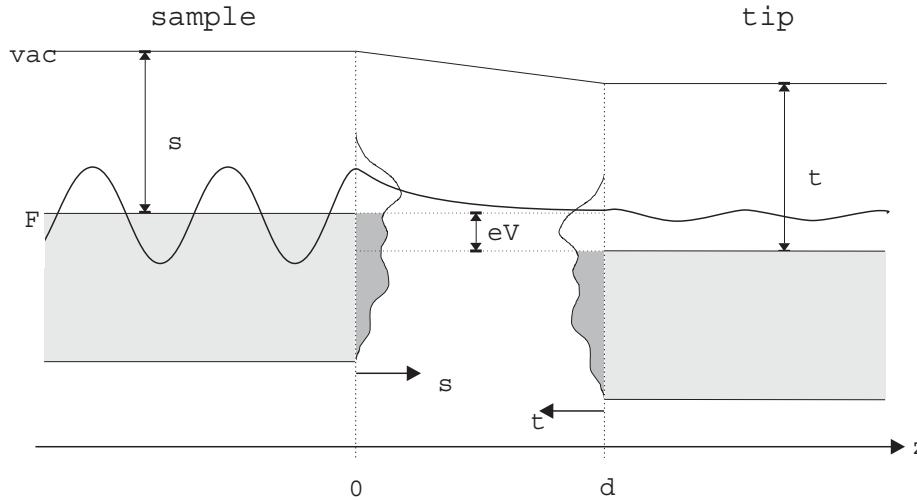


Figure 2.4: Schematic energy diagram for the sample-tip tunnel junction with a width d . A positive bias voltage V is applied to the tip, i.e. tunneling proceeds from occupied sample states to empty tip states (occupied states in the sample/tip are shaded grey). Tunneling is only permitted within the small energy interval eV . ϕ_s and ϕ_t are the (local) work function of the sample and the tip, respectively. The density of states ρ of the sample and the tip are sketched. ψ illustrates a wavefunction at the Fermi energy ϵ_F that decays exponentially in the junction but still has a non-zero amplitude at the tip position. ϵ_{vac} is the vacuum energy.

theoretical calculations are used to support experimental data [19]. TiO_2 , which is studied here, has very different geometric and electronic topographies, as will be shown in chapter 3.

Adsorbate imaging can sometimes give rise to counterintuitive imaging, which can be seen in the O/Pt(111) system [28] and the N/Fe(100) system [29], where the O and N are imaged as depressions with respect to the bare metal surface. Other examples are the imaging of CO on Cu(211) which can appear as a depression or protrusion, depending on the proximity of neighboring molecules and the modification of the tip with CO adsorbed to it [30].

It is generally difficult to identify chemically different adsorbates in STM images. This arises from the fact that STM probes the electronic structure of the surface at the Fermi level and is therefore only indirectly sensitive to the position and chemical nature of the nuclei.

Lang proved that the results by Tersoff and Hamann are valid also for atomic adsorbates [31, 32]. Consequently adsorbates are imaged as protrusions or depressions, depending on how they modify the LDOS at the Fermi level compared to the bare surface, i.e. if they add or deplete electron density.

A review of various theories used to calculate STM images of adsorbates is given in [33].

2.6 Working with Ultra High Vacuum

All experiments were performed in a standard ultrahigh vacuum (UHV) chamber (base pressure less than $1 \cdot 10^{-10}$ Torr), which is relatively large owing to the large number of instruments attached to it. In the following I will describe those that have been utilized during the experiments.

All instruments within the chamber are focused on the center axis, where a very long manipulator arm allows for transfer through the chamber, heating and cooling of the sample, and ultimately transfer to and from the STM's with the help of other linear translators. While in the manipulator, the sample is placed in the sample house, which secures the sample during transport and places the sample very close to a resistively heated annealing filament heating the backside of the crystal. The sample house is connected to a dewar via a thick copper braid to allow for cooling of the sample. Temperatures as low as 105K have been used in the experiments.

An automated system for cleaning of samples controls both the annealing filament and the differentially pumped sputtergun. The gas system connected to the chamber allows for the use of CO, CO₂, H₂ and O₂ dosing as well as the attached commercial molecule cracker (Oxford Applied Research) makes it possible to create a flux of atomic hydrogen or oxygen onto the surface.

For metal deposition an electron beam evaporator (Oxford Applied Research) is used for simple resistive evaporation of Au in a Mo crucible.

Two home-built, high-resolution STMs are installed. The sample temperature can be controlled, during the experiments, within the range ~100 K to 400 K with liquid N₂ and counter-heating. While cooling, the STM must be counter-heated, because the piezos controlling the STM tip movement are highly sensitive to temperature changes.

The chamber background pressure was kept around and below $1 \cdot 10^{-10}$ torr during all experiments.

2.7 Alternative Experimental Methods

The local probe STM has a number of advantages for observing atomic features and single events on the surfaces. However, the images do not reflect averages over large areas of the surface, which is both an advantage and a drawback of the method. Special care must be taken to avoid focussing on (interesting) details that may lead to erroneous generalizations.

Another drawback of the STM is the lack of chemical specificity, which only to a certain degree can be circumvented by atom counting and atomistic model work.

The TiO₂(110) system has been studied very extensively with most other techniques [1, 34]. This means that models based on the STM observations most often can be verified or discarded based on investigations made by other groups.

Extensive references have been made along the way to the temperature programmed desorption work by Henderson and coworkers [35–40], to the photodesorption studies by Yates and coworkers [10,41–46], and to the seminal article by Göpel from 1983 [12].

CHAPTER 3

Rutile Titanium Dioxide

This chapter concerns the basic features of titanium dioxide. The geometric and electronic structure of the rutile bulk TiO_2 is briefly reviewed. The characteristic $\text{TiO}_2(110)$ surface is discussed with respect to stoichiometric and defected structure, in relation to STM, and in terms of density functional theory calculations. The most prominent point defect on the surface, the bridging oxygen vacancy, is treated in some detail, since it governs most of the surface reactions with the surrounding gases. Adsorption of a few of the most important small molecules is reviewed.

3.1 Introduction

Metal oxides differ from metals because of the large degree of ionic bonding in the crystal. In an ideal ionic crystal there is a complete charge transfer between adjacent atoms in the structure, giving all atoms the number of electrons they need to fill the outer shell. This leads to positively charged cations and negatively charged anions giving rise to immense electrostatic forces among the ions. These forces are long-ranged with a $1/r$ dependence, leading to interaction beyond the nearest neighbor. The ions are packed to maximize the contact between those of opposite charge and to minimize repulsions between those of the same charge, surrounding cations with anions and vice versa. The crystal structure is thus determined by the coordination number and the relative sizes of the involved species [1,47,48].

The multitude of effects that have to be energetically minimized in the crystal, means that the structure is highly sensitive to changes in the environment, like defects, giving rise to significant relaxations both in the bulk and on the surfaces.

Point defects on metal oxide surfaces are most often missing anions, that is oxygen vacancies. Removal of a neutral oxygen atoms reduces the coordination of the surrounding cations and leaves behind the two electrons donated to it in the ionization. The electrons can stay in the vacancy as is the case with MgO [49] or they can populate metallic electron levels of the surrounding coordinatively unsaturated metal atoms [1]. The internal forces in the structure may then cause a relaxation around the vacancy.

The most studied metal oxide is the rutile TiO_2 and its (110) surface, due to two reasons.

- TiO_2 has substantial applicational value as discussed in chapter 1.
- TiO_2 is easily reducible in the bulk, making it conductive and thus making it possible to use standard surface science tools based on electron and ion impact.

3.2 Bulk Rutile TiO_2

Titanium dioxide was discovered in 1791 when amateur chemist William Gregor examined sand from the local river. He used a magnet to extract ilmenite (FeTiO_3), from which he removed iron by treatment with hydrochloric acid. The residue was the impure oxide of a new element. Gregor discovered the reactions which were to form the basis of the production of virtually all titanium dioxide up to around 1960. German M. H. Klaproth independently discovered titanium dioxide in 1795 and named the metal titanium after the mythological titans, the first sons of the earth [50,51]. There is a small percentage of titanium in many silicate and oxide minerals as titanium is the 9th most abundant element in the Earth's crust, but bulk rutile TiO_2 is not found in nature [51,52].

Titanium dioxide is used in heterogeneous catalysis [2,53–55], as a photocatalyst [56] for waste water treatment [57], in biocompatible implants [58], in solar cells for the production of hydrogen and electric energy [56,59], as a gas sensor [1,12], and as an optical coating [60]. When it is bombarded with ultraviolet rays, it becomes a sterile surface and, for a long period of time afterwards, will kill any germs that come in contact

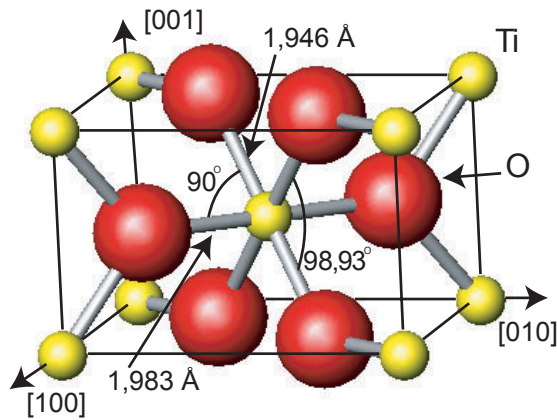


Figure 3.1: The primitive unit cell of bulk rutile TiO₂. From [65]

with it [57,61]. Titanium dioxide doped with Al³⁺ to suppress the photoreactivity is, due to its high refractive index, durability, strength, chemically inert nature and non-toxicity, widely used for coatings (implants), as white pigment in paints, lacquers, inks, shoe whiteners, ceramics and even chewing gum [62]. It is used as a sunblock in sunscreen creams, because it scatters light and does not irritate skin, and because it is not soluble in water [62]. Titanium dioxide is used to clean the air in space [63].

Stoichiometric rutile TiO₂ is a transparent yellow non-conducting crystal which turns black (via blue) upon reduction of the bulk [34].

3.2.1 Geometric Structure

Rutile TiO₂ has a flat tetragonal unit cell with two Ti atoms and four O atoms (fig. 3.1). The Ti atoms are surrounded by six O atoms, and as in many ionic crystals the geometric structure is determined by the relative size of the ions and the coordination [64]. The octahedral configuration of O atoms around the Ti atom is slightly distorted to accommodate all the ions. Bond lengths between Ti and O atoms are 1.946 Å and 1.983 Å for the four-fold symmetric and two-fold symmetric bonds respectively. In the crystal, the octahedra are stacked with their long axis alternating by 90° resulting in three-fold coordinated O atoms [34]. This can be seen in figure 3.2.

3.2.2 Electronic Structure

Rutile TiO₂ is an insulator with a wide bandgap of ~ 3 eV. The valence band is based predominantly on O 2p orbitals, while the conduction band is Ti 3d based [66]. The *ionicity* (the degree of ionic bonding) of rutile TiO₂ is of the order of 70%, meaning that it has a non-negligible covalent character. Figure 3.3 shows the theoretically calculated density of states (DOS) of the oxygen 2p and the Ti 3d orbitals [66].

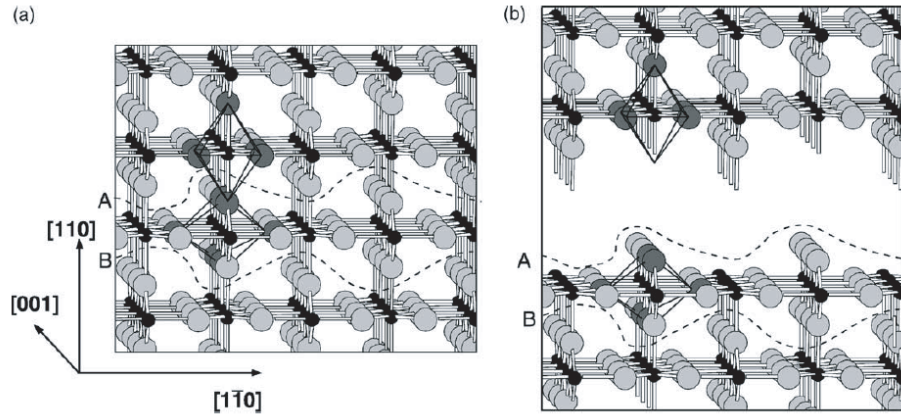


Figure 3.2: Ball and stick model of the rutile crystal structure. (a) Slightly distorted octahedra rotated by 90° give the characteristic structure with channels along the [001] direction. (b) Cleaving the crystal along A gives a charge neutral repeat unit without a dipole moment perpendicular to the surface. From [34]

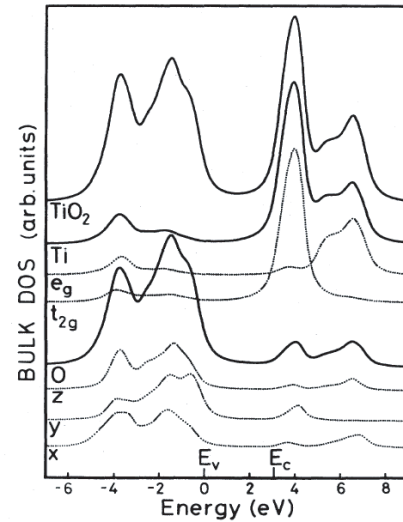


Figure 3.3: The density of states (DOS) of bulk TiO_2 . The DOS is decomposed into partial Ti and O density of states, and their respective symmetry subbands. Ti states in the valence band region and O states in the conduction band region arise from the non-negligible covalency in TiO_2 . From [66]

3.2.3 Bulk Defects

Titanium oxide has a large number of stable phases, and since Ti is in its maximum valency state in TiO₂, it is easily reducible [1]. Upon reduction, O vacancies and Ti interstitials are introduced in the bulk giving rise to a significant change in properties. The defects result in n-type doping introducing donor levels in the band gap, enhancing the conductivity [34, 67].

In titanium oxide, oxygen vacancies form color centers which trap electrons 0.76 eV below the conduction band [52, 68, 69], and change the color of the crystal from transparent through light to dark blue.

Ti interstitials have been shown to be the dominant type of bulk defect. Sputtering causes a preferential removal of oxygen from the surface. The surface stoichiometry of the sputtered TiO₂ surface is then restored when annealing in UHV through transport of Ti atoms to the bulk [39]. These bulk Ti interstitials introduce donor states very close to the conduction band (0.002, 0.02 and 0.05 eV below the conduction band), which explain the enhanced conductance of reduced TiO₂ [70–73], because the chemical potential (Fermi level) is moved up very close to the conduction band [48, 71].

Ti interstitials diffuse relatively fast through the open channels of the crystal along the (001) direction (see figure 3.2), while oxygen in the bulk diffuse by site exchange with other oxygen atoms giving rise to an effective diffusion of bulk oxygen vacancies [34].

3.3 The Rutile TiO₂(110) Surface

The rutile TiO₂(110) surface is the most stable of the low-index rutile surfaces and it is the most studied TiO₂ surface [1].

The (110) surface is bulk terminated, and can be seen as created through cleaving of bulk material, leaving two equal opposite surfaces as seen on figure 3.2 (b). With this termination, the top-most layer (between A and B in figure 3.2) is charge neutral, containing twice as many O²⁻ as Ti⁴⁺ ions. Due to some degree of covalent bonding, the stability of the surface is also founded in the fact that this termination breaks the least number of bonds and the longest bonds in the crystal structure [74].

The surface contains both Ti atoms and O atoms with two different kinds of coordination. In the surface plane rows of five-fold coordinated (5f) Ti atoms alternate with rows of six-fold coordinated (6f) Ti atoms separated by rows of O atoms. All rows are in the [001] direction. The former Ti atoms are exposed to the surroundings, while the latter are covered by rows of two-fold coordinated O atoms positioned in bridge sites above them, giving them the name bridging oxygen rows (see figure 3.4).

The (1x1) surface unit cell is 2.96 Å in the [001] direction and 6.5 Å in the [1̄10] direction [74].

When bonds are *broken* at a surface, the top layers accommodate the dangling bonds by relaxing into a more energetically favorable structure. In metal surfaces this relaxation most often causes a contraction of the outer-most layer [76]. On the TiO₂(110) surface the two different types of Ti atoms move in opposite direction causing a rumpling of the in-plane layer. Ti (5f) atoms move inwards towards the bulk by 0.16 Å,

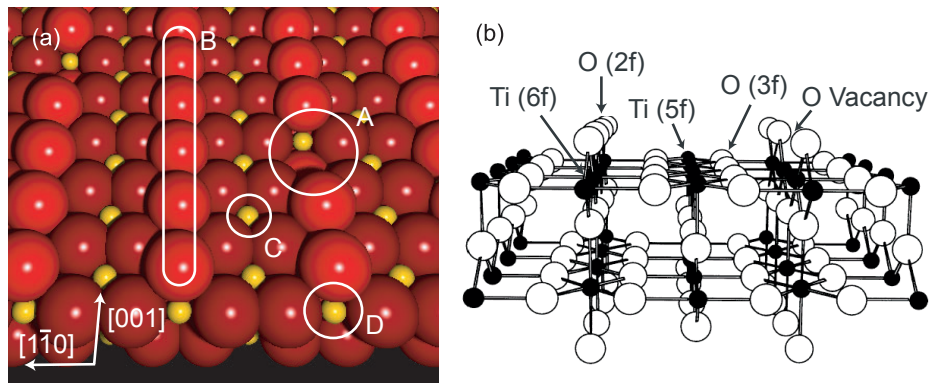


Figure 3.4: (a) Ball model of the rutile $\text{TiO}_2(110)$ surface, illustrating (A) a bridging oxygen vacancy, (B) a bridging oxygen row in the [001] direction, (C) a five-fold coordinated Ti atom and (D) a six-fold coordinated Ti atom, (b) ball and stick model of the underlying structure of the rutile $\text{TiO}_2(110)$ surface illustrating the coordination of the individual atoms (from [75]).

while $\text{Ti}(6f)$ atoms move outward by 0.12 \AA . The bridging oxygen atoms above the $\text{Ti}(6f)$ relax inwards by as much as 0.26 \AA . The second layer relaxes in the same directions, but the relaxations are significantly less [74, 77].

3.3.1 Defects on the $\text{TiO}_2(110)$ surface

The (110) surface contains two types of point defects as seen in STM, the so-called type A and type B defects [75].

The Type A defects have recently been shown to incorporate both bridging oxygen vacancies and bridging hydroxyls [13], and the next section is dedicated to a more detailed discussion about the structure and appearance of the bridging oxygen vacancies in STM.

Type B defects can be seen on some STM images as slightly darker areas as if the subsurface structure is defective to some degree. No explanation has been given to explain the B type defects, though speculations exist that they are missing oxygen atoms just below the surface [75].

With a strong focus on the bridging oxygen vacancies in this report, this section will not concern other types of defects like step edges, line defects, impurities or crystallographic shear planes. The excellent review by Diebold has a section devoted to these defect types [34].

3.3.2 Bridging Oxygen Vacancies

Oxygen vacancies are present in the TiO_2 crystal due to thermodynamic reasons. The defects have a finite positive free energy of formation, and they are stable in finite quan-

ties because of the favorable entropy associated with the introduction of defects in the otherwise well-ordered system [71].

Ti, being a transition-metal with a partly filled d-band, can exist in several different oxidation states (0,+2,+3,+4). With the low energy difference between states in the d-band, the creation of an oxygen vacancy is not energetically unfavorable since the remaining two electrons left over from the removal of the oxygen atom (ionic bonding) can relocate (partly [73, 74]) onto the surrounding two Ti atoms changing their oxidation state from 4+ to 3+. The complex surface chemistry of TiO₂ can partly be explained in terms of the number of different oxidation states and thus the presence of vacancies [1].

Oxygen vacancies are created when the TiO₂ crystal is heated above 500 K [75], because bulk vacancies and top layer Ti atoms diffuse to equilibrate the crystal [39].

3.3.3 Preparation of the Surface

The TiO₂ samples were prepared by multiple cleaning cycles (10 min. 800 eV Ar⁺ sputtering, 5-15 min. annealing at 877 K in an O₂ ambient (10^{-6} Torr) followed by 10 min. annealing at 877 K in UHV). The oxygen stage causes a small number of remnant oxygen molecules (≤ 0.01 ML) to be present on the surface, and while this can be avoided to some degree if the oxygen stage of the preparation is left out, there will always be a few oxygen molecules on the surface.

Preferential sputtering of the surface oxygen depletes the surface of oxygen until an equilibrium is reached. The surplus of Ti cations at the surface then causes a net flow of Ti cations into the bulk during the subsequent annealing, giving rise to both Ti interstitials and oxygen vacancies in the bulk and oxygen vacancies on the surface [39]. Annealing the TiO₂(110) surface to 877 K in an oxygen ambient causes regrowth of the crystal, as bulk diffusing Ti atoms reach the surface and are oxidized first to Ti₂O₃ and then to TiO₂ [39, 78].

Terraces on the rutile TiO₂(110) surface can be quite extended, but are normally 50-200 Å across, depending on the preparation procedures. [75].

3.4 STM on TiO₂(110)

The TiO₂(110) surface was imaged with STM for the first time in 1990 [79], and atomic resolution was obtained in 1994 [80]. Interpretation of the STM data took a little longer, and it was not until 1996 that the final interpretation was found [81].

When imaging the TiO₂(110) surface with STM (see figure 3.5), it is only possible to work with a positively biased sample, since a negatively biased sample inevitably causes the tip to crash into the surface, ruining resolution. When biased positively, electrons tunnel from the tip of the STM into empty surface states. As seen on figure 3.3, these states are located primarily on the Ti atoms and the in-plane Ti atoms appear protruding in the STM images. Due to the very low LDOS at the Fermi level of oxygen atoms, they are imaged as depressions with STM, despite the fact that they protrude, so that the bright rows in the STM images are indeed the rows of Ti(5f) atoms along the (001) direction (compare figure 3.5 with figure 3.6). An apparent reversal of geometry

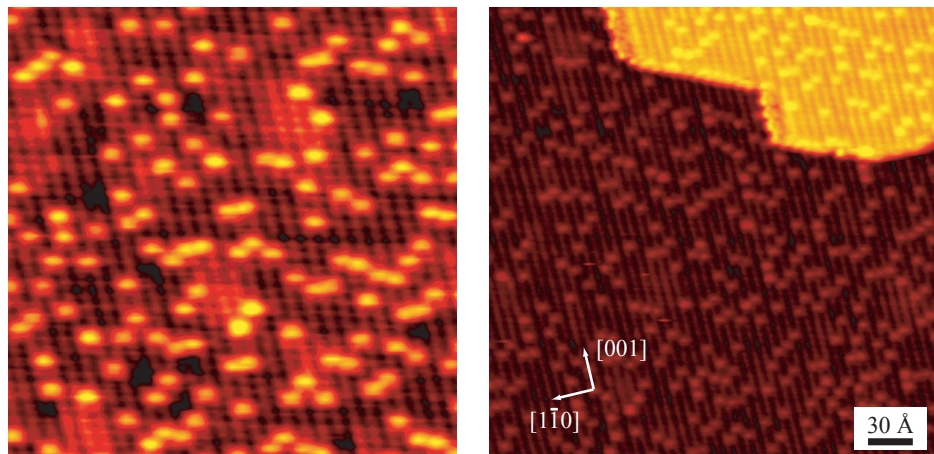


Figure 3.5: STM images of the TiO_2 surface. The bright lines are Ti rows separated by darker bridging oxygen rows with oxygen vacancies imaged as bright protrusions. (a) Close up with a color scale that enhances the vacancies (The size is $180 \times 180 \text{ \AA}^2$). (b) Larger image which shows the rows and vacancies on to terraces (The size is $300 \times 300 \text{ \AA}^2$).

compared to the physical geometry of the surface made the original interpretation hard until theoretical calculations gave the correct interpretation [81].

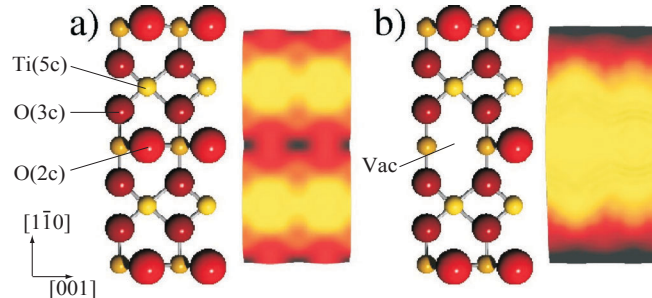


Figure 3.6: TiO_2 surface structures and simulated STM images of (a) the stoichiometric TiO_2 surface illustrating how the $\text{Ti}(5f)$ appear as protruding, (b) a missing oxygen atom in a bridging oxygen row giving rise to a protrusion on the bridging oxygen row [13].

Typical imaging parameters for the tunneling is $V_t = 1.25 \text{ V}$ and $I_t = 0.1 \text{ nA}$. These parameters have reproducibly proven to give good resolution and are rarely changed after good resolution has been achieved. To recover good resolution it is often necessary to scan extremely fast on large areas with a high voltage ($\sim 10\text{V}$).

In STM bridging oxygen vacancies appear as protrusions on the bridging oxygen rows, and until recently it was not clear if they were missing oxygen atoms or hydroxyls (O-H groups). A recent study has shown that both defect types look much the same in STM images, but that the two can be distinguished from each other in size [13]. Figure 3.5 shows a typical STM image of the surface with bridging oxygen vacancies clearly present. Simulated STM images in figure 3.6 illustrates the difference between (a) the stoichiometric surface and (b) a bridging oxygen vacancy.

3.5 Density Functional Theory on TiO₂(110)

As discussed in sections 2.5 and 2.7, the STM does not reveal direct information about the chemical nature of a given feature on the surface and alternative experimental methods are used to confirm observations with the STM. Theoretical calculations are also used to support experimental observations and this section concerns the current status of the calculations and their reliability.

Density functional theory (DFT) [82, 83] studies of the TiO₂(110) surface have shown one thing with absolute certainty: It is a very complicated system to study with theoretical methods. With a typical metal surface, you only need a few layers of atoms (or even a small cluster) to simulate a surface [84]. With metal oxides the situation can be somewhat different.

When modelling the TiO₂(110) surface, theorists speak of the number of trilayers, illustrated on figure 3.2 (b), where the layers between the dotted lines A and B is a trilayer. One such trilayer is stoichiometric in the ratio of Ti and O atoms, and it is symmetric over the Ti plane, which allows theorists to make slabs that have identical surfaces on both sides, increasing the symmetry of the calculations.

The number of layers in a slab was in 1997 shown by Bates *et al.* [85] to be of fundamental importance to the integrity of the calculations. The problem is one of convergence of the surface energy, and with that all other energies relating to the surface. Typically the slabs are made out of 3-5 Ti layers and relaxed fully. The relaxations in the surface region (of which there are two in the slab) are rather large and extends into the layers below the surface layer, but with the small number of layers, this means that no actual bulk phase exists in the calculations. The relationship of the surface with the bulk phase is very important, and removing the bulk phase and making the surface the back-side of another surface, the comparability to the real TiO₂(110) surface could be lost. Bates showed that it takes 6 Ti layers to reach acceptable convergence for the surface parameters. Rasmussen *et al.* has very recently used a slightly different method [86]. Their systematic study of the surface energies uses a slab consisting of 2-6 layers where only one side of the slab is allowed to relax away from the bulk parameters. They show that it takes 4 Ti layers with 2 layers relaxed to reach acceptable values, and that even 6 layers with 2-3 relaxed layers may not reveal completely relaxed surface energies. Their observations of oscillations in the surface energies are consistent with those of Bates [85]. The oscillations are also found in the rutile SnO₂ system, indicating that the phenomenon could be closely related to the rutile structure.

Another problem with DFT results is the problem of surface super cells. As we shall

see in chapter 5 long-range interactions dominate the reduced (and thus interesting) surface along the [001] direction. Again primarily due to computational limits, very few studies have used a super cell larger than (3×2), which is significantly too small to make concrete statements about the energetics of the surface, the vacancy creation and the interaction with adsorbates [74, 87–91].

Despite the inherent problems in doing theoretical calculations on the $\text{TiO}_2(110)$ surface, theory have added valuable information about the system. The reversal of geometry and electronic properties was a problem which was discussed in the early nineties until Diebold *et al.* calculated the charge density above the surface using DFT methods [81]. With the increase in computational power and a significantly better understanding of the system, the next years will be very interesting with respect to the theoretical findings and eventually predictions concerning the $\text{TiO}_2(110)$ system.

3.6 Adsorption of Small Molecules on $\text{TiO}_2(110)$

With the wide variety of technological applications utilizing the properties of TiO_2 , it is no wonder that extensive studies have been made of the interaction of gases with the surfaces of TiO_2 . The adsorption, dissociation and/or reactions of atoms and molecules on the $\text{TiO}_2(110)$ surface are of fundamental importance to the understanding of the surface chemistry that governs the exciting technological applications. Extensive experimental and theoretical work has been done on the system, and this work has been excellently reviewed by Henrich/Cox and Diebold [1, 34]. This section is primarily based on these reviews, where I will focus on some of the interesting features of adsorption of small molecules from the gas phase on $\text{TiO}_2(110)$ in order to give a better background for reading the next chapters. That said, I should warn the reader that even the simplest adsorption chemistry on the $\text{TiO}_2(110)$ surface is not well understood. Different experimental groups disagree, and the discrepancies between experiment and theory are at times appalling.

Chemisorption on the $\text{TiO}_2(110)$ surface is very much affected by the ionic nature of the crystal. Ti cations on the surface are coordinatively unsaturated and act as Lewis acids (electron pair acceptor) and may interact with electron donors like H_2O . Bridging oxygen atoms are basic sites and interact with electron acceptors like H^+ creating bridging hydroxyls (-OH groups).

Most studies show that the stoichiometric (110) surface is relatively inert, as is expected since it is the lowest-energy surface of the TiO_2 surfaces [1].

The primary adsorption sites on the non-stoichiometric surface are the bridging oxygen vacancies, where especially dissociative adsorption is found. The main problem with the study of these interactions is the inherently low concentration of these vacancies, which makes the relative vacancy to stoichiometric surface signal very small when utilizing space averaging surface science techniques.

The vacancies are hot spots with respect to adsorbates, because two electrons are left in non-bonding 3d states on the neighboring coordinatively unsaturated Ti atoms. This makes electronic interactions favorable in a large number of cases, and in the next I shall briefly review some features relating to molecules both present in the background gases

in the chamber and others of general interest.

3.6.1 H₂ and H

The adsorption sites and characteristics of hydrogen on the TiO₂(110) surface are still unresolved. Molecular hydrogen does not stick to the stoichiometric surface at room temperature. When dosing molecular hydrogen on the reduced surface, several experimental studies favor the dissociative adsorption of two hydrogen atoms in the bridging oxygen vacancies each bound to a five-fold coordinated Ti atom as a hydride (Ti(III)-H) [12, 92], while others find no change in the surface-defects states upon exposure to hydrogen molecules [93]. Very few theoretical studies have been made, and falling short with respect to the problems stated in section 3.5, they claim that hydrogen binds more strongly to both the bridging oxygen atoms and to the acidic cation sites on the stoichiometric surface than in the vacancies [94, 95].

Dosing atomic hydrogen also bring about unresolved matters. Suzuki claims that by dosing atomic hydrogen cracked over a hot filament in front of the sample, around 25% of the bridging oxygen atoms are hydrogenated to form hydroxyls [92], while Wöll in similar experiments finds 100% hydroxyls on the surface by means of helium scattering [96]. A relatively dubious time-of-flight elastic recoil detection study by Fujino adsorbs 80% of a monolayer hydroxyls, suggesting based on a low sticking coefficient that hydroxyls are created through the vacancy sites [97]. Preliminary studies carried out by Schaub *et al.* [98] confirm by use of STM (and a commercial hydrogen cracker) the findings of Suzuki.

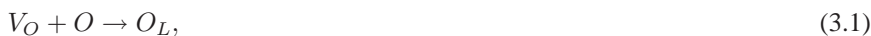
An interesting problem with hydrogen on the TiO₂(110) surface is the fact that hydrogen is able to diffuse into and out of the bulk, effectively making the crystal a hydrogen reservoir. The hydrogen atoms have been shown to diffuse preferentially along the bulk crystal channels visible in figure 3.2, while some diffusion have been found along the (110) surface normal [99, 100].

This creates a dependence on the history of the sample, and since all UHV chambers have a background partial pressure of hydrogen, all samples studies will have some degree of hydrogen in them.

3.6.2 O₂ and O

The oxygen chemistry on the TiO₂(110) surface is reviewed briefly here with respect to previous studies of the surface. Chapter 4 discusses our findings related to the oxygen mediated diffusion of bridging oxygen vacancies on the surface and chapter 7 concerns the thermal activation of oxygen molecules through electron transfer from the substrate. The chapters will explain and elaborate on some of the models reviewed here.

It was previously assumed that the entire interaction between oxygen molecules and the surface was through a simple dissociative filling of a vacancy:



where V_O is the bridging oxygen vacancy, O the adsorbed oxygen atom and O_L a bridging oxygen atom in the lattice structure [12]. The filling of vacancies has been shown

several times both through UPS [14], XPS [101], TPD [38,40], ELS [40] and STM [75], but while the filling is known, the proposed filling mechanism [38] is shown in chapter 4 to be wrong at the coverages investigated in this thesis.

At low temperatures (~ 100 K) Henderson et al. show that three oxygen molecules adsorb for each vacancy present on the surface [40]. They argue that all three molecules are bound as O_2^- species in and around the vacancy. The molecule in the vacancy dissociates to fill the vacancy, while the other two molecules desorb at 410 K. The remaining oxygen atom (from the dissociation) is unaccounted for in [40], while the same group in [38] suggests that the single atom most probably diffuse into the bulk. When exposing the vacuum annealed surface to 2.4 L O_2 at 120 K (shown to correspond to the coverage of vacancies) a significant TPD peak is found at 410 K. This peak disappears, if the oxygen dosing is done in two steps with an initial exposure of 0.8 L O_2 at 120 K followed by annealing to 200 K and then exposure to the remaining 1.6 L at 120 K to give a total of 2.4 L O_2 . This would indicate that further molecular adsorption is blocked by the annealing the surface with oxygen molecules adsorbed in the vacancies.

Lu et al. [44,45] find two low temperature oxygen species, with distinctly different photo-desorption patterns; one channel (α) which undergoes slow photo-desorption and can be photo-activated to oxidize CO to CO_2 , and a fast channel (β). The α state is populated at 105 K, and it is thermally converted into the β state above 200 K, indicating that either the β state is more strongly bound to the surface than the α state or the α state is not entropically stable above 200 K. Population of the β state is maximized between 250-300 K.

A three Ti layer theoretical study also points in the direction of three oxygen molecules being bound as superoxide ions (O_2^-) [102], and a more recent theoretical study confirms the existence of vacancy-bound molecular oxygen [86].

3.6.3 H_2O and OH

As with hydrogen and oxygen, controversy has riddled the investigations of water adsorption of the $TiO_2(110)$ surface. A clearer picture is evolving, and I shall only give the currently accepted picture of the adsorption characteristics here. For further information the excellent review by Henderson is recommended [103].

Molecular adsorption of water on metal oxides usually occurs on acidic cations (acceptors) with the oxygen atom pointing downwards and the hydrogens pointing away from the surface. For dissociation to happen on this surface, one of the hydrogen atoms has to be in close proximity of an oxygen atom (a base), which is not the case on the $TiO_2(110)$ surface [37].

Three different TPD peaks are found after dosing H_2O on the surface. A lower peak found at 155-175 K is attributed to multi-layer desorption, while a peak at 270 K is attributed to the desorption of molecular water from the five-fold coordinated Ti^{4+} sites between the bridging oxygen rows. A third H_2O TPD peak at 410 K is ascribed to the associative desorption of bridging O-H groups [36,37,101,104,105].

Henrich et al. detected, using UPS, surface hydroxyl groups present after adsorption of H_2O on a slightly reduced $TiO_2(110)$ surface at 300 K [106]. Several other studies have confirmed this [13,14,37,101,104] and consensus is that H_2O adsorbs in

the bridging oxygen vacancy, where one of the hydrogen atoms is transferred onto the neighboring bridging oxygen atom [13]. Isotopic labelling studies have shown that the hydrogen atoms loose memory of the original adsorption site in the dissociation process, indicating that they readily diffuse along the bridging oxygen rows [37].

3.6.4 CO

According to work by Göpel *et al.* [12] adsorption of CO is not possible on the stoichiometric TiO₂(110) surface. Only when bridging oxygen vacancies act as active sites for chemisorption will CO adsorb, and then it may form CO₂ by reaction with an adjacent bridging oxygen atom [12]. CO dosed at 105 K [10], desorbs from the stoichiometric surface at 135-170 K. TPD shows no scrambling of the CO with lattice oxygen and no desorption of CO₂ from the surface (when CO is dosed at 105 K). CO adsorbed in or at vacancies are found to desorb in the 170-350 K range [10, 41].

Theoretically CO has consistently been shown to adsorb on the stoichiometric surface with the C end down, but no conclusive investigations have been made of the CO adsorption by or in a vacancy [34]. The present studies has included work with CO adsorption in vacancies and CO oxidation, but unfortunately at the time of writing, the experiments have not reached a conclusive end.

CHAPTER 4

Oxygen Vacancy Diffusion on $\text{TiO}_2(110)$

Bridging oxygen vacancies are found to diffuse in a correlated manner, perpendicular to the bridging oxygen rows. Low temperature experiments illustrate that the diffusion is mediated by oxygen molecules. An atomistic model for the diffusion mechanism is proposed, where the oxygen molecule fills the vacancy, leaving a single highly reactive oxygen atom on the Ti rows, which subsequently reacts with a lattice oxygen to recreate the bridging oxygen vacancy in either the original position or on the neighboring row. This chapter is based on paper I.

4.1 Introduction

Diffusion affects most processes happening on surfaces [107] like crystal growth [39], cluster growth [108–110] and reaction dynamics including associative desorption [13] and catalytic behavior [53, 111, 112] in heterogeneous catalysis.

Bridging oxygen vacancies are adsorption sites for most of the smaller molecules participating in the various catalytic processes occurring on the TiO₂(110) surface [113], so the diffusion of the vacancies is expected to play a prominent role in the reactivity of the surface.

When looking at the physical morphology of the TiO₂(110) surface (see the ball model in figure 4.2), it is quite obvious that the simplest imaginable diffusion mechanism of vacancies is the diffusion of a single bridging oxygen atom along the bridging oxygen row to fill a neighboring vacancy. This mechanism would lead to diffusion along the [001] direction. Surprisingly we find that the diffusion of vacancies at RT is strictly perpendicular to the [001] direction. In this chapter, the correlated diffusion of bridging oxygen vacancies perpendicular to the [001] rows of the TiO₂(110) surface is described, showing that the diffusion is mediated by oxygen molecules on the surface, and a novel diffusion mechanism for the vacancies is proposed. The diffusion described is not a simple diffusion, and emphasis has been put on the atomistic model of the process. Chapter 7 deals with aspects related to molecular oxygen diffusion along the Ti rows, which influences the diffusivity of the oxygen vacancies.

Assisted diffusion has previously been investigated with STM on self-diffusion metal systems [114], and recently mediated diffusion was studied where surface vacancies mediate the diffusion of tracer atoms in Cu surface layers [115]. To our knowledge, no previous observations of vacancies diffusing through a mediated process exists, and while this may be specific to the titanium dioxide it is likely that other metal oxide surfaces exhibit similar behavior.

4.1.1 Room Temperature Observations

When consecutive STM images are visualized as so-called STM movies, the diffusion of the bridging oxygen vacancies become apparent. An STM movie have been made available online as supporting material for paper I [116]. The STM movies were recorded at RT with a high image acquisition rate to gain high temporal resolution.

Figures 4.1 (a) and (b) show 2 consecutive STM images from one of the STM movies [116], where a diffusing vacancy is marked by a circle. The initial position of a diffusing vacancy in one image and the final position in the next image are made clearly visible by use of a difference plot (image (c)), where image (b) has been subtracted from image (a). The difference plot illustrates the pairing of the initial and final positions indicating that the diffusion only occurs perpendicular to the bridging oxygen rows. The observed process is illustrated in figure 4.2. The difference plot also provides evidence for a "track" across the surface, where vacancies have moved perpendicular to the rows leaving the vacancies in other areas immobile.

Difference plots between 700 consecutive images were analyzed, and the spatial correlation between the initial and final positions of vacancies was calculated. Figure

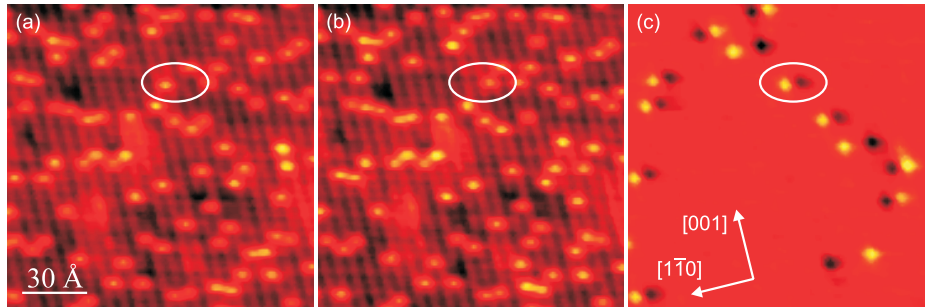


Figure 4.1: (a) and (b) Consecutive STM images each acquired in ~ 8.5 s, (c) the difference plot, where image (b) has been subtracted from (a). A light protrusion corresponds to the original vacancy position in image (a) while a dark depression is the new position of a vacancy in image (b). The pairing of the initial and the final position is quite evident.

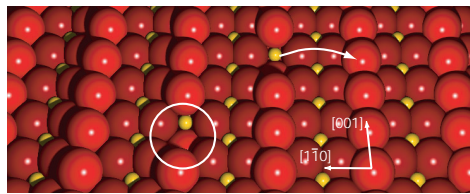


Figure 4.2: Ball model illustrating the observed diffusion process.

4.3 is a displacement-vector density plot, which shows that the diffusion at RT only occurs along the $[1\bar{1}0]$ direction.

As mentioned in the introduction, the diffusion exclusively perpendicular to the $[001]$ bridging oxygen rows is rather surprising, when considering the surface structure. The nearest neighbor distance along the $[001]$ direction is 3 \AA , while the distance between two oxygen rows is 6.5 \AA . The surface unit cell is shown in figure 4.3 to illustrate the distances.

The crystal preparation procedure has a significant impact on the amount of diffusion events at RT. The preparation of the $\text{TiO}_2(110)$ surface includes 5 minutes annealing of the sample at 877 K in an O_2 ambient (10^{-6} Torr) followed by 10 min. annealing at 877 K in UHV. Samples prepared without this oxygen stage exhibit at RT very few vacancy diffusion events, whereas samples annealed in UHV for only 5 minutes after the oxidation stage show a substantial increase in vacancy mobility. This indicates that remnant oxygen species on the surface could be mediating the diffusion of the oxygen vacancies.

A number of experiments were made to confirm this. Oxygen was dosed by backfilling the chamber with the sample (at 300 K) placed in the manipulator. Returning

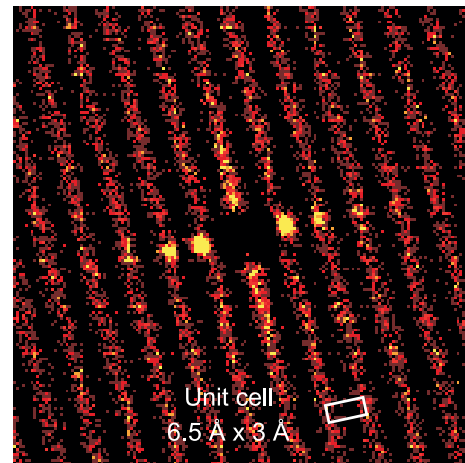


Figure 4.3: Density plot of distance vectors between all original and final positions of vacancies. Three peaks can be seen on each side of the origin, indicating the presence of single, double and triple "jumps" of the vacancies. The surface unit cell is shown.

the sample to the STM revealed an increased number of diffusion events, and a larger number of oxygen species on the surface depending on temperature and dosage. When further investigating the effect of O₂ exposure, it was found that the frequency of vacancy diffusion events correlates with the amount of O₂ exposed on the sample until one monolayer of O₂ has been dosed (Fig. 4.4). When more than one monolayer is deposited, the frequency of diffusion events levels out due to the formation of other oxygen species on the surface. These species will be discussed further in Paper V, but is not subject to further discussion here. This result, together with the vacancy diffusion mechanism being correlated and proceeding perpendicular to the bridging O rows, points to an adsorbate-mediated diffusion mechanism. It will be shown below that O₂ is indeed the diffusion-mediating species. However, at RT these adsorbates diffuse too quickly to be observed directly in our STM experiments.

4.1.2 Low Temperature Observations

To investigate the vacancy diffusion mechanism in further detail, the sample temperature was lowered to below ≈ 250 K, where the mobility of O₂ is sufficiently reduced to enable direct STM observation. The O₂ molecules are identified as additional protrusions (imaged 0.2 Å higher than oxygen vacancies) in the STM images (Fig. 4.5 (A)) and for low O₂ exposures (0.1 to 1 L dosed at RT) their density increases with the O₂ exposure. From high-resolution STM images (Fig. 4.5 (B)) the O₂ is found to adsorb on top of five-fold coordinated Ti atoms.

The possibility of a small protrusion being a single oxygen atom is ruled out for the following reasons: (1) Experiments were made where atomic oxygen was dosed with a

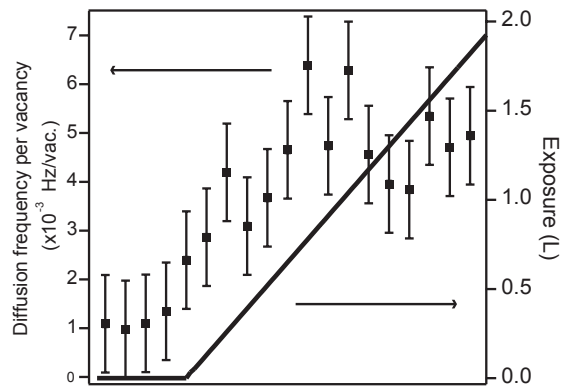


Figure 4.4: Observed frequency of O vacancy diffusion events as function of O_2 exposure.

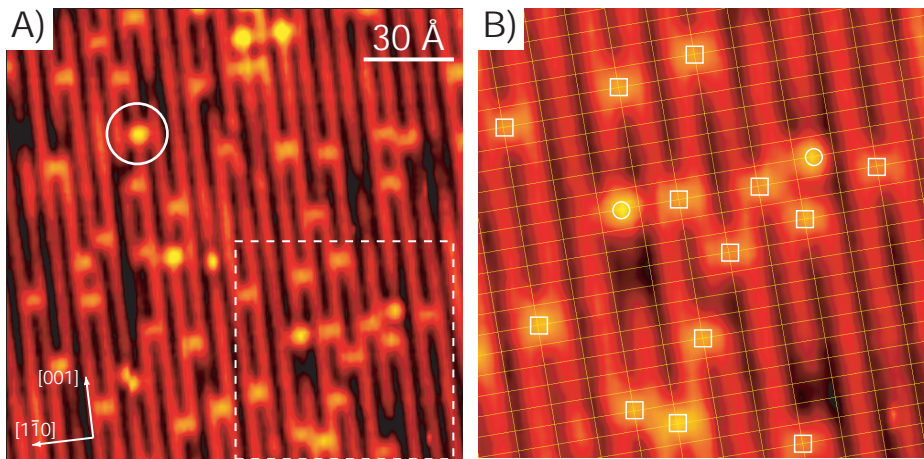


Figure 4.5: (A) STM image recorded at 220 K. Besides the O vacancies, additional features ascribed to adsorbed O_2 are distinguished. (B) High-resolution STM image showing that O_2 molecules adsorb on top of five-fold coordinated Ti atoms. The surface lattice locked on the bridging O atoms is superimposed. Squares locate vacancy sites, whereas circles locate O_2 molecules.

molecule cracker onto the clean $TiO_2(110)$ surface. This gives a significant *increase* in the number of vacancies indicating that atomic oxygen will react with bridging oxygen atoms and form molecular oxygen and vacancies. In fact, the number of protrusions appearing on Ti rows after atomic O exposure showed a 1:1 correlation with the increase in number of O vacancies (Figure 4.6). The protrusions observed after both O_2 and O

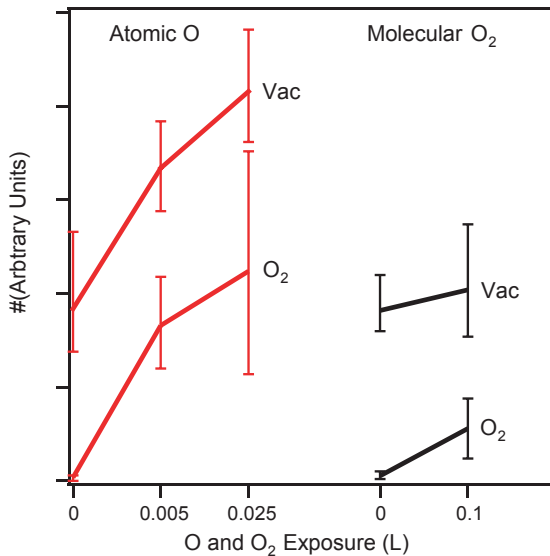


Figure 4.6: Graphs showing the effect of dosing atomic oxygen and molecular oxygen at low coverage at RT. Red graphs illustrate the 1:1 correlation between the number of created vacancies and the number of created protrusions. The black graphs do not show the same relationship after dosing molecular oxygen onto the surface, although at low dosage the number of vacancies can be seen to go up slightly.

exposures promote vacancy diffusion and are identical in appearance and dynamical behavior. (2) If the diffusing entity was a single oxygen atom as proposed by Henderson and coworkers [38,40], then during an oxygen vacancy diffusion event the oxygen atom would enter the vacancy without filling it, and it would then extract another oxygen atom from the next row without forming O₂. Both steps are highly unlikely.

These pieces of information provide evidence for the proposed process of O₂ molecule formation (step 4 in figure 4.8 (B)) in our diffusion model and for the identification of O₂ as the species mediating oxygen vacancy diffusion.

To verify that adsorbed molecules from the residual gases in the chamber were not the actual mediators, a series of experiments were made with both CO and CO₂, that confirmed that neither molecule activates the diffusion process. The presence of hydrogen in the vacancy and/or as part of the diffusing entity on the surface can not be entirely ruled out, since hydrogen rarely is seen in STM images [114]. No hydrogen dosing experiments made, have been able to affect the characteristics of the diffusion.

To exclude tip-vacancy interactions, several movies were made where the scanning direction was rotated 90 degrees. The diffusion behavior was not affected by this. Scanning was done with tunneling voltage V_t = 1.3 V and tunneling current I_t = 0.2 nA (R_t = 6.5 GΩ), which minimizes tip-sample interactions [75]. The STM tip only scans in the [110] direction, but a closer look at figure 4.3 shows that the diffusion of vacancies

at those conditions is equally probable in the $[1\bar{1}0]$ and the $[\bar{1}10]$ directions. This also indicates that the tip is not affecting the diffusion. Diebold proposed in [75] that the diffusion is tip induced and she found no trace of correlation between the diffused vacancies. These observations could very well be due to differences in sample preparation and lack of temporal resolution, since the STM used in those investigations use 20-30 seconds per frame, when recording a $300 \times 300 \text{ \AA}$ image [117].

4.2 Diffusion Mechanism

The protrusions assigned to oxygen molecules are responsible for the main part of the interactions with the vacancies. At low temperatures, these protrusions appear to be confined within a Ti row limiting the movements to be along the $[001]$ direction, unless a vacancy is encountered. 4 different results of an encounter have been witnessed (see figure 4.7 (1) to (4)). The particle can move past the vacancy, and flip the vacancy across the row (1). It can in the simplest case move past the vacancy without moving the vacancy (2). It can diffuse through the vacancy to the next row either leaving the vacancy in its original position (3), or flipping it onto the next row (4).

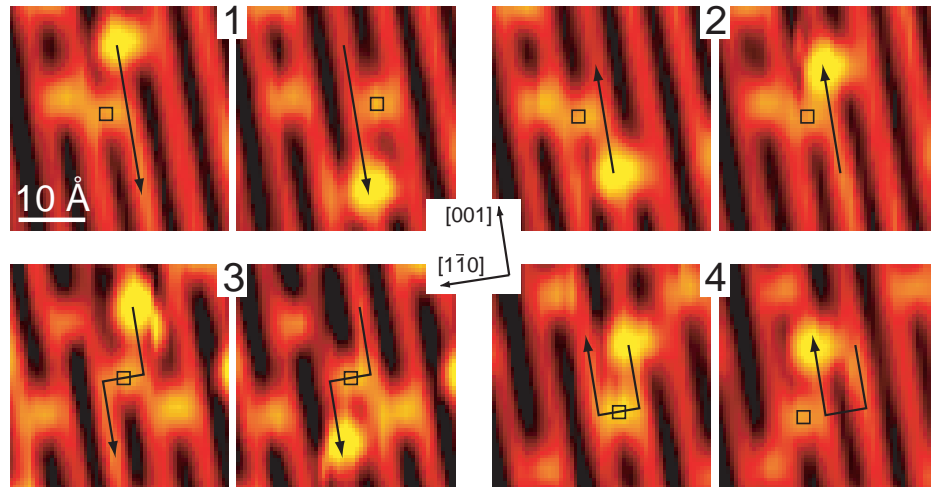


Figure 4.7: STM images showing the four different initial and final configurations resulting from the encounter between oxygen vacancies and O_2 molecules. To each of these correspond an atomistic pathway as shown in figure 4.8. The squares denote vacancy positions and the arrows indicate the diffusion path of the O_2 molecules.

These observations and the identification of the protrusions as molecular oxygen leads us to the following model for the vacancy diffusion (see figure 4.8).

When an adsorbed oxygen molecule encounters a vacancy it forms an intermediate complex with the vacancy (step 1). The intermediate complex is unstable and the

molecule dissociates filling the vacancy with one of the oxygen atoms, leaving the other oxygen atom in one of the Ti rows (step 2). This oxygen atom is highly reactive and forms an oxygen molecule with one of the bridging oxygen atoms next to it. This procedure recreates the vacancy in one of 3 different positions (step 3). The four different outcomes of the diffusion, shown in figure 4.7, correspond directly to the ones shown in figure 4.8.

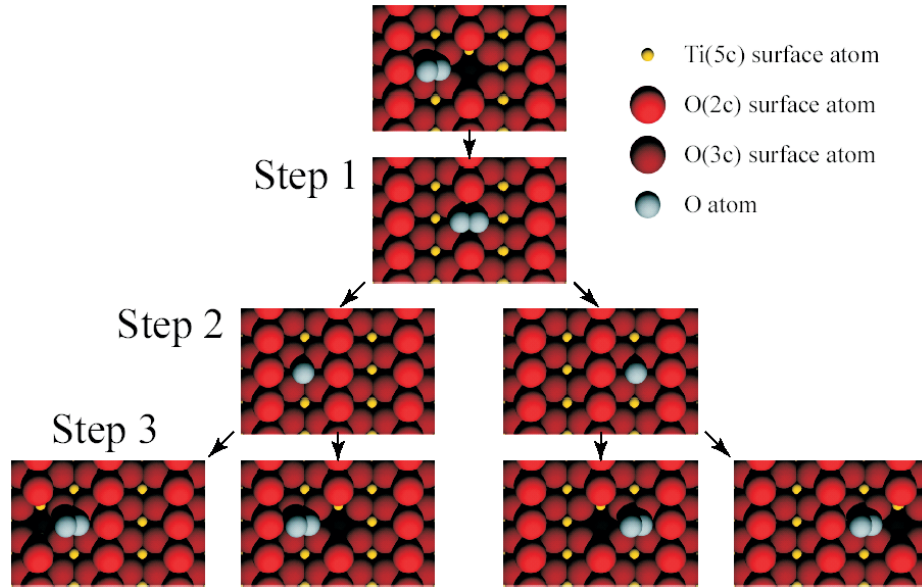


Figure 4.8: The diffusion mechanism consisting of 3 steps. (Step 1) The adsorbed oxygen molecule encounters a vacancy and forms an intermediate complex. (Step 2) The complex is unstable and dissociates, leaving an oxygen atom in one of either neighboring rows (per symmetry). (Step 3) The highly reactive oxygen atom reacts with a bridging oxygen atom, leaving an oxygen vacancy behind in one of 3 different positions.

No other final configurations than the four discussed above were observed. Each of these diffusion mechanisms involves two meta-stable, intermediate states. The first one consists of an O₂ molecule bound to an oxygen vacancy (step 2 in Fig. 4.8) and the second one consists of a single O atom located on a Ti site neighboring the initial vacancy position (step 3 in Fig. 4.8).

The first intermediate state was in our previous publication [118] identified as the O₂/vacancy complex found by Lu *et al.* [44] when depositing O₂ at 105 K onto the TiO₂(110) surface. This complex is not stable at temperatures above 180 K [40], and it was believed that the oxygen molecule would be trapped in a meta-stable state in the vacancy at the temperatures of our diffusion experiments (180 to 250 K). Very recent findings suggest that a charging of the diffusing molecular oxygen is causing the diffusion of the molecule into the vacancy, where it de-charges and fills the vacancy while

expunging the left-over oxygen atom onto the Ti rows. This new model for oxygen diffusion will be discussed in more detail in chapter 7.

The second proposed intermediate state was directly observed in some diffusion events as illustrated in figure 4.9 by three consecutive STM images [identical to mechanism (4) described in Fig. 4.7 (4)]. It appears as a very bright protrusion, readily dis-

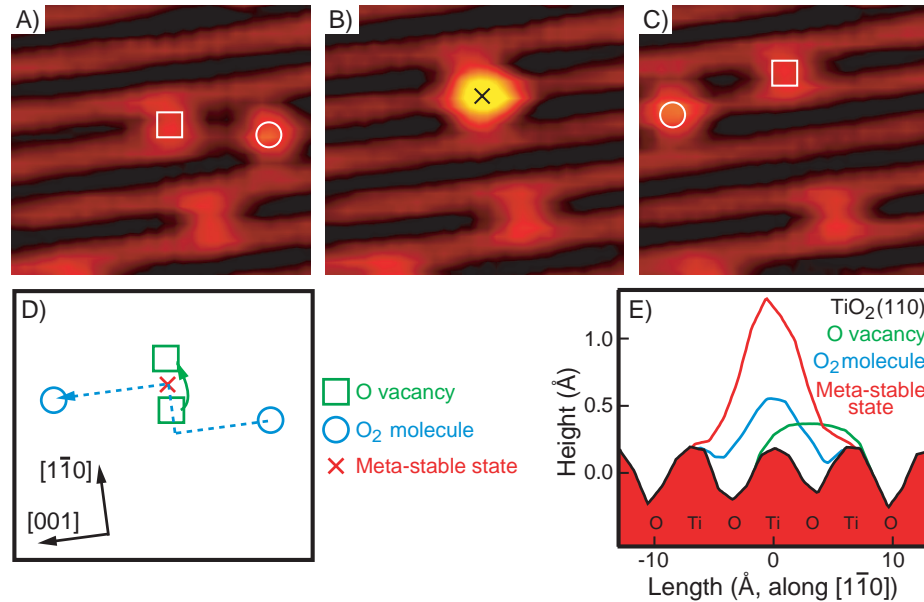


Figure 4.9: (A) to (C) Three consecutive STM images (1.1 s/frame at 230 K) showing the O₂-mediated diffusion of an oxygen vacancy. The process involves an intermediate state seen as the bright protrusion located on a Ti atom, in between the initial and final positions of the vacancy. (D) Schematic drawing of the diffusion event. (E) Line profiles illustrating the heights measured by STM of oxygen vacancies (green), O₂ molecules (blue) and intermediate states (red) involved in the diffusion process. The corrugation of the TiO₂ surface is also reported (black). All profiles were acquired perpendicular to the bridging O rows.

tinguishable by its height from other species present on the surface, imaged 0.9 Å and 0.7 Å higher than an O vacancy and an O₂ molecule, respectively (Figure 4.9 (E)). The bright protrusion is adsorbed on top of the Ti atom located in between the initial and final positions of the oxygen vacancy. The bright protrusion is therefore identified as being a single O atom adsorbed on a Ti site (step 3 in Fig. 4.8).

Different models have been proposed [38, 39, 75] to describe the healing of O vacancies (filling by an oxygen atom), observed when depositing O₂ on the TiO₂(110) surface. These models rely on the mechanisms described in step 1 to step 3 in Fig. 4.8. Subsequent to step 3, the O adatom is however proposed to diffuse along the Ti

rows and heal another vacancy. In the STM movies it is never observed that single O₂ molecules are responsible for vacancy healing (in more than 100,000 events) under the present circumstances.

4.3 Conclusion

A model for the mediated diffusion of oxygen vacancies has been proposed in this section, describing the creation of an intermediate complex consisting of an oxygen molecule and a vacancy. This complex dissociates to heal the vacancy with one of the oxygen atoms, while the other oxygen atom moves to the Ti row next to the former vacancy. Here it subsequently reacts with a bridging oxygen atom to recreate the vacancy in one of 2 different positions.

The model presented in this section is not only self-consistent, but also consistent with previous publications, though it brings about new and probably very important knowledge about the oxygen chemistry on the TiO₂(110) surface. The present observations dismiss the idea that oxygen vacancies fill up at the first encounter with an oxygen molecule, and since the vacancy is the active site on the TiO₂(110) surface, it is important to obtain this information. The second intermediate state is a relatively long-lived highly reactive oxygen atom, which could very well turn out to be important in surface processes involving other atomic and molecular species on the surface. In chapter 7 the diffusing oxygen molecule will be discussed based on the most recent findings.

CHAPTER 5

Vacancy-Vacancy Interactions on $\text{TiO}_2(110)$

Understanding the bridging oxygen vacancies on the $\text{TiO}_2(110)$ surface is essential to obtain a detailed knowledge about the atomistic processes on the surface. When investigating the distribution of the vacancies on the surface in detail, we find that the interaction between the vacancies is repulsive with a strong anisotropy, indicating an interaction of up to 18 Å along the bridging oxygen rows, while the interaction perpendicular to the rows is very small. The anisotropic interaction is shown to cause the vacancies to create strand-like formations on the surface. The two dimensional pair potential between single pairs of vacancies is found through Monte Carlo simulations and explained by electrostatic interaction and surface relaxation around the vacancies.

The chapter is based on paper III.

5.1 Introduction

The most abundant surface defects on the thermally annealed TiO₂(110) surface are the bridging oxygen vacancies, which are also the primary adsorption sites on the surface, whether it be for small gas molecules or metal atoms.

Despite this well-known fact, the distribution of vacancies on the surface has not been investigated in detail. The only two references to the distribution of the vacancies were written by Diebold and coworkers:

"...they are only one atom wide, with no tendency to agglomerate along the [001] direction, consistent with single missing oxygen atoms." [75]

"They always appear as isolated spots with no apparent short-range ordering, but a slight tendency to be staggered perpendicular to the rows." [34]

Taking a look at figure 5.1, it is easy to confirm that there indeed appears to be no vacancies in neighboring positions along the bridging oxygen rows, and as the coverage of vacancies goes up, the vacancies tend to line up next to each other both at directly neighboring sites and sites up to 3 lattice sites away on the neighboring bridging oxygen row, giving the visual impression that these strands of vacancies are stable configurations.

In this chapter the interaction between the vacancies is described in detail. It is shown that this interaction is of a different nature and much stronger than the forces between entities on surfaces previously studied, ie. adsorbates on metals.

On metal surfaces, the interactions between adsorbates or adatoms are caused by adsorbate induced changes in the surface electron gas, surface-induced charge redistribution on the adsorbates, and relaxation in the surface lattice [119, 120]. The adsorbate-adsorbate interaction has in both articles been shown to exhibit an oscillatory behavior with a typical metal on metal value of 2 meV at a distance of 10 Å [119, 120], whereas an investigation of N adatoms on Ru(0001) revealed intermolecular interactions on the order of 10-15meV [121]. The oscillatory potential found in metals is completely missing in this study, probably due to the lack of electronic states at the Fermi level, ie. few de-localized electrons.

A single study of vacancy interactions on a semiconductor (Ge) showed a short-range interaction of 0.2-0.3 eV between two vacancies in neighboring sites only. Beyond the first lattice site, the interaction was zero within the limits of the study [122]. With the chemical potential (Fermi level) at similar distances from the conduction band in the Ge (half of bandgap E_g=0.67 [71]) and the reduced rutile TiO₂ (Fermi level ~0.4 eV below the conduction band [101, 123]), the difference in interaction length therefore must lie in the respective covalent and ionic crystal bonding.

In this study, the first of its kind on metal oxides, a pair distribution analysis is used to find the effective potential between the adsorbates, and Monte Carlo simulations are used to find the pair potential between single pairs of vacancies [120, 121, 124]. Towards the end the pair potential is used to explain the strands described above and to visualize the entropic effects that arise from increased packing of vacancies on the surface.

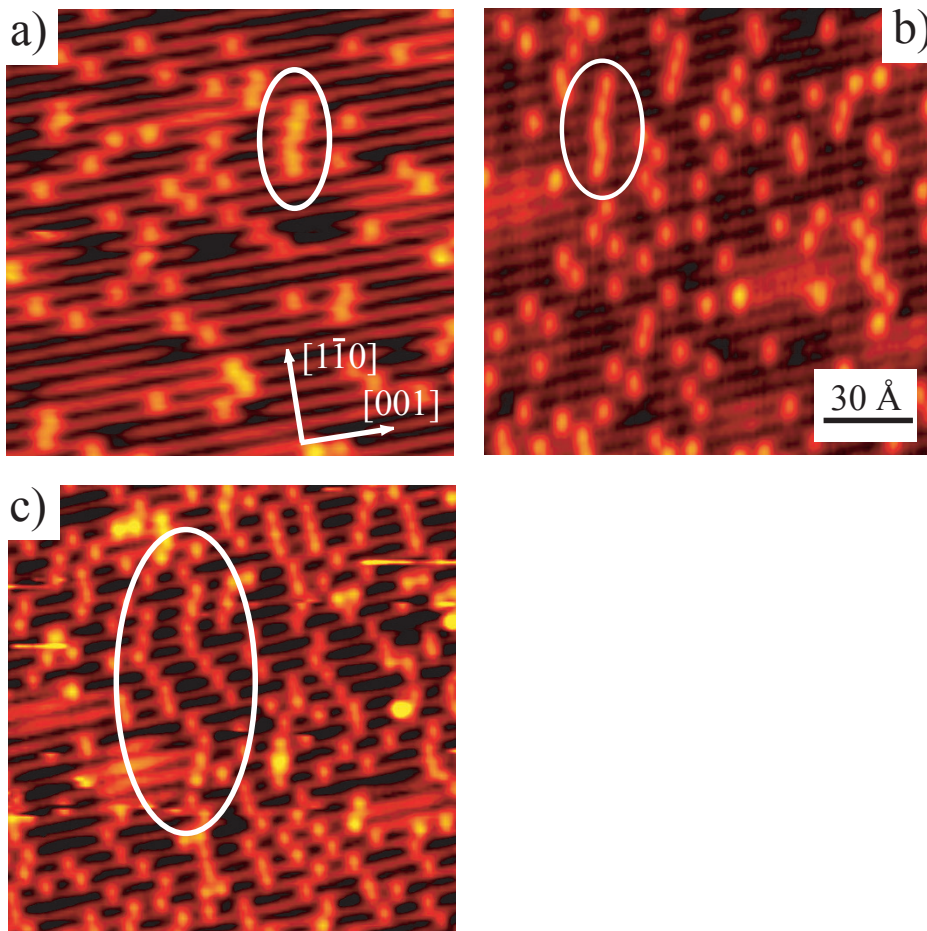


Figure 5.1: STM images of the $\text{TiO}_2(110)$ surface at three different coverages of bridging oxygen vacancies. (a) 4.9%, (b) 8.6% and (c) 14.4% vacancies. All images are $150 \times 150 \text{ \AA}^2$. The tendency to form strands with increasing coverage is illustrated by the elliptical markers.

5.2 The Pair Distribution

The spatial distribution of vacancies on the $\text{TiO}_2(110)$ surface is not homogeneous, but rather it depends on the thermodynamic fluctuations in the system. The vacancies diffuse on the surface, and the distances between the vacancies change accordingly. If one represents the distance between all pairs of vacancies in the so-called *pair distribution*, one effectively gets the average distribution. The pair distribution is used to find the effective potential.

The pair distribution for particles in a two-dimensional lattice gas with distinct lattice sites enumerated by j is given by [121]:

$$g_{eff}(j) = \frac{1}{N\Theta} \sum_{i=1}^N \frac{n_i(j)}{m(j)}, \quad (5.1)$$

where $n_i(j)$ is the number of j th-nearest-neighbor vacancies around the i th vacancy, N the number of vacancies, Θ the coverage, and $m(j)$ the number of symmetric j th neighbor sites. On the TiO₂(110) surface m is 2 along the symmetry axis and 4 on the rest of the surface (due to the two mirror planes). The function is normalized by Θ , so that $g_{eff}(j)$ goes to unity as j goes to infinity. The pair distribution can be interpreted as the ratio of the probability of finding a vacancy at a certain site, j , divided by the average occupation probability. In the case of a purely random distribution the pair distribution is unity for all values of j . Deviations from $g_{eff}(j) = 1$ thus denote deviations from the non-interacting case [121].

In the present work, the pair distribution function is found via the autocorrelation plot, which is a density plot of all separation vectors between vacancies in an STM image. This autocorrelation plot is added to the autocorrelation plots for the other images with the same coverage. This corresponds to the summation in equation 5.1.

Due to the finite size of the STM images (300×300 Å), which makes the autocorrelation fall off to zero at 300 Å, a geometric factor is used to normalize the autocorrelation. After normalization, a sine is fitted to the autocorrelation along the two symmetry axis to determine the lattice constants. With the correct lattice constants, the distinct lattice sites are determined and $g_{eff}(j)$ is found.

The occupation probabilities are Boltzmann distributed at thermal equilibrium as [125]

$$g_{eff}(j) = e^{-\frac{V_{eff}(j)}{k_B T}},$$

where $V_{eff}(j)$ is the mean effective potential, and k_B , T are the Boltzmann constant and the temperature respectively.

It is important at this point to understand that the mean effective potential, $V_{eff}(j)$ arises from interactions with an ensemble of vacancies, reflecting the number of different forces acting on the vacancy from many other vacancies and the substrate such as coulombic forces, van der Waals forces, steric hindrance etc. The pair potential, which is the potential working between a pair of isolated particles, is the really interesting potential here because it can be compared to theoretical calculations and it can be used in Monte Carlo simulations of the surface. In the low density/short interaction field case the effective and the pair potential should be almost the same [120, 121], but when a larger number of vacancies are present on the surface, they have a larger probability of occupying a lattice site within the interaction field of several vacancies, giving rise to an effective potential that appears smaller than the pair potential. We shall refer to the differences in the effective potentials occurring from increased packing of the vacancies on the surface as *entropic forces* after the work of Trost *et al.* [121], and return to it towards the end of this chapter.

The pair distribution does not reveal anything about so-called second order effects. Second order effects arise from multi-body interactions, ie. three or more vacancies close to each other might repel each other more or less than the pair potentials would show. This effect plays a role in the current study and will be discussed later.

5.3 Static Distribution

To discuss the "static" distribution, the mobility of the vacancies needs to be addressed. In chapter 4 it was shown how the vacancies diffuse on the surface. The diffusion is bound in one dimension, ie. it proceeds perpendicular to the bridging oxygen rows. The effect of the bound diffusion is discussed in section 5.5.

The primary part of the STM images used in this study are taken from 3 different STM movies leaving enough time between chosen images to ensure that all vacancies have diffused several times. No development is seen in the measured pair distribution functions as a function of time. Images on other parts of the surface have also been analyzed to ensure that each found distribution describe the distribution of the entire surface.

In order to investigate the influence of closer packing of vacancies on the surface, we studied the clean $\text{TiO}_2(110)$ surface at RT with coverages of 4.9%, 8.6% and 14.4% bridging oxygen vacancies (figure 5.1 (a), (b) and (c) respectively). As noted in the introduction, images acquired at all three different vacancy coverages show that vacancies very rarely occupy sites separated by only one lattice constant along the bridging oxygen rows indicating a strong repulsive interaction along the row. A few neighboring vacancies are found in the high coverage cases. Vacancies have a tendency to line up next to each other both at directly neighboring sites and sites up to 3 lattice site away on the neighboring bridging oxygen row, giving the visual impression that entire strands of vacancies are building up (figure 5.1 (c)).

The discrete pair distribution was acquired, according to the procedure discussed above, for each coverage case. Figure 5.2 shows both the autocorrelation plot for the 8.6% case and the discrete pair distribution for the 14.4% case. The side lengths of the cells chosen in the figure are proportional to actual lengths in the (1×1) surface unit cell illustrating the anisotropy of the interactions.

It is immediately clear from the figure that:

- There is a strong interaction along the bridging oxygen rows, extending quite far.
- The effect on the neighboring row is not very large.
- There is a contribution to the pair distribution from the strand formation, but since it extends over several lattice sites on the neighboring row, it is hard to make quantitative comments on it.

Looking closer at the pair distribution along the [001] direction (fig. 5.3), it shows a significant repulsive interaction as far away as the 6th lattice site along the [001] rows. The interaction perpendicular to the rows, along the $[1\bar{1}0]$ direction, is relatively small

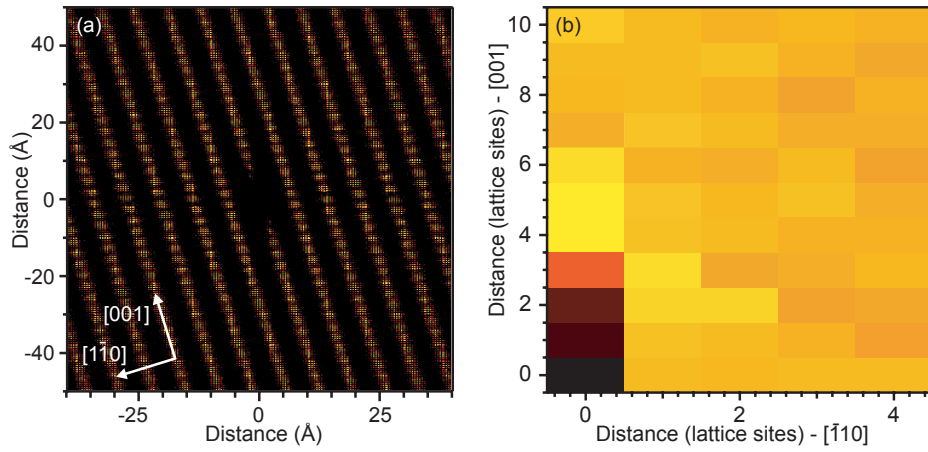


Figure 5.2: (a) Autocorrelation plot for the 8.5% case. (b) Discrete pair distribution for the 14.4% case illustrating the anisotropy of the surface interactions. The relative side lengths of the cells in the figure are proportional to the side lengths of the surface unit cell.

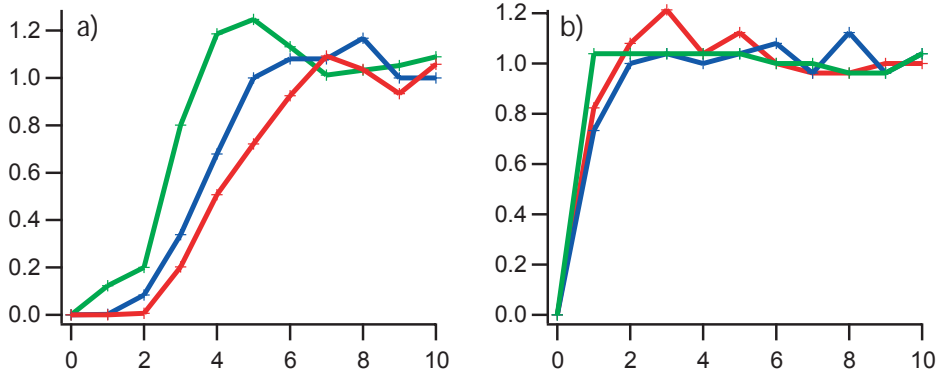


Figure 5.3: Pair distribution with 4.9% (red line), 8.6% (blue) and 14.4% (green) vacancies. (a) along the bridging oxygen rows, (b) perpendicular to the bridging oxygen rows. The pair distribution was found by counting all separation vectors between 19509 vacancies in 38 different images.

compared to the one along the [001] direction. The low coverage case only has a probability 0.68 to find another vacancy at a neighboring site. At higher coverages, the interaction appears to become negligible, while at the same time, in the area between the symmetry axis, indications of an apparent attraction can be seen in the 14.4% case. This fact will be discussed in section 5.6.

5.4 The Effective Potential

From equation 5.1 the effective potential for each coverage of vacancies can be found, given the pair distribution functions in figure 5.3. The values for the effective potentials along the [001] direction are shown in table 5.1 and in figure 5.4.

$j_{[001]}$	$V_{4.9\%}/meV$	$V_{8.6\%}$	$V_{14.4\%}$	$V_{\text{pair, MC}}$
1	—	$163 \pm 10^*$	$54 \pm 10^*$	1000^{**}
2	130 ± 26	64 ± 1	42 ± 1	136 ± 1
3	41 ± 5	28 ± 1	6 ± 1	46 ± 1
4	18 ± 3	10 ± 1	-4 ± 1	22 ± 1
5	8 ± 2	0 ± 1	-6 ± 1	11 ± 1
6	2 ± 2	-2 ± 1	-3 ± 1	4 ± 1

Table 5.1: *Effective potentials along the [001] direction found from experimental data, and the pair interaction potential found from the Monte Carlo simulation. $j_{[001]}$ is the lattice site along the [001] direction, where the first 6 are used in the analysis. All values given in meV. Uncertainties are based on the statistical analysis. Numbers marked with * and ** will be discussed in the text.*

The effective potential in the 4.9% case is purely repulsive with a monotonic decrease. When the coverage is increased the effective potentials change as expected: The effective potentials become less repulsive and in the high coverage case the effective potential even becomes attractive between the 4th and 6th lattice sites. These effects are due to the before-mentioned entropic forces and will be explored further in section 5.6. At the lowest coverage, no cases of neighboring vacancies were found in the STM images, while in the 8.6% and 14.4% cases a few neighboring vacancies were observed. These so-called double vacancies can be very hard to identify, and while significant effort has been put into the differentiation between vacancies and double vacancies, most probably a number of vacancies have been counted as double vacancies. The $V(1)$ effective potential for the 8.6% and 14.4% case (marked * in table 5.1) should thus be seen as lower bounds for the effective potential at these coverage.

As stressed previously the effective potential does not directly reveal the pair potential between an isolated pair of vacancies. This has to be found by means of Monte Carlo simulations. The MC potential value marked ** in table 5.1 will be discussed in section 5.5.

5.4.1 Vacancy Coverage

As mentioned before the distribution of bridging oxygen vacancies is not entirely homogeneous, and steps and the so-called type B defects in the surface appear to have a slightly repelling effect on the vacancies. This means that the coverage changes from image to image. We have chosen to use the general average of the number of vacancies in the images used in the analysis. The coverages found are then: 4.9% ($\pm < 0.1\%$),

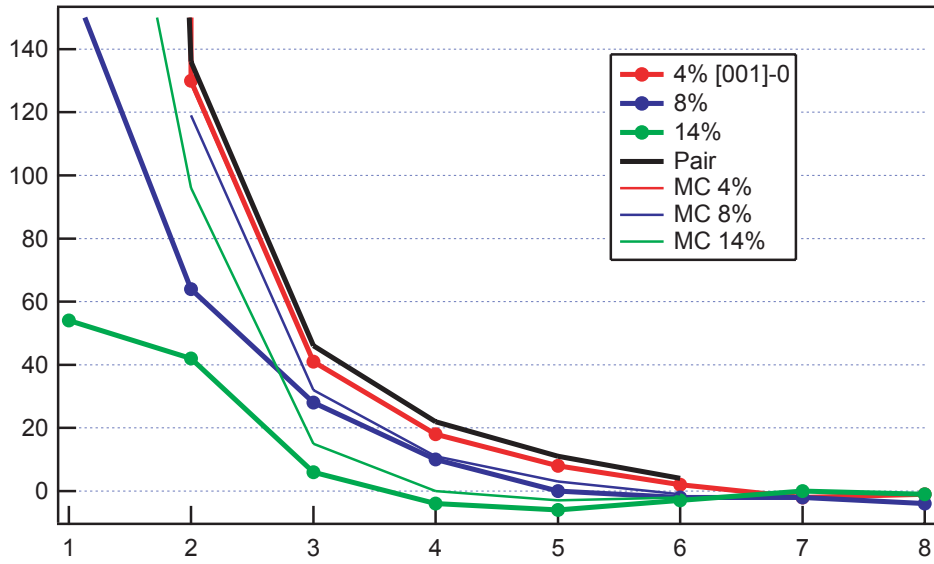


Figure 5.4: The experimental effective vacancy-vacancy interaction along the [001] direction extends to affect neighbors as far away as the 6th lattice sites. The thick black line is the common Monte Carlo pair potential and thick lines with markers show the experimentally found effective potentials. The thin lines are the corresponding effective potentials found with the MC simulation.

8.6%($\pm 0.1\%$) and 14.4%($\pm 0.2\%$), where the uncertainties are the statistical uncertainties from the averaging procedure.

5.5 Monte Carlo Simulations

Monte Carlo (MC) simulations were performed to simulate the repulsive interaction between the bridging oxygen vacancies. In order to fully understand the MC simulations, the basics of MC simulations, the Metropolis algorithm and the ergodic hypothesis are treated first [126].

In classical Monte Carlo the average of a given variable for a system is the weighted average over random points in phase space, where each ensemble is equally probable. The ensemble average is

$$\langle A \rangle = \frac{\int A(\vec{r}) \exp\left(\frac{-E(\vec{r})}{k_B T}\right) dr}{\int \exp\left(\frac{-E(\vec{r})}{k_B T}\right) dr}, \quad (5.2)$$

where A is the variable of interest, E is the energy of the configuration at the given point \vec{r} in phase space. Each value in phase space has probability 1, but is weighted with the

Boltzmann weight

$$Q^{-1} \exp\left(\frac{-E(\vec{r})}{k_B T}\right), \quad (5.3)$$

where Q is the partition function in the denominator of equation 5.2.

This way of sampling means that high energy configurations become negligible in the averaging procedure [127, 128]. Metropolis et al. [127] employed for the first time in 1953 a modified Monte Carlo scheme (the Metropolis Algorithm). The basic idea is to let the system evolve towards an energetic minimum, where consecutive states (points in phase space) can be probed to give a faster evaluation of the average of an observable. The procedure of creating a series of states from an original one is known as a *Markov Chain*, which is a central concept to Monte Carlo simulations. The basic idea is that the state at a given time completely determines the future evolution of the system. No memory of the previous evolution of the system is kept or needed. A new configuration is formed from the previous one, based on the transition probability, $w(\vec{r}_1 \rightarrow \vec{r}_2)$, as:

$$w(\vec{r}_1 \rightarrow \vec{r}_2) = \min\left(\exp\left(\frac{-(E(\vec{r}_2) - E(\vec{r}_1))}{k_B T}\right), 1\right). \quad (5.4)$$

The probing of the relevant parts of the phase space proceeds in the following manner:

1. N particles are placed in any configuration in a lattice.
2. The energy of the system's state is calculated, E_1 .
3. One of the particles is moved randomly on the surface.
4. The energy of the new state is calculated, E_2 .
5. If $E_2 \leq E_1$ then the new state is kept, otherwise...
6. If $E_2 > E_1$ then a random number ϵ is chosen in the interval $0 \leq \epsilon \leq 1$, and ...
7. If $\exp\left(\frac{-(E_2 - E_1)}{k_B T}\right) < \epsilon$ then the new configuration is kept. Otherwise the particle is moved back and this configuration is used in the averaging procedure, which will be discussed below.
8. Steps 3-7 are repeated until the energy of the system no longer evolves.

Using the Metropolis Algorithm, the average of an observable will be found from the M last steps in the simulation.

$$\langle A \rangle = \frac{1}{M} \sum_{m=N-M}^N A_m, \quad (5.5)$$

where A_m is the value of the observable after step m. This procedure eliminates the influence on the original (and physically meaningless) configuration, when (N-M) is chosen after the energy of the system is minimized. For the Metropolis algorithm to

be valid, it is essential that the random walk is ergodic, that is that any point \vec{r}_n in configuration space may be reached from any other point \vec{r}_1 . If parts of configuration space are difficult to reach, long simulations or a modification of the algorithm can be necessary. Because of the anisotropy of both the diffusion and vacancy-vacancy potential, we have chosen to probe phase space slightly different, as will be explained below.

To simulate the equilibrium configuration of the surface, we create a lattice with the same size as a 300×300 Å STM image (46×101 unit cells) with periodic boundary conditions. A number of vacancies corresponding to the required coverage of vacancies are created randomly on the surface.

Since the diffusion of vacancies only proceeds perpendicular to the bridging oxygen rows [118], this process is mimicked in the MC simulations. A random site is chosen on the surface along with a random pick of one of its neighboring sites on the adjacent rows. If only one of the two chosen sites contain a vacancy, a move is attempted within the rules of the Metropolis algorithm outlined above.

The pair potential used to describe the interaction between two vacancies on the surface is a two dimensional potential which affects the surrounding vacancies when located on the same [001] row and on the two neighboring rows. This potential has been shown to reproduce the experimental data.

The energies used in all the calculations (meaning for all coverages) are given as the sum of energies from this common pair potential. The energy, E, of a diffusing vacancy is given by:

$$E_{[0,0]} = \sum_{i \in [-1,1]} \left(\sum_{j \in [-6,6]} V_{pair}(i,j) \delta(i,j) \right), \quad (5.6)$$

where (i, j) is the numbered lattice sites on the i th row and the j th site along the [001] direction relative to the vacancy, V_{pair} is the pair potential, and $\delta(i,j)$ is unity when there is a vacancy at lattice site (i, j) and otherwise zero.

An appropriate number of attempted diffusion events ensure that an energetic equilibrium is reached. At a coverage of 14% 700,000 attempts to diffuse give an average of more than 33,000 actual diffusion events, or more than 55 diffusion events per vacancy. When energetic equilibrium is reached, the program calculates the pair distribution on the surface and the corresponding effective potential, and compares it to the experimentally found effective potential.

Creating a random distribution of vacancies and restricting their diffusion on the surface will not allow the simulations to explore the entire configuration space which is required for the Metropolis algorithm to be valid, eg. probing consecutive configurations as in equation 5.5 could give a wrong average due to the restriction on the phase space. This problem can be overcome by creating a large number of initial configurations and probing them each once after they have relaxed energetically. Thereby a larger part of phase space is explored and the ergodicity of the simulations is restored [126]. The

average of an observable then becomes:

$$\langle A \rangle = \frac{1}{m} \sum_{l=1}^m A^{(l)}(t), \quad (5.7)$$

where $A^{(l)}(t)$ is the observable A observed at (simulation) time t in the l th run of the m independent simulations performed.

The simulations are run until the energy has equilibrated. Then we probe once, and start the simulations over with a new initial configuration. This is done 20,000 times for each coverage, at which point the standard deviation of the values of the pair distribution extracted are less than 0.5% in the 4.9% case and 0.2% in the 14.4% case.

As mentioned previously the pair distribution is per definition normalized to one for values beyond the interaction field. In the simulations the pair distribution is normalized in a simple way. For each coverage, 50,000 simulations are made with no interaction between the vacancies. This gives us the corresponding non-interaction pair distribution, which is subsequently divided into the interaction pair distribution to give a normalized distribution. This normalization procedure also eliminates the finite-size problem with the STM images.

Second order effects (due to multi-body interactions) are seen to affect the effective potential at higher coverages through the misfit between the experimental and the simulated effective potentials (figure 5.4). Despite this, second order effects are not taken into account in the present calculations, partly since the interaction is found to be purely repulsive, and partly because of the lack of information about the actual mechanisms causing the second order effects.

To minimize the impact of the second order effects, the pair potential is tuned to reproduce the experimental data (the effective potential) for the 4.9% coverage case through a 12 parameter least squares (χ^2) minimization. The simulated effective potentials for the 4.9%, 8.6% and 14.4% cases shown in figure 5.4 are based on this pair potential.

The restriction of the diffusion turns out to give a higher pair potential than if the diffusion in the simulation was allowed to happen between two random sites (that could be far from each other) on the surface. When the diffusion of a vacancy is restricted, the vacancy is more likely to move into the interaction field of another vacancy due to it's relatively higher attempt frequency. This causes the effective potential to become lower, and thus the pair potential must be higher to fit the experimental observations. The difference in the pair potential without and with restricted diffusion is of the order 5%.

The strand formation observed in the STM images (figure 5.1) is also observed in the MC simulations. The strand formation is not dependent on the restricted diffusion, as can be seen from figure 5.5, where simulated STM images with and without restricted diffusion are indistinguishable. The strand formation is not seen, when there is no pair potential between the vacancies in the simulations, instead double and even triple vacancies form.

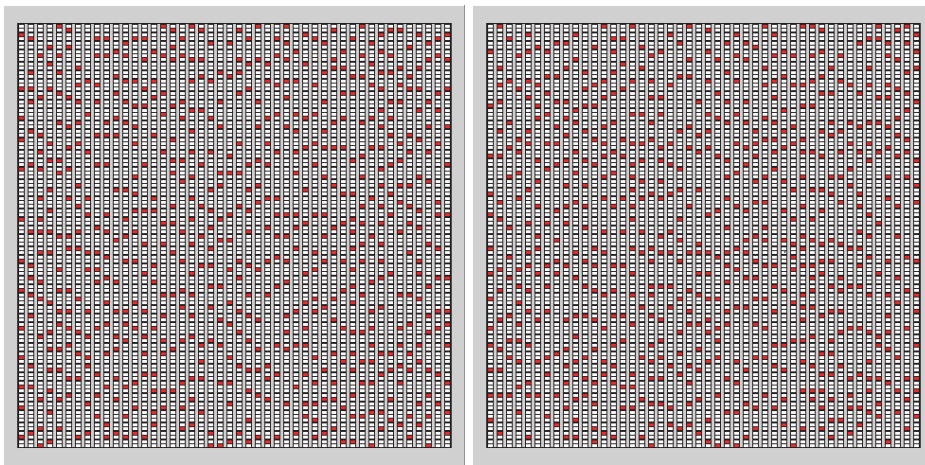


Figure 5.5: *Simulated STM images of the TiO₂(110) surface with 14.4% vacancies. The strand formation is clearly observed both (a) without and (b) with restricted diffusion. Both images are 300 × 300 Å².*

5.6 The Pair Potential

The pair potential found from the Monte Carlo simulations is shown in figures 5.4 to illustrate the relative size of the effective potentials. Generally it is interesting to notice that, along the [001] direction, the pair potential is found to be purely repulsive with an monotonic decrease that levels out around the 6th lattice site ($\sim 18 \text{ \AA}$). The values for the pair potential can be found in table 5.1 on page 45.

As mentioned previously the nearest neighbor effective potential along the [001] direction, $V(1)$, found at 8.6% and 14.4% coverage is a lower limit, due to difficulties in the analysis of the vacancies. At 4.9% coverage, there are no observations of double vacancies, which gives another way to find an estimate for the lower limit of the pair potential at the first lattice site. The lack of double vacancies means that the probability of forming a double vacancy is less than 1 in the 4486 counted vacancies on the surface (at 4.9%). This would indicate that $V(1) \geq -kT \ln(1/4486) = 217 \text{ meV}$.

To find the interaction on the adjacent rows, the nearest 9 sites on each of the adjacent rows were used in equation 5.6. The full 2-dimensional potential is given in table 5.2. The interaction on the adjacent rows is relatively small compared to the interaction along the row, but has an effect on the pair potential along the rows, which is lowered closer to the 4.9% effective potential and gives a better fit to the 8.6% and 14.4% cases.

The repulsive interaction between vacancies on the TiO₂(110) surface can be explained by two effects; electrostatic repulsion due to the loss of a neutral atom in the ionic crystal, and relaxations in the surface region. Both of these effects display a repulsive interaction which varies as $1/d^3$, where d is the distance between interacting vacancies [129, 130]. A $1/d^3$ fit to the pair potential gives reasonably good agreement,

$j_{[001]}$	$V_{\text{pair, MC}}(0, j)$	$V_{\text{pair, MC}}(1, j)$
0		4
1	1000	6
2	136	4
3	46	3
4	22	1
5	11	0
6	4	0

Table 5.2: *Pair potential used in the Monte Carlo simulation. $J_{[001]}$ is the lattice site along the [001] direction. All values given in meV.*

but since the two effects are indistinguishable in the current analysis, and since theory does not provide us with anything more concrete about the two effects, no basis is found for an analysis of the relative strengths of the effects.

When a neutral bridging oxygen atom is removed from the surface, creating a vacancy, two electrons are left in the vacancy due to the ionic nature of the crystal. These two electrons have been shown to relocate partly onto two previously six-fold coordinated Ti^{4+} atoms below, changing their formal oxidation state to 3+. The electrons are found in non-bonding, 3d-like conduction band levels localized primarily on the Ti atoms [74]. This relocation gives rise to the formation of two electrostatic dipoles in each vacancy, creating interactions between vacancies.

The charging of the neighboring Ti atoms causes a significant relaxation among the Ti and O atoms around the vacancy [74]. The relaxation has previously been underestimated because of the small surface super cells used in DFT calculations. Section 5.8 discusses the relaxations of the lattice and the theoretical findings in recent investigations.

The under-coordination of the Ti atoms readily explains the large repulsive interaction between first neighbors, since two vacancies next to each other effectively would cause one of the Ti atoms to become four-fold coordinated with two five-fold coordinated neighbors. This is energetically highly unfavorable and explains why, at the temperatures studied, there is no tendency to form rows of missing oxygen atoms, so-called vacancy islands, on the surface.

The large difference between the interaction along the rows and perpendicular to the rows is only in part due to the difference in the extent of the surface lattice in the two directions. The electronic effects from the remnant electrons are most likely attenuated significantly by the Ti (5f) rows that lie between bridging oxygen rows. Nothing is known about the relaxations of the lattice since no DFT calculations have yet worked with a super cell wider than 2 rows.

Despite the pure repulsion of the pair potential, the entropic effects caused by the packing of the vacancies on the surface at 14.4% vacancy coverage causes the effective potential to appear to be attractive at the 4th to 6th lattice site along the [001] direction.

The connection between V_{eff} and V_{pair} can be written as

$$e^{V_{eff}(j)/kT} = f(j, V_{pair}, \theta, T) e^{V_{pair}(j)/kT} \quad (5.8)$$

with an unknown function $f(j, V_{pair}, \theta, T)$. This corresponds to

$$V_{eff}(j) = V_{pair}(j) - kT \ln(f), \quad (5.9)$$

where the last term can be interpreted as an entropic contribution. This leads Trost *et al.* [121] to call the deviations of V_{eff} from V_{pair} *entropic forces*.

We have qualitatively investigated the effect of the entropic forces in the system as a function of the coverage of bridging oxygen vacancies. Again second order effects are not taken into account. Figure 5.6 (a) illustrates the development of V_{eff} along the [001] direction as the coverage increases from 0% to 50% in steps of 5%. As the

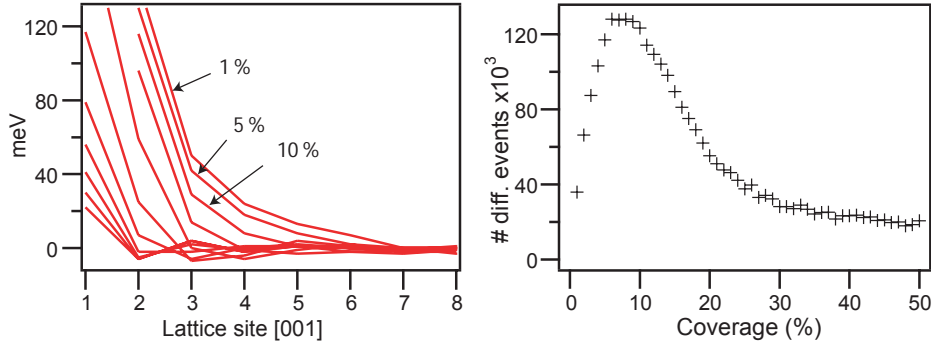


Figure 5.6: (a) V_{eff} as a function of coverage for the found pair potential. As the coverage increases, entropic effects cause packing of vacancies on the surface. (b) The number of actual diffusion events in the simulation as a function of coverage.

coverage is increased, the effective potential decreases at short distances. At coverages as low as 15% the effective potential becomes attractive at the 6th lattice site. As the coverage increases the apparent attraction in the potential moves towards lower values of j , which indicates a closer packing on the surface. At 25% the effective potential has two points of apparent attraction, which indicates the packing of vacancies on the surface at every other lattice site. An interesting feature is the effective potential at the first lattice site. With the pair potential set to 1000 meV, the simulations give no double vacancies (neighbors) for coverages up to 15%, while above that coverage it becomes possible for the vacancies to occupy neighboring sites. This way the simulation qualitatively explains the lack of double vacancies in the STM images in the 4.9% case, and the presence of them thereafter.

Figure 5.6 (b) shows the number of diffusion events as a function of coverage in 2,000,000 diffusion attempts. Not surprisingly the number of events exhibit a volcano style behavior. At low coverages the low number of vacancies will limit the number of

actual diffusion events, while at high coverages the restricted diffusion causes a lowering of the number of events.

As the pair potential reaches 6 lattice sites in each direction along the bridging oxygen row, the sites around a vacancy are effectively "blocked" for access by another vacancy, if it is within the pair interaction field. This effect is seen on the STM images as stranding of vacancies. Since the diffusion is blocked over quite a large distance, the stranding is spread out in the autocorrelation. Nonetheless an apparent attraction is seen in the experimental (and the calculated) effective potentials in the area between the symmetry axis. As the vacancy coverage increases this area with apparent attraction moves closer to the [1 $\bar{1}$ 0] axis, indicating that the strands become straighter as the coverage goes up.

5.7 Surface Energy

The TiO₂(110) surface is known to reconstruct under reducing conditions from a 1 × 1 to a 1 × 2 structure, although the atomic nature of the 1 × 2 reconstruction is still unknown [34]. The reconstruction begins to occur between 15 % and 25 % vacancy coverage depending on temperature and surface treatment. Small areas reconstruct, most probably as a response to a high local coverage of vacancies. By examining the total energy of the surface, as calculated with the Monte Carlo simulations, it is possible to give an estimate of the average energy per lattice site that is required for the surface to reconstruct. In figure 5.7 the average energy per lattice site on the surface is calculated as a function of vacancy coverage.

The calculations show that the average surface energy of every site on the surface increases exponentially to reach values of the order 12 meV/LS (per lattice site) at a coverage of 20 % and 26 meV/LS at 25 %. This surface energy can be directly compared to the outcome of DFT calculations.

5.8 DFT Calculations

The charging of the neighboring Ti atoms causes a significant relaxation among the Ti and O atoms around the vacancy. This study shows that with typical surface super cells of size (1 × 2), (2 × 2) or (3 × 2) [74, 87, 89, 131, 132] and cluster calculations [49], density functional theory (DFT) studies have previously not been able to detect the extent of the interaction between vacancies. According to preliminary DFT results on a 6×2 surface unit cell, the Ti atoms under the vacancy are charged positively and move away from each other due to electrostatic repulsion, causing the neighboring bridging O atoms to follow. 2nd and 3rd neighbor Ti and O atoms along the bridging oxygen rows are affected by this, and since this is the extent of the super cell, the interaction could very well be found theoretically as well to go beyond the 3rd lattice site. The four O atoms in the surface plane surrounding the vacancy move slightly closer to the Ti atoms [86]. This relaxation of the lattice acts to strengthen the bond between the under-coordinated Ti(5f) atoms and the oxygen atoms. The monotonic decrease in the pair potential along

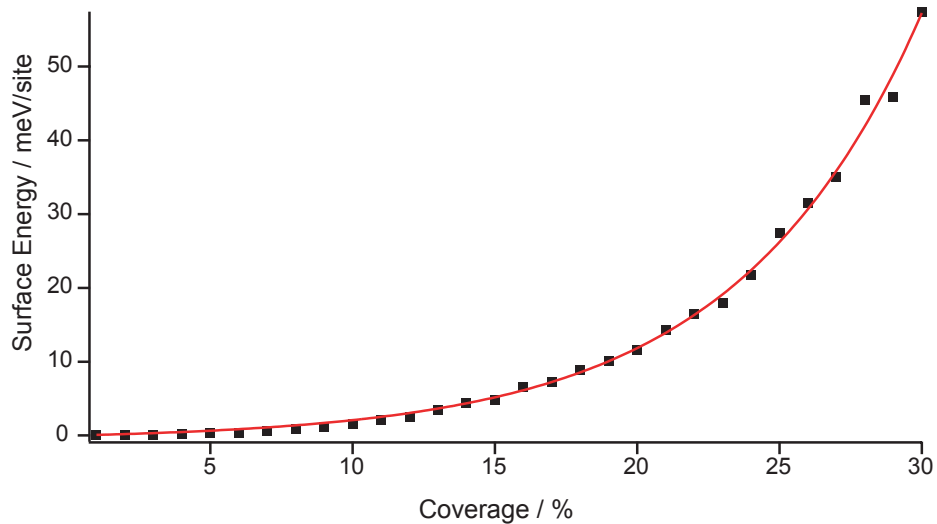


Figure 5.7: The surface energy per lattice site as a function of bridging oxygen coverage. The range up to a coverage of 30 % is plotted although the surface will reconstruct locally before this coverage. The red line is a fit to an exponential function to illustrate how fast the surface energy goes up.

the [001] direction is reproduced in the theoretical calculations, but the energetics are at this point not in agreement with our observations [86].

5.9 Conclusion

The current study has involved a detailed examination of the interaction between bridging oxygen vacancies on the TiO₂(110) surface. Through an analysis of a large number of high resolution STM images, we have found a highly anisotropic, long-range repulsive pair potential that describes the interaction between single pairs of vacancies on the TiO₂(110) surface. The pair potential is shown through Monte Carlo simulations to account for differences in the effective potential at different coverages and reproduces the apparent attractive effective potential found at high coverages. Strand-like formations of vacancies on the surface are explained by the anisotropy of the pair potential.

The implications of the repulsive and anisotropic potential are manifold. Vacancies are the active sites on the surface, and if they were to form vacancy islands, they would most likely reconstruct into a less reactive structure. The repulsive potential acts to maintain a high reactivity of the surface.

The abnormal anisotropy and the length of the interaction means that most (or all) DFT calculations performed previously on this system need to be reconsidered. The high interaction between vacancies in a small super cell could very well cause the predictions

of adsorption in the vacancies to become overly positive. Hopefully the near future will present some very exciting results from the theorists.

CHAPTER 6

Au on TiO₂

Studies of the model catalyst Au/TiO₂(110) in the temperature range 125 K to RT are presented. It is found that 0.005-0.04 ML Au deposited onto TiO₂(110) nucleate at bridging oxygen vacancies at all temperatures studied. At the lowest temperatures the single Au atom clusters are predominant, while an increase in temperature gives fewer and larger clusters tending more towards growth at step edges. A decrease in the number of vacancies with larger cluster size indicates that clusters at all temperatures grow on top of a number of vacancies that correspond to a Au atom - vacancy ratio of 3. With a larger ratio the clusters become mobile. DFT calculations are presented to support the experimental findings.

This chapter is based on paper II.

6.1 Motivation

The noble metal gold was considered to be of no interest to catalysis until 1989, when a study by Haruta [2] showed that Au nanoclusters on metal oxides are catalytically active in the CO oxidation process. The conversion of CO to CO₂ was shown to peak at a Au particle size around 3 nm, even at temperatures as low as 200 K [16]. Metal cluster - substrate interactions have been shown to play a significant role [3], but a scientific understanding of this phenomenon is still missing. The interactions leading to a high catalytic activity can be classified into three types [54]:

- The metal particles constitute the active phase. Metal particles with a size of less than 2-3 nm enter a regime, where quantum size effects significantly alter the electronic structure of the particle. The small particles are very susceptible to external influences like the interaction with a semiconducting support. Electron transfer between support and cluster further modifies the electronic structure of the metal [133].
- The interface between the metal particle and the support creates new reaction sites that favor the catalytic reaction [134]. The metal particle provides adsorption sites for at least one of the reactants, while the support may participate as a reactant reservoir. It is speculated that CO adsorbs on the Au particle while O₂ reacts from adsorption sites on the TiO₂ substrate [54, 135].
- The substrate is the catalytically active phase. The electronic structure of thin overlayers of the substrate covering the metallic particles is altered to activate the previously inactive substrate. This has been shown to work with TiO₂ on large ($\sim 1\mu m$) Au particles [136, 137].

All three of these cases depend heavily on the dispersion of the Au particles on the substrate surface, so the diffusivity and growth of the particles and thus the sintering of particles is very important to understand and be able to control.

Initially metal substrate interactions were shown to have a significant effect on the rate of conversion in the process, and TiO₂ was proven to be the substrate that gives the highest conversion of CO [3]. However, recent experiments on the catalytic activity of Au on Al₂O₃, SiO₂ and TiO₂ indicate that the substrate has little or no effect on activity, while the Au cluster size and thus the cluster perimeter interface appears to be a highly relevant parameter for the oxidation [134]. Experiments by Vannice and coworkers [136, 137], where TiO₂ was deposited onto large Au particles, showed high activity, suggesting again that the interface between Au and TiO₂ is where the CO oxidation takes place or that the immediate surroundings of the Au particles are altered to facilitate the oxidation process.

The present study focuses on the interaction between Au clusters and the substrate, and shows that the nucleation and growth of small Au clusters on the rutile TiO₂(110) surface is intimately related to the presence of surface oxygen vacancies.

By quantifying the temperature dependence (125 K – RT) of the cluster size distribution (0.005-0.04 ML) and the oxygen vacancy density, it is found that an oxygen vacancy on average accommodates 3-5 Au atoms. Medium-sized clusters (area $\sim 250 \text{ \AA}^2$)

are destabilized at room temperature (RT), indicating the mobility of Au-vacancy complexes.

Experimental findings are supported by density functional theory calculations that provide a model for the cluster growth mode.

6.2 Growth of Au Clusters on TiO₂(110)

Au was deposited from an e-beam evaporator (Oxford Applied Research). The Au evaporation rate was quantitatively calibrated from STM measurements of Au deposited at 300 K on a Ni(111) surface (see e.g. [138]) to be 0.01 ML/min (where one monolayer is defined as the packing density of an Au(111) plane, $1.39 \cdot 10^{15}$ atoms·cm⁻²). A +2.5 kV potential was applied to a nearby electrode in order to prevent any charged Au atoms from impinging on the sample surface.

The present investigations show that Au clusters are very weakly bound to the stoichiometric surface. At tunneling currents higher than 1 nA, a majority of the Au clusters disappear from the scanning area. This extremely weak binding of some of the clusters spurred the development of a new preamplifier to facilitate the lowest possible tunneling currents and high feedback gains. All presented STM images are acquired with 0.1 nA and 1.2 V.

In all images shown, the sample was cooled down from, or kept at, the deposition temperature during imaging. During sample transfer to the STM a short rise in temperature occurs, estimated to be 10-20 K.

Figure 6.1a shows an STM image of the clean surface prior to Au deposition. After Au deposition, Au clusters on the surface are observed (figures 6.1 (b) to (d)). The number of Au clusters increases with the amount of Au deposited. The size of the clusters depends on the deposition temperature. At the lowest temperature (130 K), most of the clusters contain only a few atoms and are homogeneously distributed on the terraces.

High-resolution STM images reveal that the smallest Au induced protrusions found (figure 6.2 (a)) are located on the bridging oxygen rows. The protrusions have a typical height of ~ 1.7 Å and width of 10 Å, and are assigned to single Au atoms adsorbed in a bridging oxygen vacancy (Supporting evidence for this below).

With increasing deposition temperature, the average cluster density decreases and the average Au cluster size increases accordingly. At 210 K, the clusters are still distributed homogeneously on the terraces but contain on average 10 atoms. Large clusters are not solely located on oxygen rows, and no specific nucleation site can be determined directly from the island geometry. At 300 K (RT) the clusters preferentially nucleate at step edges and contain ~ 30 atoms.

To quantify the interaction of Au clusters with bridging oxygen vacancies, the number of vacancies as well as the number of clusters before and after Au deposition at the different deposition temperatures was counted in high-resolution STM images (figure 6.3).

When Au is deposited, the density of oxygen vacancies decreases at all investigated temperatures. This decrease is clearly not due to a "shadowing" effect from the Au clusters

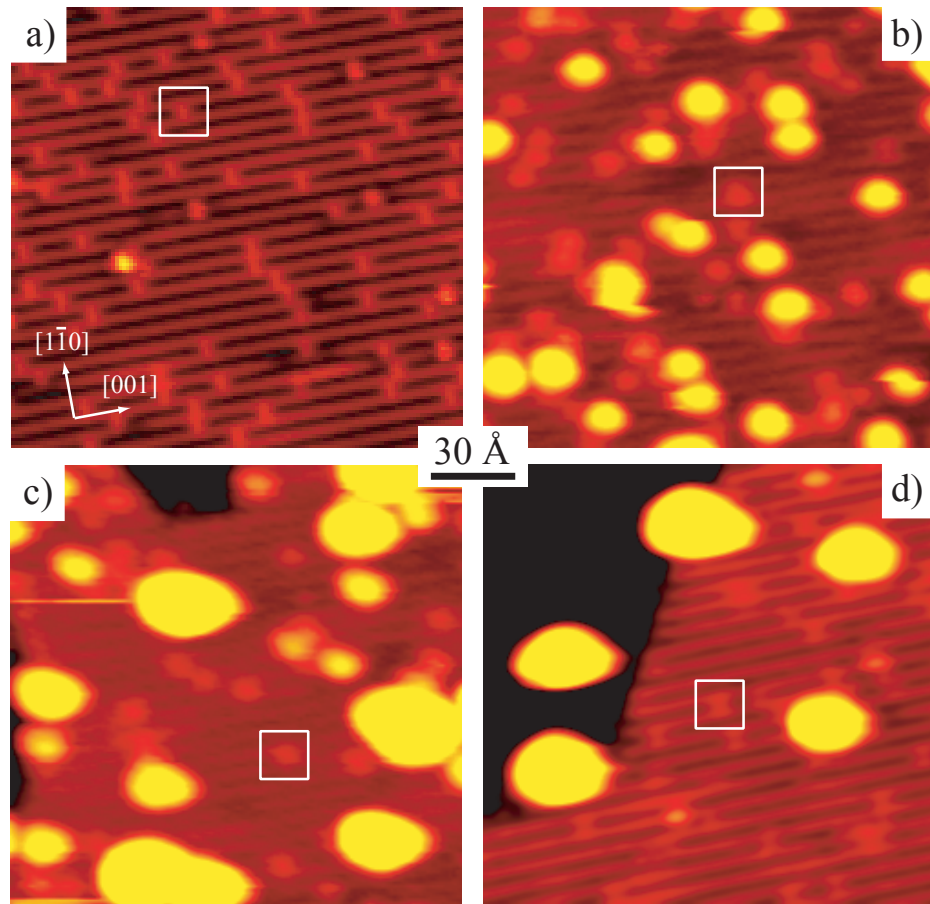


Figure 6.1: (a) Clean TiO₂(110) surface with bridging oxygen vacancies. (b)–(d) TiO₂(110) surface after 4% ML Au deposition at 130 K, 210 K and 300 K, respectively. Vacancies are indicated by squares. All images are 150 × 150 Å²

since they occupy <15 % of the surface area, and thus cannot account for the observed decrease in number of vacancies. At the lowest temperature, close to a 1:1 correlation is observed between the increase in number of Au clusters and the decrease in the number of oxygen vacancies. At higher temperatures, the decrease in the number of oxygen vacancies is considerably larger, indicating that the clusters trap several oxygen vacancies beneath them. Figure 6.3 shows that at all investigated temperatures the clusters bind at oxygen vacancy sites. The experimental findings of figure 6.3 are further quantified and summarized in table 6.1, which lists the number of Au atoms per cluster, the vacancy/cluster ratio and finally the number of Au atoms per vacancy for different sets of deposition temperature and Au coverage. The numbers are averaged over many STM

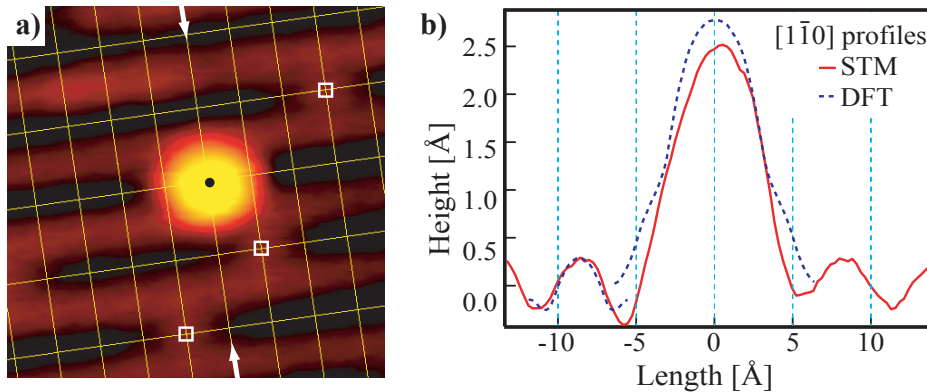


Figure 6.2: (a) A close-up STM image of one of the smallest clusters observed. Note the location on top of the bridging oxygen row. Vacancies are marked with squares. (b) Line profiles comparing experiment and theory (see arrows in (a)).

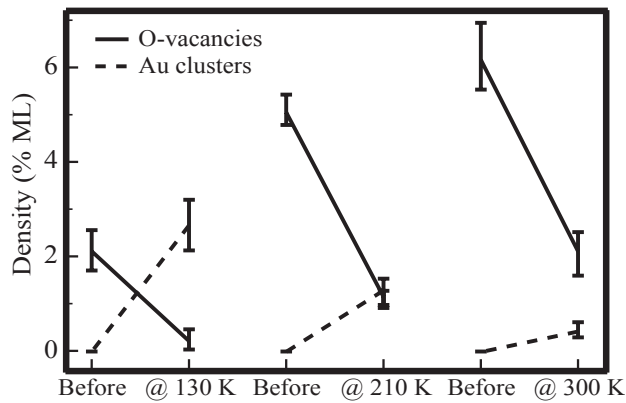


Figure 6.3: Densities of vacancies and Au clusters before and after deposition of ~ 0.04 ML Au at different temperatures. 1 ML = 1 vacancy or cluster/TiO₂(110) unit cell = $5.13 \cdot 10^{14}$ cm⁻².

images. The table clearly shows that the number of oxygen vacancies trapped under each Au cluster increases with deposition temperature for a fixed coverage, but most importantly, that the number of Au atoms per oxygen vacancy is roughly constant and equal to 3-5 in all cases.

An investigation of the increase in the number of "filled" vacancies with Au deposition time at 130 K (figure 6.4) shows that the number of filled vacancies initially increases linearly with deposition time, with a rate which levels off at longer deposition

Coverage	Temp. (K)	Au Atoms/clust.	Vac./clust.	Au Atoms/vac.
0.005	125	1–3	1	1–3
0.005	300	7	2	3
0.02	151	5	1	5
0.04	130	5	1	5
0.04	210	9	3	3
0.04	300	28	9	3

Table 6.1: Average distributions of oxygen vacancies and Au clusters grown at different temperatures and coverages, showing an average of 3-5 atoms per vacancy at all investigated temperatures.

times. This indicates that impinging Au atoms reside on the surface long enough to either find an empty vacancy or when the coverage goes up, to form larger clusters.

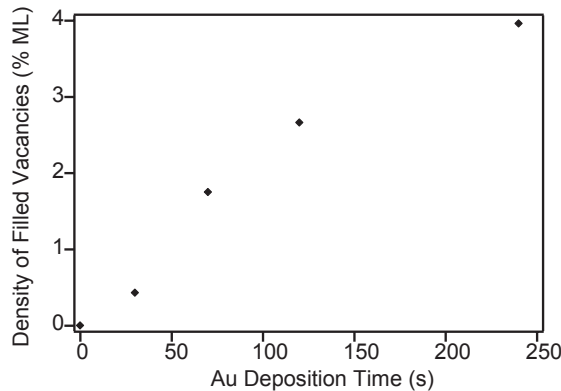


Figure 6.4: The vacancy filling as a function of Au deposition time at 130 K can be seen to level off at longer deposition times.

DFT has been used to determine the binding site of Au on the stoichiometric and reduced surfaces ¹. On the stoichiometric surface, Au is very weakly bound. A single Au atom binds by 1.55 eV in its most favorable site on top a bridging oxygen atom. Adsorption of a full Au monolayer is almost a thermoneutral process [139]. This fact is consistent with the difficulties arising when imaging the Au/TiO₂(110) system by STM as previously stated. The Au-Au interactions thus dominate for larger clusters and makes the

¹Theoretical modelling was performed by Nuria Lopez in Jens Nørskov's group at Denmark's Technical University (DTU). DFT calculations were performed on periodic slabs containing three O-Ti₂O₂-O units (Ti layers) in 2×2 surface super cells, separated by 10 Å of vacuum. Au was adsorbed on one side in line with previous work done on hydroxyls and Au on TiO₂(110) [13,139]. With reference to section 3.5 it can be argued that the number of Ti layers has to be larger than 3, and that the surface super cell should be significantly larger than 2×2 for the calculations to be valid. Extended calculations will hopefully confirm the results below.

Au-TiO₂ adhesion extremely small.

For a single Au atom, the most stable configuration is found to be adsorption in an oxygen vacancy site. This configuration is more stable by 0.45 eV than Au adsorbed on top of a bridging oxygen atom on the stoichiometric surface, and more stable by 0.80 eV than adsorption on top of a five-fold coordinated Ti atom. The Au-vacancy bond is found to be covalent with a very small charge transfer, which is different from Au adsorption in a vacancy on MgO where significant charge transfer occurs [140].

The smallest protrusions observed experimentally are only reproduced in simulated STM images when a single Au atom substitutes the missing bridging oxygen atom (see figure 6.5).

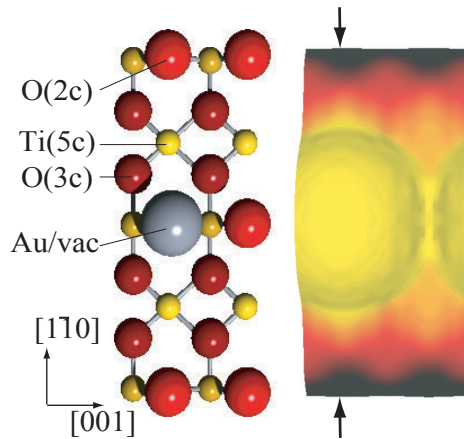


Figure 6.5: Ballmodel and simulated STM image of a single Au atom trapped in an oxygen vacancy. Arrows indicate the line profile shown in figure 6.2 (b).

These findings confirm the interpretation that the smallest protrusions centered on the bridging oxygen rows are single Au atoms trapped at bridging oxygen vacancies. The sample voltage employed is 1.0 V and the simulated images were obtained at a constant density of $3 \cdot 10^{-6} \text{ e}/\text{\AA}^3$, since at this value experimental and theoretical corrugations for the non-defected surface are similar.

6.3 Growth Model

To investigate the mechanism of nucleation and growth of Au clusters, the size distributions of Au clusters grown at different temperatures are plotted in figure 6.6. At low-temperature, the growth results in many small clusters, as also seen in figure 6.1. Upon heating, or depositing Au at RT, fewer but larger clusters are observed, and the cluster size distribution becomes bimodal. The smallest protrusions, i.e. single Au atom-vacancy complexes, can also be observed after deposition up to 300 K, although their relative number decreases with increasing temperatures.

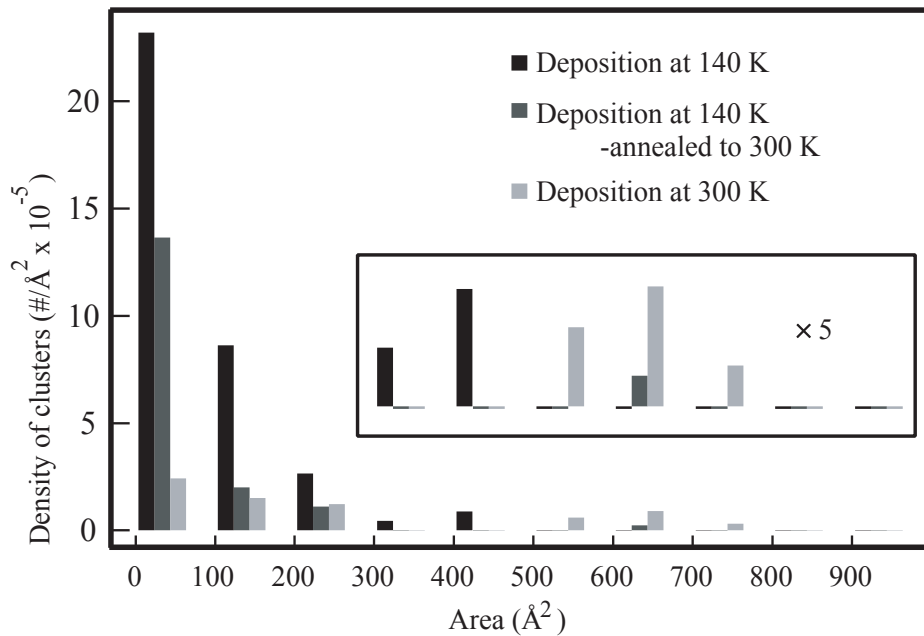


Figure 6.6: Size distributions of Au clusters on TiO₂(110) for different deposition temperatures and annealing after deposition of 0.02 ML Au. All areas were measured at a threshold level of 1 \AA above the medium position of the (110) plane on which the clusters were positioned.

Analysis of sequences of STM images shows no evidence for diffusion of single Au atom-vacancy complexes at any investigated temperature. The bimodal size distribution together with the stability of the smallest clusters is interpreted as a sign of cluster growth through diffusion of clusters above a certain critical size [108].

The critical cluster size for this growth mode can be deduced from the bimodal size distribution at RT in figure 6.6. A minimum in the cluster population starting at 250 \AA^2 indicates that clusters containing 5 to 7 atoms are unstable. Conversely, clusters containing 3 to 5 atoms are stable. This value correlates nicely with the amount of Au atoms found per vacancy (see table 6.1).

Clusters nucleate primarily at oxygen vacancy sites, but upon further growth, a single oxygen vacancy can no longer stabilize the cluster, and the entire cluster-vacancy complex will then diffuse. Whilst diffusing, it can encounter either another cluster (coalesce) or other surface defects. In the former case, a larger cluster is formed that may continue to diffuse as well. If the cluster-vacancy complex encounters other oxygen vacancies, it can bind to them and will therefore stabilize on the surface. Not surprisingly larger clusters formed after growth at, or annealing to, RT are found at step edges, since the step edges typically contain a large number of low coordinated Ti and O atoms that

might act as stable nucleation sites [34].

The bimodal growth model based on cluster instability differs from other models proposed to explain Au growth on TiO₂(110) [141, 142]. Parker *et al.* [142] have shown that the onset of 3D growth corresponds to a coverage of 0.086 ML and 0.15 ML on the stoichiometric and the thermally reduced TiO₂(110) surface respectively (1 ML is defined as the packing density of an Au(111) plane, $1.39 \cdot 10^{15}$ atoms·cm⁻²). Based on the present findings, it can be assumed that the observed 0.064 ML change in transition coverage originates from the presence of oxygen vacancies. A typical vacancy density of 6–7% ML (1 ML is here 1 vacancy/unit cell with $5.13 \cdot 10^{14}$ unit cells·cm⁻²). These numbers are used to calculate that each vacancy binds ~ 3 atoms, the same number as deduced from table 6.1.

For larger clusters, a simple model is used to estimate the number of gold atoms stabilized per vacancy. The stability of a monolayer cluster (represented by a disk attached to a varying number of vacancies) is compared to the stability of a 3D Au cluster on the stoichiometric surface (represented by a sphere).

The energies used in the calculations are as follows: for the disk $E_{\text{disk}} = E_d n_d + \gamma_0 \cdot N \cdot 2 + E_{\text{edge}} \cdot N^{1/2}$ and for the sphere $E_{\text{sphere}} = \gamma_0 \cdot N^{1/3}$. E_d is the Au binding energy to a vacancy (= -2 eV); n_d is the number of vacancies; γ_0 is the surface energy (= 0.3 eV/atom); N is the number of Au atoms; E_{edge} is the edge energy (= 0.6 eV/atom).

This continuum-like model is only a rough estimate and only reasonable for fairly large clusters. The results are summarized in figure 6.7.

If there are no vacancies attached to the Au cluster, the 3D cluster is always the most stable configuration, but if vacancies are included 2D clusters up to a certain size will be more stable than the 3D (freely moving) clusters. The maximum number of Au atoms stabilized by a group of vacancies is given by the intersection of the curves representing the two configurations. With a large number of vacancies under the cluster, such as 5 or 10 (see vertical projections in figure 6.7), the maximum number of Au atoms per vacancy that can be stabilized and adsorbed in a disk-like structure is about 3. This correlates very well with the experimental observations in table 6.1.

6.4 Conclusion

The present study has shown that bridging oxygen vacancies are the nucleation sites for Au clusters on the rutile TiO₂(110) surface at all investigated temperatures. A single Au atom-vacancy complex is stable up to room temperature. An oxygen vacancy binds on average 3 Au atoms, which means that for larger clusters the Au-substrate interface contains a high density of oxygen vacancies. This enhances the binding of Au particles to the substrate.

A new growth model involving coalescence of diffusing Au-vacancy complexes explain previous and present observations of the Au/TiO₂(110) system.

The presence of a high concentration of oxygen vacancies underneath the Au clusters will inevitably lead to a profound change in the electronic configuration of both the clusters and the substrate. This change in electronic configuration could very well explain, on one hand, why Au nano-particles are catalytically active for low-temperature

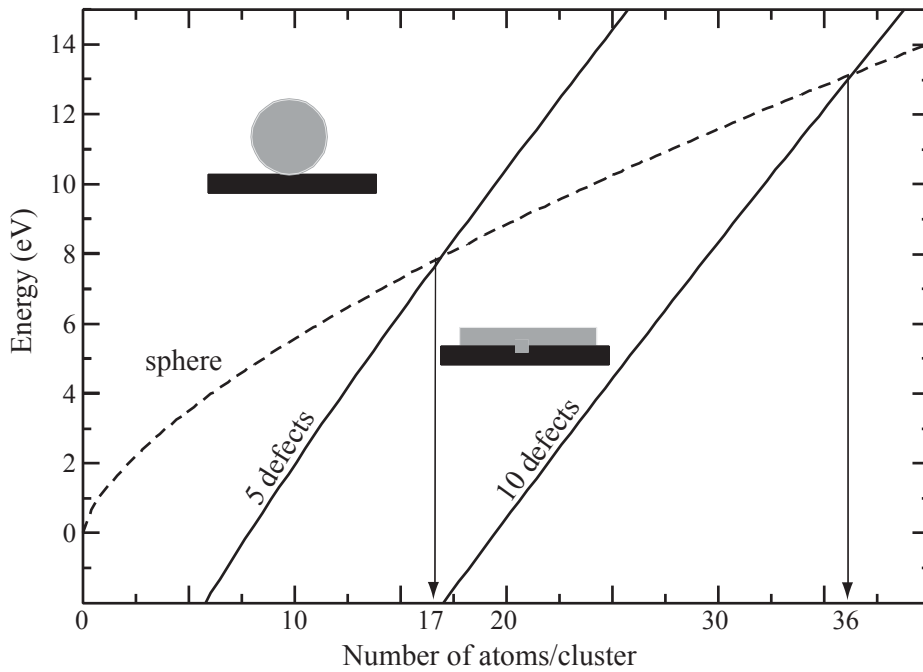


Figure 6.7: Transition between adsorption on vacancies and diffusion. Solid lines represent the energy for the Au disk adsorbed on a given number of oxygen vacancies (indicated in the graph). The dashed line shows the limit for diffusion, and the vertical arrows indicate the actual number of Au atoms in the cluster at which the transition occurs.

CO oxidation on the TiO₂(110) surface or, on the other hand, it could explain why the TiO₂(110) surface itself becomes catalytically active when Au clusters are present on the surface. The latter process will be discussed in further detail in chapter 7.

CHAPTER 7

Thermal Activation of O₂ Molecules on TiO₂(110)

Recent experiments have shown that oxygen molecules on the TiO₂(110) surface only diffuse when they are thermally activated by electrons from the conduction band. Bridging oxygen vacancies are shown to induce a band bending of the conduction band, increasing the diffusion activity of oxygen molecules. Two models for the diffusion are proposed and a mechanism for the dissociation of oxygen molecules in oxygen vacancies found in chapter 4 is discussed further in the context of thermal activation.

This chapter is based on paper IV.

7.1 Introduction

In this chapter, it will be shown that the diffusion of oxygen molecules on the TiO₂(110) surface is not a standard diffusion mechanism, and that the hopping rate of the diffusing species correlates well with the density of electrons in the conduction band. A model is proposed, where the oxygen molecules only diffuse, when they are charged by electrons in the conduction band.

Oxygen vacancies and metal interstitials are thermally created in stoichiometric reducible metal oxides like TiO₂ (see section 3.2). These defects act as donors and acceptors of electrons and affect both the optical, chemical and electrical behavior of metal oxides [1, 68].

In TiO₂, the chemical potential (Fermi energy) is determined by the bulk Ti interstitials and oxygen vacancies, but the lack of Ti interstitials at the surface and the local change in the density of vacancies causes a band bending which affects the activity of adsorbed oxygen molecules.

7.2 Diffusion Characteristics

In chapter 4, oxygen molecules after adsorption on rutile TiO₂(110) were shown to reside on top of the Ti atoms in the troughs along the [001] direction between the bridging oxygen rows. Through the use of variable temperature, high-speed scanning tunneling microscopy, the motion of single oxygen molecules at the TiO₂(110) surface can be followed.

The displacement distributions obtained are analyzed according to the method used in the work by Ehrlich *et al.* [143], where focus is on the probability of finding the oxygen molecule at the same site in two consecutive STM images, P_0 .

If $ht \ll 1$, where h is the hopping rate and t the time between images, then P_0 can be approximated as:

$$P_0 \approx e^{-ht}, \quad (7.1)$$

but when the molecules perform several jumps in between images, this approximation is not valid and a modification is needed. The modification accounts for jumps where the molecule jumped between images, but either returned to the original position or performed sequential single jumps that appear as longer jumps.

The displacement distribution is then given as:

$$^1P_x = e^{-h_1 t} I_x(h_1 t), \quad (7.2)$$

where $I_x(h_1 t)$ is the modified Bessel function of the first kind of order x , where x is the distance from the origin ($x = 0$) at time t . When using equation 7.2 it is found that the displacement distributions are very well described assuming only single jumps of the oxygen molecules along the [001] direction (figure 7.1).

By analyzing the displacement distributions of oxygen molecules in the temperature range 120 K to 250 K, the hopping rate at different temperatures is extracted. From

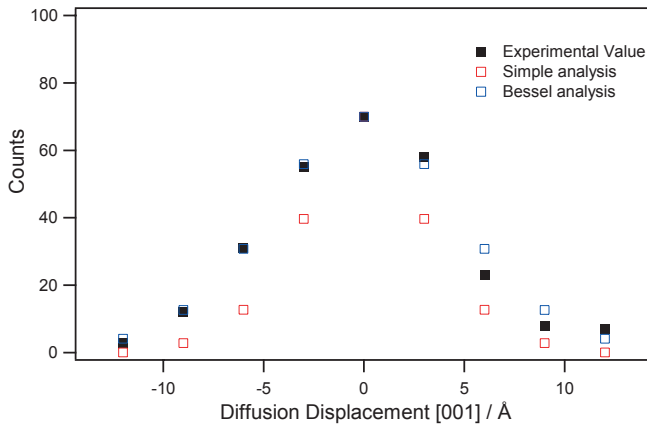


Figure 7.1: *Displacement distribution (Number of jumps between consecutive STM images) compared to both a simple exponential function and the single jump Bessel function (from eq. 7.2) with the same P_0 . The Bessel analysis gives a significantly better correspondence with data.*

this it is possible to explore the activation energy for the diffusion process through an Arrhenius plot (see figure 7.2) since the hopping rate h for barrier limited diffusion is:

$$h = h_0 \cdot \exp\left(\frac{-E_a}{k_B T}\right), \quad (7.3)$$

where E_a is the activation energy (diffusion barrier), k_B Boltzmanns constant, h_0 the attempt frequency and T the temperature. However, this reveals three anomalies (see figure 7.2):

- The activation energy changes in different temperature regimes.
- The attempt frequencies extracted in this manner ($h_0 \sim 100 - 10^6$) are far below what is expected from any realistic potential ($h_0 \sim 10^{12}$).
- Samples with different history (reduction level, exposure etc.) give drastically different oxygen diffusion rates.

7.3 Thermal Activation

We propose a model where an uncharged oxygen molecule adsorbed on the Ti rows is charged by electrons from the conduction band. This charging enables the diffusion of the molecule. According to this model, the hopping rate is proportional to the density of electrons in the conduction band at the surface. This yields a diffusion which is

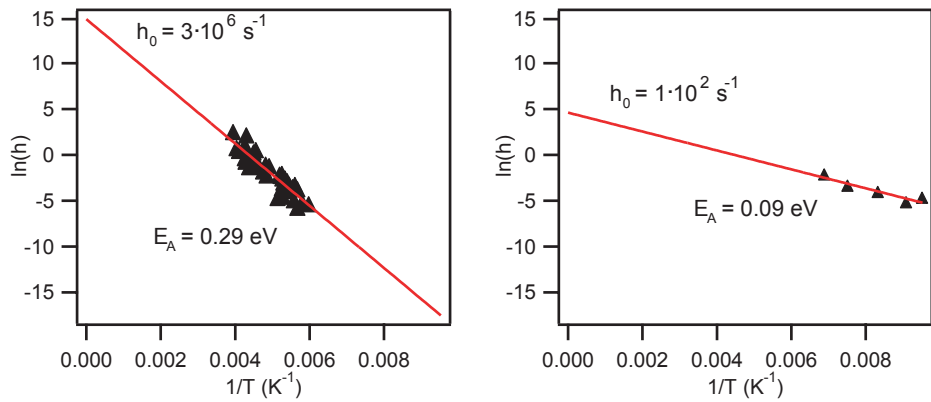


Figure 7.2: Hopping rates measured for two different samples in the temperature regimes (a) 180 K-250 K and (b) 120 K-145 K. Fits to the standard Arrhenius equation (7.3) indicate the differences in both attempt frequency and activation energy in the two regimes.

exponentially dependent on temperature, with different apparent activation energies for different temperature intervals depending on the main contributor (dopant) of electrons to the conduction band. It also explains the difference between the different activities on different samples, since the nature and number of dopants is dependent on the history of the sample (reduction level, exposure to H etc.).

The density of conduction band electrons in an n-type semi-conductor (like TiO₂) depends on the different donor levels relative to the conduction band and the temperature [48, 71]. At low temperature the highest lying donor state is the only donor of electrons to the conduction band ¹. This pins the chemical potential, μ , (or Fermi level) midway between the highest lying donor state and the conduction band (see figure 7.3). The density of conduction electrons, n_c , in a semi-conductor is [71]:

$$n_c = N_c(T) \cdot \exp\left(\frac{-(E_c + E_b - \mu)}{k_B T}\right), \quad (7.4)$$

where E_c is the energy of the lowest conduction level, E_b is the band bending energy (discussed below). $N_c(T)$, which is the effective density of electron states in the conduction band, is normally proportional to $T^{3/2}$ [71]:

$$N_c(T) = 2(2\pi m_{eff} k T / h^2)^{3/2} \quad (7.5)$$

For TiO₂, $N_c(T)$ is of the order 10^{17} , using the effective electron mass $m_{eff} = 20m_e$ [12].

As the temperature increases, all the donor states are ionized and a saturation regime is reached, where the density of conduction band electrons do not increase. In this

¹Due to the low temperature, the electrons are *frozen out* in the highest lying donor state, which acts like the valence band in an intrinsic (clean) semi-conductor.

regime, the chemical potential changes to a position midway between the conduction band and the valence band. When $k_B T$ is high enough to bring electrons from the lower lying states up to the conduction band the chemical potential is fixed again and the density of conduction electrons increase. Equation 7.4 still holds for the fully ionized donor states, but now the chemical potential is in the middle of the bandgap.

For this study it is important to realize that the semi-conductor can have several donor states. If these states are separated by more than $k_B T$, the chemical potential will ideally successively become fixed midway between each of the donor states and the conduction band as the temperature is increased. Visualized in an Arrhenius type graph, figure 7.3 illustrates how the increased energy gap between chemical potential and conduction band as the temperature increases gives the graph a steeper slope.

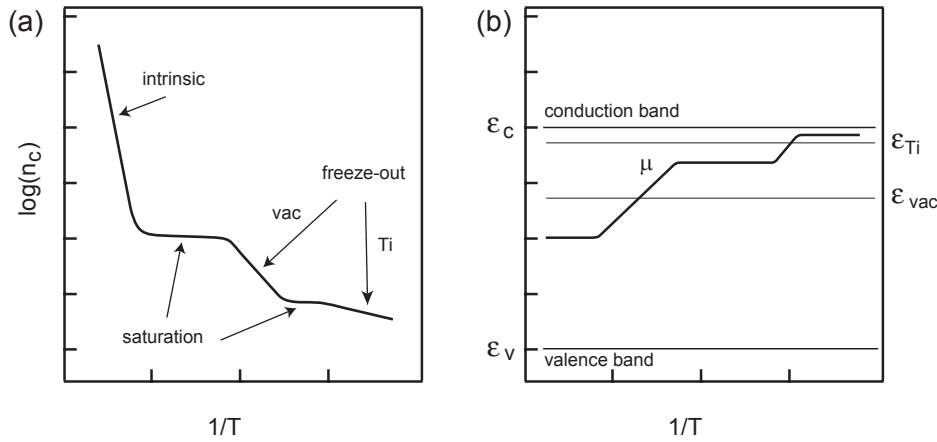


Figure 7.3: Schematic illustration of the temperature dependence of the density of conduction band electrons in an extrinsic n-type semi-conductor. (a) Conduction electron density with different gradients in the freeze-out regimes with (from low T) Ti donors and vacancy donors, in the saturation regimes with constant carrier density, and finally in the intrinsic regime. (b) Chemical potential showing the fixed energy in the respective regimes and the decrease in the saturation regimes.

The density of conduction band electrons in bulk reduced TiO_2 are determined, at different temperatures, by donor states from Ti interstitials very close to the conduction band and by donor states from oxygen vacancies in bulk and surface.

Assuming that the hopping rate, h , is proportional to the density of electrons in the conduction band, n_c , gives good agreement with the data, as can be seen in figure 7.4 (a), where equation 7.4 was fitted to the experimental data with $(E_c + E_b - \mu)$ and $(CT^{3/2})$ as the fitting parameters, where C expresses the proportionality between h and n_c .

The activation energies $(E_c + E_b - \mu)$ extracted from the fits are 0.392 eV, 0.374 eV and 0.366 eV for the <8%, 8%-20% and 24% cases respectively. The standard error (± 0.02) is given for the best fit, which determines the constant C used in the other fits.

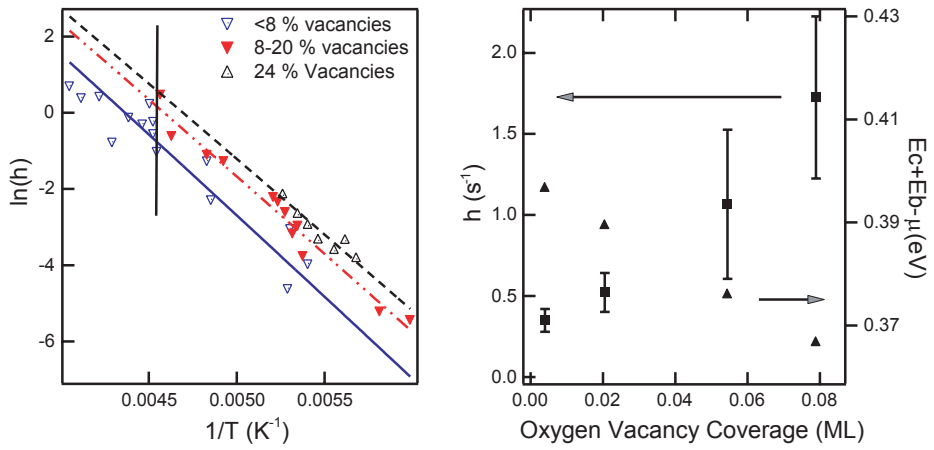


Figure 7.4: (a) Hopping rate of the molecules as function of temperature, the three lines are proportional to the number of conduction electrons in the bulk (equation 7.4), assuming a fixed N_c for all three cases.(b) Hopping rates obtained on one sample (same bulk reduction level) prepared with different densities of vacancies at a fixed temperature (220 K, corresponding to the vertical line at $4.55 \cdot 10^{-3}$ in (a)). Also presented is the extracted activation energy (from equation 2) which decays roughly linearly with the number of oxygen vacancies.

The bulk oxygen vacancy levels have a fixed energy $E_v = 0.76$ eV below the conduction band, which if it was the only dopant level would pin the chemical potential ~ 0.38 eV below E_c [68]. The extracted activation energies fit very well with this experimentally determined distance between the chemical potential and the conduction band. At the temperatures investigated (180 K – 250 K) n_c thus appear to be determined by the oxygen vacancy levels and the band bending discussed below.

With the chemical potential found, it is concluded that the Ti interstitial states ($E_1 = 0.002$ eV, $E_2 = 0.02$ eV and $E_3 = 0.05$ eV below E_c) are (almost) completely ionized in the temperature interval investigated. $k_B T$ (=0.016-0.022 eV). is less than E_3 , so one would expect some degree of freeze-out in this state, but the amount of Ti donors is smaller than the density of bulk vacancies , which apparently gives a higher density of holes in the bulk vacancy levels than the density of electron in the Ti states, which then causes the electrons to fall into the vacancy levels [72]. An upward surface band bending would also contribute to emptying the higher lying states (discussed below).

The activity of the oxygen molecules has been investigated in the temperature regime below 180 K. Only very few experiments/samples yield good results in this regime with hopping rates either too small to give significance in the data (< 0.002 jumps/s) or too high activity (> 5 jumps/s). The latter case of course also affects the higher temperature regimes. The activity is strongly dependent on sample history. An example of the hopping rate measurements between 120 K to 180 K can be found in figure 7.2 (b), where it

is clear that the hopping rate is higher than in figure 7.2 (a), because of the higher degree of reduction of the sample in (b).

The band bending on the $\text{TiO}_2(110)$ surface, which depends on the charge accumulation/depletion at the surface relative to the bulk reduction, is determined by the density of bridging oxygen vacancies and the lack of Ti interstitials near the surface as well as adsorbates. This affects the density of conduction electrons near the surface (see equation 7.4). The effect of the band bending, E_b , is illustrated in figure 7.5.

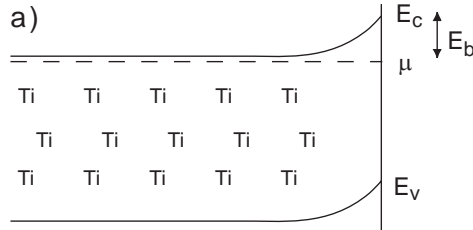


Figure 7.5: (a) Schematic drawing of the energy levels at the titanium dioxide surface. In the bulk the conduction band level is determined by the Ti interstitials and oxygen vacancies, while at the surface an upwards band bending E_C is found caused by the lack of interstitials and a higher density of bridging oxygen vacancies.

The variation of the band bending as a function of oxygen vacancy densities at a fixed temperature is investigated to verify the hopping rate dependence on the conduction band placement. The same sample with the same bulk reduction level was used for this series of experiments to ensure that the bulk reduction level did not change significantly between measurements. Oxygen vacancies act as donor states, effectively causing a downward band bending ($\Delta E_b \propto -\Delta n_{vac}$), thus increasing the diffusion activity on the surface [12, 67, 101, 144]. That is, the diffusion activity of the oxygen molecules increases with the number of oxygen vacancies. Figure 7.4 (a) indicates that the conduction band electron density differs with three different surface vacancy densities.

The proposed model is, as mentioned in the introduction of the chapter, based on the existence of a transient charged oxygen state. Such states are known to exist, and have been studied extensively on powdered titanium oxide samples [145]. Infrared adsorption measurements with and without oxygen present indicate that the whole mechanism (electron capture and release) spans 10-100 μs , while the transfer mechanism has a time span of about 0.5 μs far below the time resolution of our STM [145].

7.4 Diffusion Mechanism

Two diffusion mechanisms are immediately imaginable.

First, the diffusion of the charged molecule could be a standard diffusion with Arrhenius behavior (equation 7.3), a low diffusion barrier and an attempt frequency of order 10^{12} , but only activated when the molecule is charged yielding a lower apparent h_0 .

Second, the charged molecule could have an equilibrium position in a bridge site between two equilibrium positions (Ti top sites) of the uncharged state. Upon discharging either to the valence band or to other lower lying states, the molecule will again be stable on top of a Ti atom. The molecule can either return to its old position (no net movement) or move on to the next Ti atom resulting in a movement of one unit cell. The process is illustrated in figure 7.6.

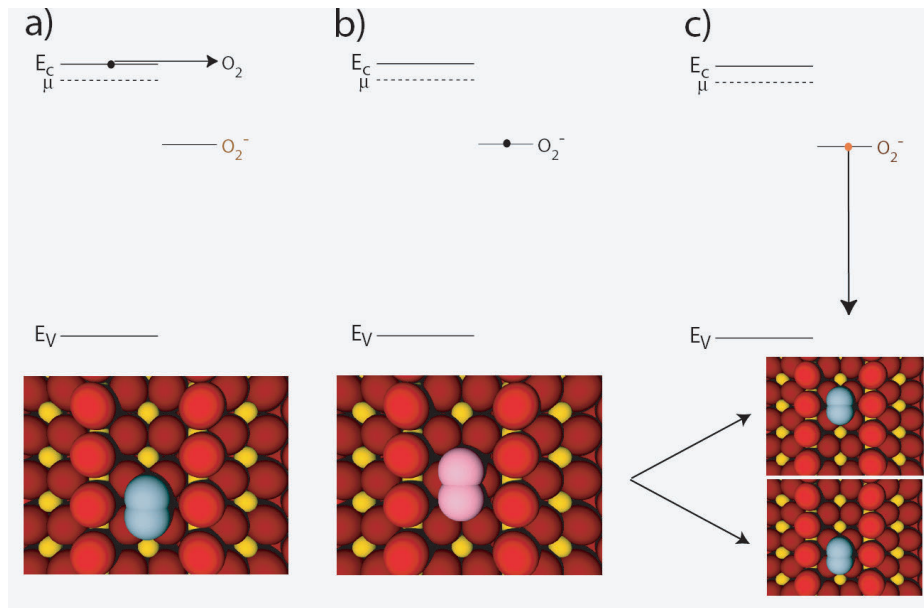


Figure 7.6: *Schematic model of the diffusion process a, In the first step the oxygen molecule are thermally charged by an electron in the conduction band while it resides on top of a Ti atom. b, upon charging the molecule change equilibrium position to a bridging site between two Ti atoms. c, when discharging electrons to the valence band or impurity levels, the molecule again change its equilibrium position, either through resuming the old position or by moving half unit cell further away.*

At the time of writing, the exact diffusion mechanism is undetermined. Theoretical investigations are under way to predict which model is correct.

7.5 Dissociation in Vacancies

As mentioned in chapter 4, an intermediate state is found to dissociate in a bridging oxygen vacancy leaving an oxygen atom on the adjacent Ti row. In our earlier investigation this intermediate was attributed to a precursor state [118], but the current observations of the diffusion of charged molecular oxygen allows for a more detailed view on this mechanism.

We propose that the charged oxygen molecule enters an equilibrium position in the vacancy. Upon de-charging, the oxygen molecule in the vacancy dissociates to fill the vacancy with one of the oxygen atoms, and the other oxygen atom moves to the adjacent Ti row.

7.6 Conclusion

The diffusion of oxygen molecules was shown to be limited by the thermal activation of the molecule through the hopping rates of oxygen molecules. The introduction of more donor levels (a higher density of vacancies) leads to a local band bending of the conduction band which gives rise to a higher activity of the oxygen molecules.

Two possible models for the diffusion of the oxygen molecules were presented. One is the standard diffusion of the charged molecule limited by the density of conduction band electrons, while the other is based on an equilibrium position change for the charged molecule, which leads to diffusion upon de-charging.

A possible process for diffusion into and dissociation in a bridging oxygen vacancy was discussed based on the diffusion models.

The fact that the activity of an oxygen molecule can be changed with the very light "doping" of bridging oxygen vacancies and is extremely dependent on the level of bulk reduction is very interesting from both a catalytic and photocatalytic point of view. The charged oxygen molecule could very well be an active species in the various catalytic processes occurring on the TiO_2 surfaces.

The photocatalytic properties of commercial TiO_2 are suppressed by doping with Al^{3+} , which is an acceptor atom [62]. In the present context this can be explained by the decrease in the chemical potential causing the surface to become completely inactive.

Au, on the other hand, causes a downward band bending, which in turn cause an increased activity of the surface. This might be used to explain the catalytic activity of the Au/ TiO_2 system [3, 16]. H_2O also induces donor levels [12], and the presence of water in the industrial catalyst has been shown to increase the activity of the catalyst [4, 101]

CHAPTER 8

Vanadium Oxide Nanoclusters on Au(111)

This chapter is based on a preliminary study of vanadium oxide nanocrystals on the Au(111) surface. Vanadium clusters are grown in a background pressure of oxygen and post-annealed in UHV to produce vanadium oxide nanocrystals. Characterization with STM shows two different crystal structures; a quadratic and a hexagonal phase. These are described and discussed in terms of previous investigations of vanadium oxide on Pd(111).

8.1 Motivation

V_2O_5 supported on anatase TiO_2 is one of the most widely used catalyst for the reduction of nitrous oxides (NO_x) emitted from combustion engines or power plants. The catalyst has a very high reactivity in the so-called selective catalytic reduction (SCR) De NO_x process and is resistant to SO_2 poisoning. [146].

NO_x is produced in all combustion processes, and since the gases are greenhouse gases and cause lung-related problems, the regulating laws concerning emission of these gases are tightening. The SCR De NO_x process removes NO_x using ammonia as the reducing agent through the process:



which yields harmless nitrogen and water.

The active phase of vanadium oxide is slightly reduced V_2O_5 [113, 146]. A surface reduction to create V species with valences of 4+ or lower is necessary in order for the V_2O_5 surface to catalyze chemical reactions. Industrial type catalysts are often prepared from V_2O_5 and then easily reduced under reaction conditions to initiate chemical and catalytic reactivity.

To study the very basic catalytic behavior of a catalytically active species, it can be practical to break the complex system down into model systems and study individual processes to be able to grasp the complexity of the entire system. Working with STM, model systems consist of atomically flat surfaces either of the catalytically active phase itself or of another surface with the active phase on or embedded in the surface [53]. Ideally one would like to study V_2O_5 nano crystallites on the surface of anatase TiO_2 to mimic the real catalyst, where recent investigations have shown that the support plays an active part in the dispersion of the vanadium oxide [146]. As illustrated in the previous chapters of this thesis, even the most studied surface of the titania surfaces ($TiO_2(110)$) is not only difficult to work with, it also still features a large number of unknowns. The anatase $TiO_2(101)$ surface has been characterized by STM [34, 147], but the lack of understanding of the anatase surfaces makes it an unsuitable choice for studying the active V_2O_5 nanocrystals. The $TiO_2(110)$ surface has attracted much attention as a model system for the vanadia/titania system. Investigations include such surface analysis techniques as XPS [148–153], STM [148, 154], AES [152], NEXAFS [148], ARPEFS [155], LEED [152], HREELS [152], SRPES [156] and XPD [150, 157]. All but the most recent [153] of these investigations have deposited metallic V onto the surface and subsequently oxidized the surface. V initially reduces the surface to form $V^{2+/3+/4+}$ and Ti^{3+} ions, and in no cases are V^{5+} ions found, indicating that the desired level of oxidation has not been reached. Wong et al. [153] deposited V in an oxygen background pressure of $1 \cdot 10^{-3}$ Torr, producing V^{5+} ions on the surface.

STM studies on the growth of vanadium on the $TiO_2(110)$ (1×1) surface reveal that V binds preferentially at the Ti^{4+} cations sites. Initial growth oxidizes the V atoms while reducing the Ti^{4+} cations, causing strong local changes of the electronic and physical properties of the surface [148].

With the strong interaction between the TiO₂(110) surface and the adsorbates, it can be desirable to create an even simpler model system, where the surface-metal oxide interactions are less pronounced. The Netzer group has recently made significant contributions to the understanding of the vanadium oxide adlayer structure with their focus on the V_xO_y/Pd(111) system. Metallic V is deposited in a background pressure of oxygen on Pd(111) to create vanadium oxide overlayers that were studied with STM, LEED, XPS, NEXAFS, HREELS, XPD [158–162] and DFT calculations [163]. The investigations have revealed a number of vanadium oxide surface phases that differ in structure from the various bulk structures. The most important structures found are (1) the metastable s-V₂O₃ (2×2) structure, (2) the VO₂-hex structure, and (3) the VO₂-rect structure. These structures will be discussed in some detail at a later point for comparison with the present results. The V_xO_y/Pd(111) system has some inherent negative points. The Pd(111) surface is not chemically inert to the extent where surface-adsorbate interactions can be excluded, and a number of alternative surface science techniques needs to be applied to ensure that the overlayers of V_xO_y are pure and Pd free. Also the surface does not have other nucleation sites (or pinning points) than at steps. This causes all clusters to be bound to the most reactive areas of the surface, inducing interaction problems in the case of small crystals.

A single-crystalline Au(111) surface, however, holds advantages both because it is chemically rather inert [164], and because the surface disperses the active catalyst material. Au(111) was previously used in investigations into NiO [165, 166] and CoO [167] overayers on Au(111), but Ni and Co were deposited in amounts corresponding to 1-3 ML, which means that the dispersion properties of the substrate were not exploited.

The present group has previously performed extensive work on another catalyst model system, the MoS₂ hydrodesulfurization system, which was studied with STM in the form of nanocrystals on the Au(111) surface [168–171]. The model system was synthesized by depositing Mo onto the reconstructed Au(111) surface in an H₂S ambient and post-annealed to create triangular MoS₂ nanocrystals widely dispersed on the surface. The elegant feature of this system is the "herringbone" reconstructed Au(111) surface, which facilitates a dispersion of the adsorbed material.

The experience with the MoS₂/Au(111) system and the lack of information about the intrinsic properties of vanadium oxide nanocrystals spurred the group to conduct preliminary investigations of the V_xO_y/Au(111) system to obtain information about the molecular structure of the nanocrystals.

The present chapter establishes proof of concept and describes the initial observations. Further investigations are needed to make qualitative statements about the system, but a number of interesting points can be made from these preliminary investigations.

8.2 The Model Substrate

Gold belongs to the class of metals, whose surface reconstructs in the clean state [172, 173]. Au(111) reconstructs into the characteristic "herringbone" reconstruction [174], which provides an ideal, regular array of nucleation sites for epitaxial growth of highly dispersed metal islands [175]. The reconstruction is characterized by a (22 × √3) unit

cell in which the gold atoms in the topmost surface layer are compressed gradually by $\sim 4.5\%$ along the $[1\bar{1}0]$ direction. Due to this contraction, 23 surface gold atoms are distributed among 22 bulk sites in the unit cell, resulting in alternating fcc and hcp stacking regions which run parallel along the $[11\bar{2}]$ direction. Brighter dislocation lines of Au atoms located near bridge positions are separating the fcc and hcp areas, as shown in figure 8.1(b). Long-range elastic interactions introduces domain boundaries, approxi-

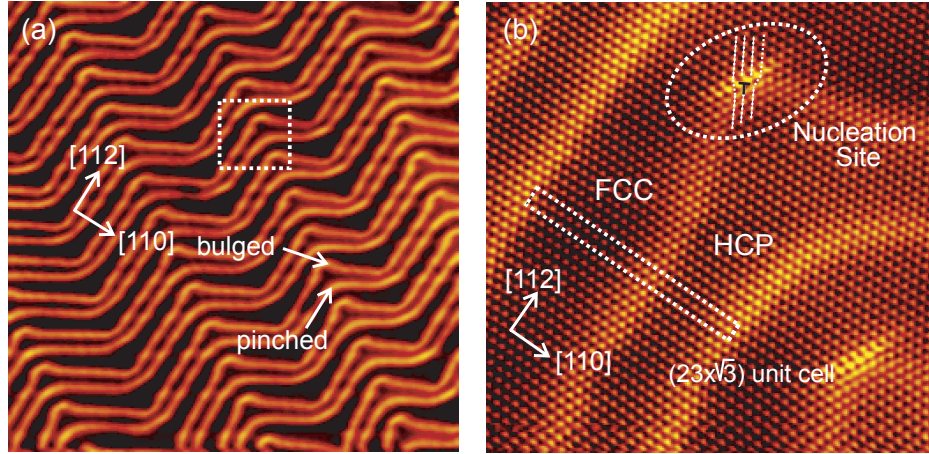


Figure 8.1: STM images of the Au(111) surface. (a) A large-scale STM image of the Au(111) “herringbone” surface reconstruction ($802 \times 795 \text{ \AA}^2$). The bulged and the pinched elbow sites are indicated together with the directions of the crystal. (b) The surface imaged with atomic-resolution ($141 \times 135 \text{ \AA}^2$, $V=-39.1 \text{ mV}$, $I=1.55 \text{ nA}$). The surface unit cell is indicated with a rectangle. The bright lines reflect Au atoms in bridge sites in the transition region between fcc and hcp sites and have a corrugation of $\approx 0.2 \text{ \AA}$. The bulged elbows (white circle) are associated with a surface dislocation (indicated with a \top).

mately every 140 \AA [176]. At these boundary lines, the domains bend by alternating $\pm 120^\circ$, and a zig-zag pattern often referred to as the “herringbone” reconstruction forms. Two types of elbows are observed, a pinched and a bulged elbow. The latter, which is associated with a surface dislocation, acts as the preferential nucleation site in the epitaxial growth of a number of different metals and as the pinning site of molecules [177–179]. The surface thus provides a periodic network of nucleation sites.

In this study, the herringbone reconstruction is used as a template to disperse oxidized V into nanoclusters of similar size and with a well-defined nanometer separation. Figure 8.2 shows STM images of V deposited at a submonolayer coverage onto the Au(111) surface. Indeed, V is observed to belong to the category of metals that nucleates in a regular fashion at the herringbone elbows. The deposited V is seen to self-organize in equally sized $\sim 50 \text{ \AA}$ wide nanoclusters dispersed onto the entire surface. For the subsequent synthesis of vanadium oxide nanoclusters, the high degree of

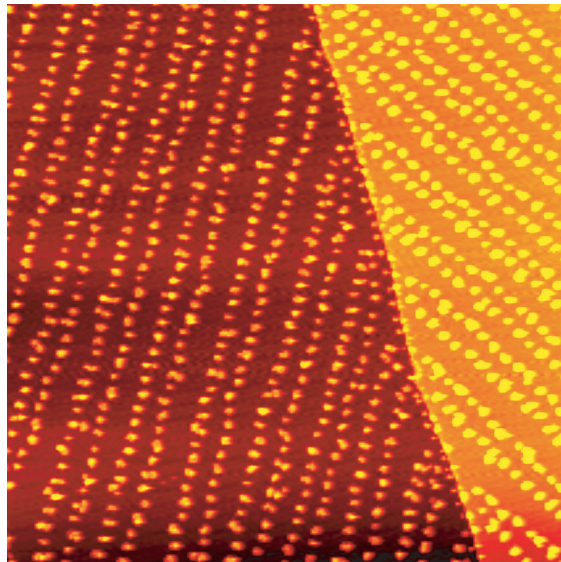


Figure 8.2: STM image ($2500 \times 2500 \text{ \AA}^2$) of V deposited on the Au(111) surface at room temperature in UHV.

dispersion and narrow particle size-distribution constitute a favorable situation since it enables direct access of gaseous O₂ and ensures a homogeneous oxidation of the clusters during crystallization.

The actual mechanism by which metals nucleate in the herringbone elbows has been investigated previously. Only a selected range of metals have been observed to nucleate in the manner demonstrated above, here including Ni, Co, Fe, Ru, Pd, Mo and now also V [175, 177, 178, 180–184], whereas other metals like Cu, Ag, Al and Au do not [185, 186]. A closer look at the actual nucleation site in the herringbone elbow is demonstrated in the atomically resolved STM image of the clean Au(111) in figure 8.1(b). The predominant feature is the dislocation (indicated with a T in figure 8.1 (b)) in which one Au atom has a reduced (five) and another atom an increased (seven) in-plane coordination. Whereas the brighter lines which characterize the herringbone pattern are predominantly ascribed to a geometrical shift in the surface corrugation, clearly the electronic effects also play a role at the dislocation site. The altered electronic structure localized around the surface dislocation may be prone to interact with the severely under-coordinated ad-atoms. Specifically, it is believed that a few, highly strained gold atoms near the dislocation are kicked out in an exchange process with ad-atoms. This theory is supported by predictions that vanadium will alloy in the surface and eventually dissolve into the bulk of Au [187]. The same is true for Mo and Ru which both nucleate preferentially in the herringbone elbows [187]. The exchanged atom(s) may thus form a nucleation site enabling the growth of clusters. Experiments have shown that V diffuses irreversibly into the bulk of Au(111) at 450 K, but that exposure to oxygen will stabilize

the vanadium oxide species on the surface to temperatures above 800 K [188].

8.3 Experimental Details

Prior to the experiments, a Au(111) single crystal is prepared as the model substrate. The integrity of the Au(111) “herringbone” reconstruction (Section 8.2 and figure 8.1) is quite sensitive towards impurities, and contaminations present in the surface are usually revealed in STM images as disruptions of the periodic pattern of the reconstruction [189]. The Au sample is cleaned by cycles of Ar⁺ ion sputtering (1.5 kV) and annealing (900 K, 10 minutes). This procedure generates a clean surface and a regular herringbone pattern of the Au(111) single crystal as determined by AES and STM.

An e-beam evaporator (Oxford Applied Research) was used for the deposition of vanadium. The evaporator holds 2 mm vanadium rods, and is capable of evaporating metals at coverages less than a monolayer in a controlled and reproducible manner.

For the oxidation of V, O₂ is dosed through a leak valve into the chamber. A background pressure of 5.0×10^{-7} torr was used before, during and after V deposition for a total of 10 minutes, corresponding to 300 L (1 L (langmuir) = 1×10^{-6} torr·sec). The high pressure of oxygen ensures a high rate of oxygen molecules impacting the surface while depositing V onto the surface, in the attempt to fully oxidize the impinging V atoms.

8.4 Preparation of V_xO_y Nanoclusters on Au(111)

When V is initially deposited in UHV, and subsequently exposed to a background pressure of 5×10^{-7} torr oxygen at 400K for 10 min, the vanadium oxide clusters still form preferentially in the herringbone elbows (Fig. 8.3 (a)). The rough structure seen with STM however suggests that the clusters are in an amorphous state of oxidized V.

When the V is deposited in an ambient of 5×10^{-7} torr oxygen at RT, as can be seen in figure 8.3 (b), the amorphous clusters appear to be more oxidized and are still widely dispersed on the surface, but the herringbone surface reconstruction is no longer visible. At the same time the amount of adsorbed material appears to have gone down, which could indicate that some V has alloyed into the surface layer disturbing the long-range interactions that are responsible for the herringbone superstructure.

Neither procedure produces crystalline vanadium oxide clusters, but since oxidation stabilizes the vanadium species at the surface up to 800 K [188], we chose to anneal the system in oxygen.

The present preparation method contains the following steps: V is initially deposited for 1 min while the surface, held at temperatures from RT to 523 K, is exposed to a background pressure of 5×10^{-7} torr oxygen. The background pressure of oxygen is maintained for 2-6 min. The sample is subsequently annealed to 623 K for 3-10 minutes. The V coverage is of the order 20 percent (0.2 ML), as estimated from images of V deposited in UHV (figure 8.2). This estimate does not account for multilayer growth, so the result is underestimated, since some degree of 3-dimensional growth is observed

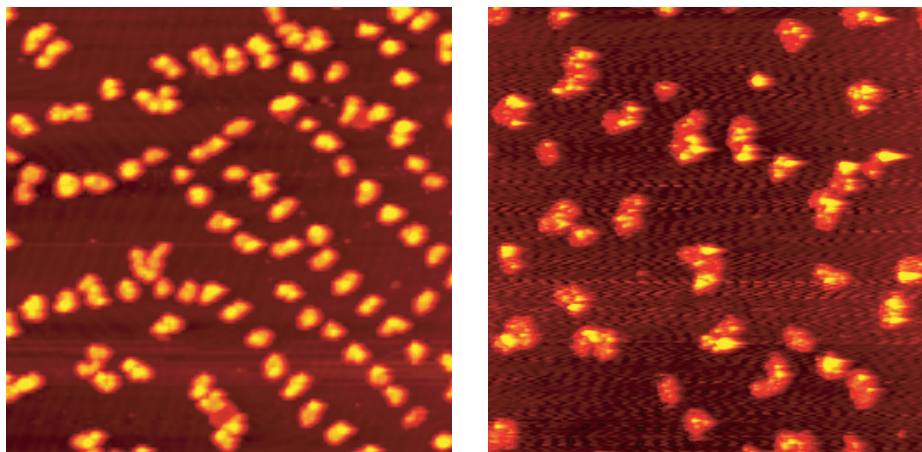


Figure 8.3: STM images of vanadium nanoclusters on the Au(111) surface at different stages of oxidation. (a) Deposition of V in UHV at RT was followed by oxidation at 400 K for 15 min. (b) V deposition performed in a background of O₂ at RT creates a higher degree of disorder on the surface. In both cases the O₂ background pressure was 5×10^{-7} torr. The size is 1000 × 1000 Å².

even for the smallest clusters. The current preparation procedure ensures crystallization of some of the oxidized vanadium clusters (See figure 8.4). After the crystallization, the sample cools to RT before STM is performed.

A *final* preparation method that optimizes the number of ordered clusters has still not been found, but as can be seen in figure 8.4, a large number of clusters contain crystallinity with the present preparation procedure.

8.5 Characterization

The ordered vanadium oxide nanocrystals found on the Au(111) surface can generally be arranged in two categories, one with a quadratic lattice structure and one with a hexagonal lattice structure. The current data has the following trends:

- With a higher substrate temperature upon deposition of V, more crystals with a hexagonal lattice are found.
- Prolonged post-annealing results in a larger number of crystals with a quadratic lattice.

The first bullet point indicates that in an excess of oxygen, the hexagonal phase is thermodynamically more stable than the quadratic, although there is a barrier for formation.

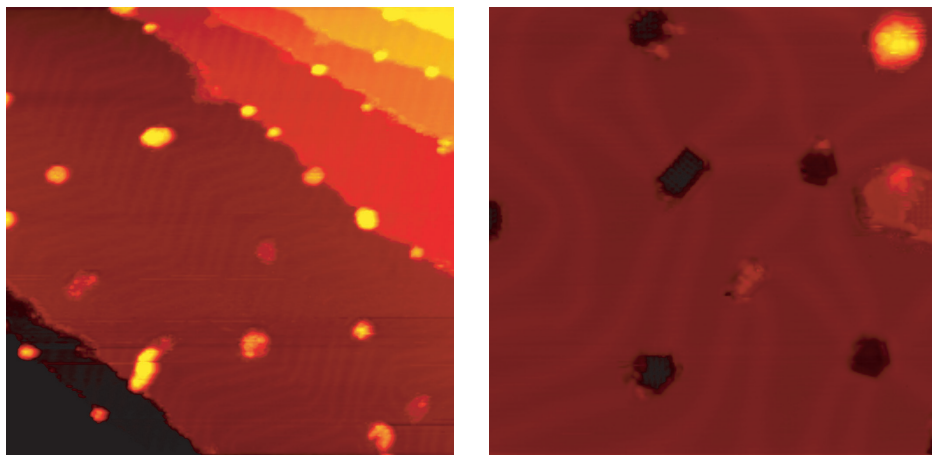


Figure 8.4: STM images of vanadium oxide nanoclusters synthesized on Au(111) surface. The clusters were crystallized through post-annealing in UHV at 673 K for 10 min. and 3 min. respectively. The size is (a) $1000 \times 1000 \text{ \AA}^2$ and (b) $300 \times 300 \text{ \AA}^2$.

Since the post-annealing is done in UHV, the second bullet point indicates that the quadratic phase is less oxidized than the hexagonal phase and thus the thermodynamically most stable configuration in UHV.

It should be stressed that the amount of data at this point is too sparse to make quantitative arguments about the relative energetics of the respective phases, and that the conclusions above could change with increased knowledge about the system.

8.5.1 Quadratic Phase

Two types of clusters with a quadratic arrangement of protrusions on the basal plane are found. Both types, which can be seen in figure 8.4 (b), vary in apparent height with tunneling conditions. In the figure, one is imaged with positive height (type A) and the other with negative height (type B). Type A has been shown (figure 8.5) to vary in height from 0.3-2.1 Å, with 2.1 Å as the high tunneling voltage value.

Type B always appears to be structurally stable, while Type A crystals often are surrounded by a cloud, indicating the presence of fast-moving adsorbates (most likely oxygen molecules), interacting with the crystal edges. Image 8.6 shows the hazy surroundings of a type A crystal.

The quadratic lattice is quite regular with a lattice constant of $3.81 \pm 0.02 \text{ \AA}$, and a typical surface corrugation of about 0.1-0.2 Å.

One side of the lattice is aligned along the rows of the unreconstructed Au(111) lattice, giving rise to rotations of multiples of 30° compared to the substrate (30° , 60° etc). With a substrate lattice constant of 2.88 Å along the Au [110] direction, the moiré ratio is 1.3 (or $\sim 4/3$), whereas perpendicularly to the [110] direction the ratio between

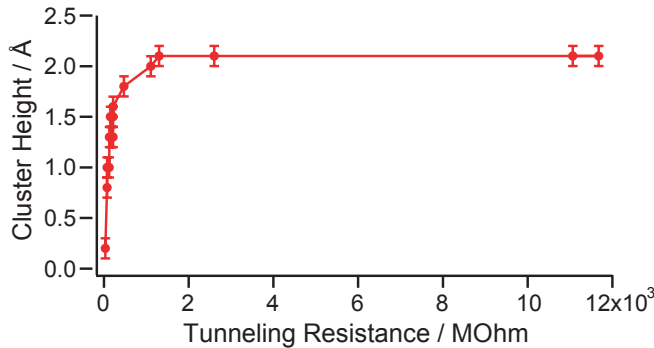


Figure 8.5: Height of type A vanadium oxide nanocluster as a function of tunneling resistance.

vanadium oxide rows and Au rows is 1.53 (or $\sim 3/2$). No moiré pattern has been seen on top of the nanocrystals (figure 8.6).

8.5.2 Hexagonal Phase

The hexagonal phase also changes its apparent height with changing tunneling parameters. No clear development in the apparent height of the hexagonal phase ($h \sim -1\text{\AA}$) as a function of tunneling voltage has been found.

Conglomerate structures consisting of triangles grown together are rather common, but also a few regular hexagons have been found.

The terminal surface has a very small corrugation ($< 0.05\text{\AA}$) with a lattice constant of $2.92 \pm 0.05 \text{\AA}$ (figure 8.7). The triangles are all rotated 30° compared to the Au(111) substrate lattice.

The edge structure, which has a corrugation of $\sim 0.1 \text{\AA}$, is reminiscent of the bright rims of the MoS₂ nanocrystals, which have a metallic edge state along the edges creating a very bright and chemically active state [190].

8.6 Discussion

An interesting development is seen in the apparent cluster height from the initial metallic V in figure 8.2 to the ordered vanadium oxide clusters with both negative and positive apparent height in figure 8.4. This change signifies the electronic change happening during the oxidation from metallic V to semi-conductive vanadium oxide. The apparent height of metallic V clusters on Au(111) (figure 8.2) does not change with the tunneling voltage between 110 mV and 1051 V (data not shown), while the graph on figure 8.5 shows that tunneling into unfilled states in the quadratically ordered vanadium oxide crystals can only take place at tunneling resistances exceeding $1000 \text{ M}\Omega$. In order to address the question of bandgap width, scanning tunneling spectroscopy (STS) is needed.

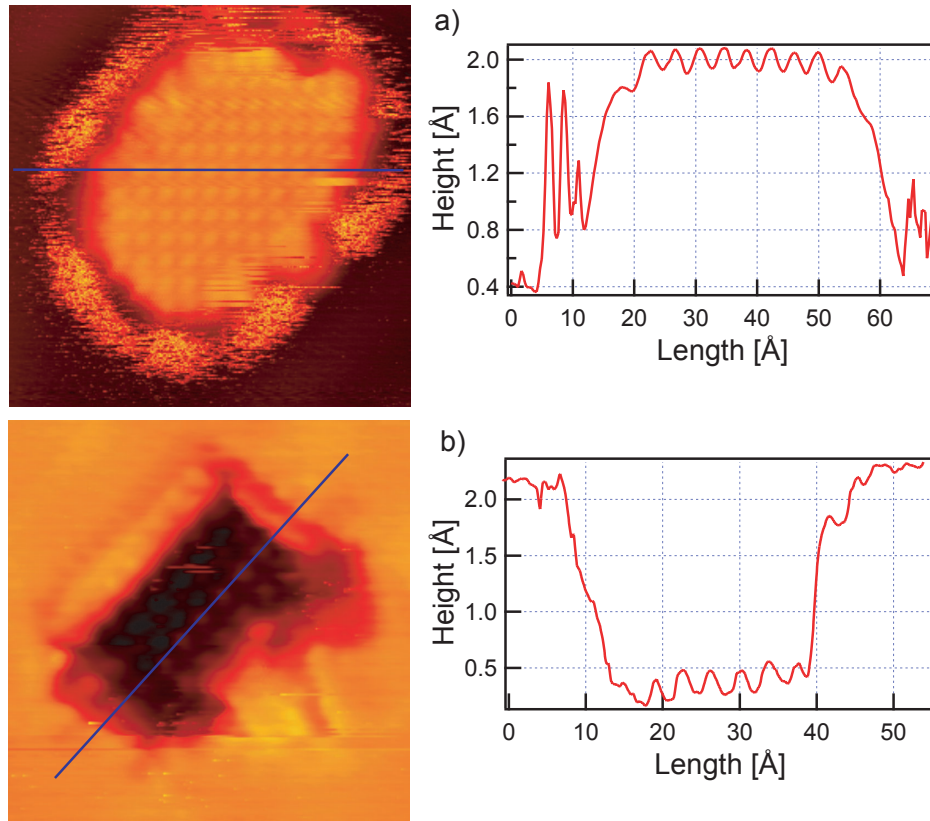


Figure 8.6: (a) STM image of type A rectangular vanadium oxide nanocluster. The regular quadratic lattice is clearly visible as well as the hazy adsorbate cloud surrounding the cluster ($70 \times 70 \text{ \AA}^2$, $V=2102 \text{ mV}$, $I=0.98 \text{ nA}$). (b) Type B rectangular vanadium oxide nanocluster ($50 \times 50 \text{ \AA}^2$, $V=2102 \text{ mV}$, $I=1.01 \text{ nA}$). Line scans across the terminal surface of the cluster are indicated by a line on the images. The line scans show the corrugation of the surface and illustrates the height differences.

STS has briefly been attempted, but at this point without conclusive results.

Gold-oxide formation in the top layer is known to happen at very high pressures of oxygen during annealing [191]. These $\sqrt{3} \times \sqrt{3}R30^\circ$ structures do not appear to bear any resemblance to the structures found here, so we disregard the possibility of surface oxide formation in the current discussion. An in-depth investigation would have to rely on theory and maybe AES or XPS to make final statements about the chemical composition of the nanocrystals.

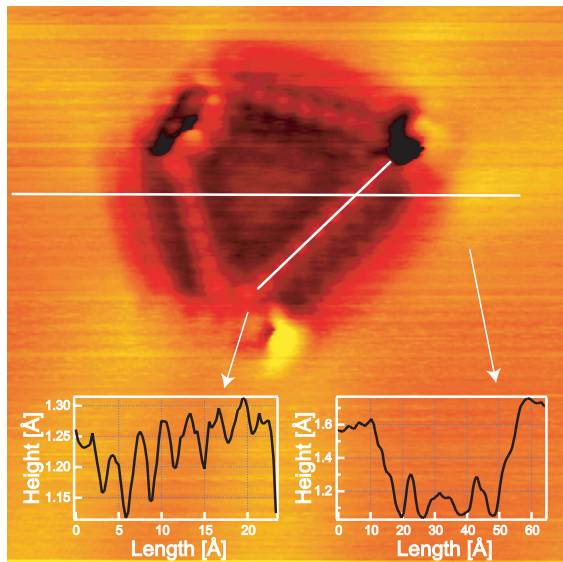


Figure 8.7: (a) STM image of hexagonal vanadium oxide nanocluster. The edge structure is clearly resolved ($70 \times 70 \text{ \AA}^2$, $V=1250 \text{ mV}$, $I=0.73 \text{ nA}$). (b) Line scan across the terminal surface of the cluster as indicated by the line on the image. The line scan shows the corrugation of the surface.

8.6.1 Quadratic Phase

The lattice constant for the quadratic structure found in the present investigations is 3.8 \AA . Previous studies of V_xO_y on Pd(111) [159] find a rectangular phase ($\text{VO}_2\text{-rect}$) with lattice constants 3.0 \AA and 3.8 \AA [159] consisting of a layer of VO (obtained from cleaving bulk VO along the (110) plane), which is oxidized on both sides to give VO_2 (see figure 8.8 (b)) [163]. The relationship between the lattice constants of the quadratic and the rectangular phases could indicate that a relationship in structure is present, but further investigations and input from theory is needed to conclude on the integral structure of the quadratic phase.

The existence of quadratic structures with two different apparent heights is suspected to be related to the number of vanadium oxide layers and/or the degree of oxidation, ie. whether the bottom of the crystal is oxidized or the crystal rests on the V atoms. In general, one would expect the bandgap to widen as the amount of oxygen in the crystal increases. The high voltage apparent height of the crystal gives a height of the quadratic phases of 2.1 \AA .

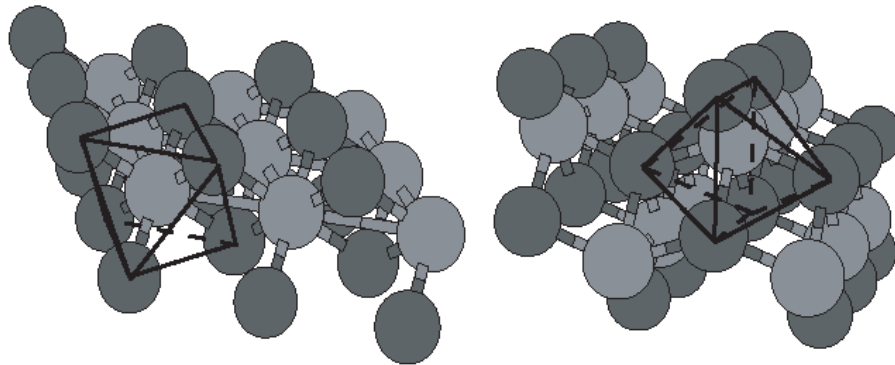


Figure 8.8: Models of the (a) hexagonal and (b) rectangular surface phases found in [163]. Taken from [163].

8.6.2 Hexagonal Phase

A hexagonal phase is also found in the Netzer experiments on Pd(111) [159], which is found to be another layer of VO, cut along the (111) plane and oxidized on both sides to give a VO_2 stoichiometry [163]. The lattice constant of the bulk VO along this plane is found to be 3.62 Å, relaxing to 2.87 Å on the Pd(111) surface. A similar lattice constant is found here (2.92 ± 0.05 Å), which is very close to that of the Au(111) (2.88 Å), indicating that the lattice of the hexagonal phase has accommodated to the substrate lattice.

It is thus concluded that the hexagonal phase found in the present study is the same as that found by Netzer/Kresse [159, 163]. In the model of the hexagonal phase (see figure 8.8 (a)) V atoms are surrounded by 6 O atoms in an octahedron structure [163]. The observed 30° rotation of the lattice is not explained, and theoretical calculations are needed to discuss this issue.

8.7 Conclusion

The preliminary study of vanadium oxide nanocrystals has illustrated that we can resolve the terminating surfaces of the oxide clusters with atomic resolution; this gives valuable information in the later identification of the actual structures of the crystals. We have found both quadratic and a hexagonal crystal phases, where the former is unidentified while the latter is most likely to be the VO_2 -hex phase also found on the Pd(111) surface in monolayer surface structures [159].

Thermodynamic arguments conclude that the lower oxides like V_2O_3 and VO_4 are more stable on surfaces [163] and in UHV [192] than V_2O_5 . To achieve this high level of oxidation would either demand annealing the structures in high pressures of oxygen, exposure of the surface to atomic oxygen or maybe the use of other oxidants like NO_2 .

These options are all available within the group through use of a high pressure cell, an atomic oxygen cracker and of course the dosing of NO₂.

Further investigations into the V_xO_y/Au(111) system will explore the energetics of the two observed phases and attempt to characterize the phases with higher resolution. Interaction studies with NO and NH₃ would be highly interesting for observation of the formation and filling of oxygen vacancies on the edges (or terminating surfaces) of the nanocrystals.

CHAPTER 9

Summary

In this chapter, the thesis will be summarized into main points and a number of interesting derived investigations will be presented.

9.1 Conclusion

In this thesis, four very different studies of the TiO₂(110) surface have been evaluated: (1) diffusion of oxygen vacancies, (2) pair interactions between oxygen vacancies, (3) nucleation and growth of Au clusters, and (4) the thermal activation of oxygen molecules.

While the studies themselves are very different and the methods vary a great deal, all four studies are interconnected through their very basic view point of the TiO₂(110) surface. The diffusion of thermally activated oxygen molecules causes the diffusion of the bridging oxygen vacancies which in turn are spread over the surface in a manner that makes it possible to evaluate the effective potentials and find the pair potential between them. This repulsive potential between the vacancies counteracts the vacancy island formation and reconstruction of the surface and thus facilitates the adsorption of atoms and molecules from the gas phase, as was the case with Au atoms nucleating in the oxygen vacancies.

The thermal activation of the oxygen atoms may be of fundamental importance for the understanding of most of the surface processes that makes titanium dioxide scientifically and technically interesting, like photocatalysis, heterogeneous catalysis and gas sensing.

9.2 Outlook

A number of derived investigations are under way at the time of writing, and with the newly gained understanding of the TiO₂(110) surface and the activation of oxygen molecules experiments are lined up. Some of the interesting projects are briefly described here:

A more complete understanding of the bridging oxygen vacancies is very interesting. The highest number of vacancies observed in these investigation is ~25%, and at this coverage the surface is very unstable with local reconstructions relieving the surface tension. Understanding the process of reconstruction on the surface may help us understand the deactivation of working catalysts.

An increase in the number of donor levels in the bandgap pins the Fermi level close to the conduction band, creating more active molecular oxygen species. The introduction of other surface dopants like Au is very interesting, as they might contribute to explaining why Au clusters on metal oxides are good catalysts for CO oxidation.

A new reaction cell has been designed with the possibility to control sample temperature (>RT), control the flow of gases impinging on the surface and measure the composition of the reaction products. This way we can test the model catalyst under working conditions with a flux of O₂ and CO onto the surface, while measuring the amount of CO₂ desorbing after oxidation.

A thorough investigation of the Au/TiO₂ model catalyst when exposed to high pressures of CO and O₂ in the high pressure cell is still in preparation.

9.3 Acknowledgements

The present work marks the end of an era for me, where physics is giving way to the creative arts and design. My past 7 years in physics have been a wonderful experience, and my colleagues deserve great thanks for their contribution.

Erik Wahlström has acted as mentor for me throughout the writing process, guiding me through the nooks and crannies of scientific writing and argumentation. Erik is one of the most talented physicists I have met, and I am happy to have had endless discussions about the fabric of the atomic world with him. Renald Schaub has lifted me out of deep holes several times with his enthusiasm for the science he creates. Renald has made life easy for us all with his professional programming work and his ability to lift the discussion. Ebbe Kruse Vestergaard is one of the most knowledgeable and thorough physicists I know, and through my interactions with Ebbe, I have learned tremendously about physics and about myself. Stig Helveg and Jeppe Vang Lauritsen's careful introduction to STM, UHV and nanocrystals on Au(111) has been valuable to me throughout my work here. I am grateful to Jeanette Dandanell for correcting large parts of the thesis for linguistic errors and typos.

Good friends at the department have done theirs to keep me afloat, and daily coffee breaks and discussions with Ebbe Kruse Vestergaard, Kristian Rechendorff and Karen Marie Hilligsøe have made the days here entertaining and sunny.

Flemming Besenbacher is thanked for making this thesis possible by standing up for me beyond his call of duty. His endless hunt for new and interesting avenues for the group to walk down along with his ability to gather incredibly talented physicists around him are very inspiring and have provided me with the possibility to grow immensely as a scientist.

The STMs created by Erik Lægsgaard are works of art, and I am deeply in debt to Erik who gave me access to the nano world, where I have roamed about these past years.

Anders Rønnau

Bibliography

- [1] V. E. Henrich and P. A. Cox, *The surface science of metal oxides* (Cambridge University Press, Cambridge, 1996).
- [2] M. Haruta, N. Yamada, T. Kobayashi, and S. Iijima, “Gold Catalysts Prepared by Coprecipitation for Low-Temperature Oxidation of Hydrogen and of Carbon Monoxide”, *J. Catal.* **115**, 301 (1989).
- [3] M. Haruta, “Size- and support-dependency in the catalysis of gold”, *Catal. Today* **36**, 153 (1997).
- [4] M. Haruta and M. Date, “Advances in the catalysis of Au nanoparticles”, *Appl. Catal. A* **222**, 427 (2001).
- [5] X. Lai, T. P. S. Clair, and D. W. Goodman, “Oxygen-induced morphological changes of Ag nanoclusters supported on TiO₂(110)”, *Faraday Discuss.* **114**, 279 (1999).
- [6] C. Xu, W. S. Oh, G. Liu, D. Y. Kim, and D. W. Goodman, “Characterization of metal clusters (Pd and Au) supported on various metal oxide surfaces (MgO and TiO₂)”, *J. Vac. Sci. Technol. A* **15**, 1261 (1997).
- [7] O. Dulub, W. Hebenstreit, and U. Diebold, “Imaging Cluster Surfaces with Atomic Resolution: The Strong Metal-Support Interaction: State of Pt Supported on TiO₂(110)”, *Phys. Rev. Lett.* **84**, 3646 (2000).
- [8] A. Berkó and F. Solymosi, “Effects of Different Gases on the Morphology of Ir Nanoparticles Supported on the TiO₂(110)-(1×2) Surface”, *J. Phys. Chem. B* **104**, 10215 (2000).
- [9] A. Fujishima and K. Honda, “Electrochemical Photolysis of Water at a Semiconductor Electrode”, *Nature* **238**, 37 (1972).
- [10] A. Linsebigler, G. Lu, and J. T. J. Yates, “Photocatalysis on TiO₂ Surfaces: Principles, Mechanisms, and Selected Results”, *Chem. Rev.* **95**, 735 (1995).
- [11] R. Asahi, T. Morikawa, T. Ohwaki, K. Aoki, and Y. Taga, “Visible-Light Photocatalysis in Nitrogen-Doped Titanium Oxides”, *Nature* **293**, 269 (2001).
- [12] W. Göpel, G. Rocker, and R. Feierabend, “Intrinsic defects of TiO₂(110): Interaction with chemisorbed O₂, H₂, CO, and CO₂”, *Phys. Rev. B* **28**, 3427 (1983).
- [13] R. Schaub, R. Thostrup, N. Lopez, E. Lægsgaard, I. Stensgaard, J. K. Nørskov, and F. Besenbacher, “Oxygen vacancies as active sites for water dissociation on rutile TiO₂(110)”, *Phys. Rev. Lett.* **87**, 6104 (2001).
- [14] J.-M. Pan, B. L. Maschhoff, U. Diebold, and T. E. Madey, “Interaction of water, oxygen, and hydrogen with TiO₂(110) surfaces having different defect densities”, *J. Vac. Sci. Technol. A* **10**, 2470 (1992).
- [15] M. A. Henderson, “Evidence for bicarbonate formation on vacuum annealed TiO₂(110) resulting from a precursor-mediated interaction between CO₂ and H₂O”, *Surf. Sci.* **400**, 203 (1998).
- [16] M. Valden, X. Lai, and D. W. Goodman, “Onset of Catalytic Activity of gold Clusters on Titania with the Appearance of Nonmetallic Properties”, *Science* **281**, 1647 (1998).

- [17] G. Binnig, H. Rohrer, C. Gerber, and E. Weibel, “Surface Studies by Scanning Tunneling Microscopy”, *Phys. Rev. Lett.* **49**, 57 (1982).
- [18] “The Official Web Site of The Nobel Foundation”,, <http://www.nobel.se/physics/laureates/1986/press.html>, 1986.
- [19] F. Besenbacher, “Scanning tunnelling microscopy studies of metal surfaces”, *Rep. Prog. Phys.* **59**, 1737 (1996).
- [20] R. Wiesendanger, *Scanning Probe Microscopy and Spectroscopy: Methods and Applications* (Cambridge University Press, Cambridge, 1994).
- [21] E. Lægsgaard, F. Besenbacher, K. Mortensen, and I. Stensgaard, “A fully automated, ‘thimble-size’ scanning tunnelling microscope”, *J. Microscop.* **152**, 663 (1988).
- [22] F. Besenbacher and J. K. Nørskov, “Oxygen chemisorption on metal surfaces: general trends for Cu, Ni and Ag”, *Prog. Surf. Sci.* **44**, 5 (1993).
- [23] T. R. Linderoth, S. Horch, L. Petersen, S. Helveg, E. Lægsgaard, I. Stensgaard, and F. Besenbacher, “Novel Mechanism for Diffusion of One-Dimensional Clusters: Pt/Pt(110)-(1×2)”, *Phys. Rev. Lett.* **82**, 1494 (1999).
- [24] K. H. Hansen, T. Worren, E. Lægsgaard, F. Besenbacher, and I. Stensgaard, “Bias dependent apparent height of an Al₂O₃ thin film on NiAl(110), and of supported Pd clusters”, *Surf. Sci.* **475**, 96 (2001).
- [25] J. Tersoff and D. R. Hamann, “Theory and Application for the Scanning Tunneling Microscope”, *Phys. Rev. Lett.* **50**, 1998 (1983).
- [26] J. Bardeen, “Tunneling from a Many-Particle Point of View”, *Phys. Rev. Lett.* **6**, 57 (1961).
- [27] J. Tersoff and D. R. Hamann, “Theory of the scanning tunneling microscope”, *Phys. Rev. B* **31**, 805 (1985).
- [28] J. Winterlin, R. Schuster, and G. Ertl, “Existence of a “Hot” Atom Mechanism for the Dissociation of O₂ on Pt(111)”, *Phys. Rev. Lett.* **77**, 123 (1996).
- [29] M. . Pedersen, L. Österlund, J. J. Mortensen, M. Mavrikakis, L. B. Hansen, I. Stensgaard, E. Lægsgaard, J. K. Nørskov, and F. Besenbacher, “Diffusion of N Adatoms on the Fe(100) Surface”, *Phys. Rev. Lett.* **84**, 4898 (2000).
- [30] G. Meyer, B. Neu, and K. H. Rieder, “Controlled Lateral Manipulation of Single Molecules with the Scanning Tunneling Microscope”, *Appl. Phys. A* **60**, 343 (1995).
- [31] N. D. Lang, “Vacuum Tunneling Current from an Adsorbed Atom”, *Phys. Rev. Lett.* **55**, 230 (1985).
- [32] N. D. Lang, “Theory of Single-Atom Imaging in the Scanning Tunneling Microscope”, *Phys. Rev. Lett.* **56**, 1164 (1986).
- [33] P. Sautet, “Images of Adsorbates with the Scanning Tunneling Microscope: Theoretical Approaches to the Contrast Mechanism”, *Chem. Rev.* **97**, 1097 (1997).
- [34] U. Diebold, “The surface science of titanium dioxide”, *Surf. Sci. Rep.* **48**, 53 (2003).
- [35] M. A. Henderson, “Mechanism for the bulk-assisted reoxidation of ion sputtered TiO₂ surfaces: Diffusion of oxygen to the surface or titanium to the bulk?”, *Surf. Sci.* **343**, L1156 (1995).
- [36] M. A. Henderson, “An HREELS and TPD study of water on TiO₂(110): The extent of molecular versus dissociative adsorption”, *Surf. Sci.* **355**, 151 (1996).
- [37] M. A. Henderson, “Structural Sensitivity in the Dissociation of Water on TiO₂ Single-Crystal Surfaces”, *Langmuir* **12**, 5093 (1996).
- [38] W. S. Epling, C. H. F. Peden, M. A. Henderson, and U. Diebold, “Evidence for oxygen adatoms on TiO₂(110) resulting from O₂ dissociation at vacancy sites”, *Surf. Sci.* **412-413**, 333 (1998).
- [39] M. A. Henderson, “A surface perspective on self-diffusion in rutile TiO₂”, *Surf. Sci.* **419**, 174 (1999).
- [40] M. A. Henderson, W. S. Epling, C. L. Perkins, and C. H. F. Peden, “Interaction of Molecular Oxygen with the Vacuum-Annealed TiO₂(110) Surface: Molecular and Dissociative Channels”, *J. Phys. Chem.* **103**, 5328 (1999).

- [41] A. Linsebigler, G. Lu, and J. T. J. Yates, "CO chemisorption on TiO₂(110): Oxygen vacancy site influence on CO adsorption", *J. Phys. Chem.* **103**, 9438 (1995).
- [42] A. Linsebigler, G. Lu, and J. T. J. Yates, "CO Photooxidation on TiO₂(110)", *J. Phys. Chem.* **100**, 6631 (1996).
- [43] G. Lu, A. Linsebigler, and J. T. Yates, "Ti³⁺ Defect Sites on TiO₂(110): Production and Chemical Detection of Active Sites", *J. Phys. Chem.* **98**, 11733 (1994).
- [44] G. Q. Lu, A. Linsebigler, and J. T. Yates, "The Photochemical Identification of 2 Chemisorption States for Molecular-Oxygen on TiO₂(110)", *J. Chem. Phys.* **102**, 3005 (1995).
- [45] G. Q. Lu, A. Linsebigler, and J. T. Yates, "The Adsorption and Photodesorption of Oxygen on the TiO₂(110) Surface", *J. Chem. Phys.* **102**, 4657 (1995).
- [46] C. N. Rusu and J. T. J. Yates, "Defect Sites on TiO₂(110). Detection by O₂ Photodesorption", *Langmuir* **13**, 4311 (1997).
- [47] F. A. Cotton, G. Wilkinson, and P. L. Gaus, *Basic Inorganic Chemistry*, 3 ed. (John Wiley and Sons Ltd., Chichester, New York, 1995).
- [48] S. Elliott, *The Physics And Chemistry Of Solids* (John Wiley and Sons Ltd., Chichester, New York, 1998).
- [49] T. Bredow and G. Pacchioni, "Electronic structure of an isolated oxygen vacancy at the TiO₂(110) surface", *Chem. Phys. Lett.* **355**, 417 (2002).
- [50] P. van der Krogt, "Elementymology & Elements Multidict", <http://www.vanderkrogt.net/elements/elem/ti.html>.
- [51] M. Winter, "WebElements: The Periodic Table on the WWW", <http://www.webelements.com/webelements/scholar/elements/titanium/history.html>.
- [52] D. C. Cronemeyer, "Infrared Absorption of Reduced Rutile TiO₂ Single Crystals", *Phys. Rev.* **113**, 1222 (1956).
- [53] C. R. Henry, "Surface studies of supported model catalysts", *Surf. Sci. Rep.* **31**, 235 (1998).
- [54] M. Haruta, "Catalysis of Gold Nanoparticles Deposited on Metal Oxides", *CATTECH* **6**, 102 (2002).
- [55] C. C. Chusuei, X. Lai, K. Luo, and D. W. Goodman, "Modeling heterogeneous catalysts: metal clusters on planar oxide supports", *Topics Catal.* **14**, 71 (2001).
- [56] M. Grätzel, "Photoelectrochemical cells", *Nature* **414**, 338 (2001).
- [57] *Photocatalysis - Fundamentals and Applications*, edited by N. Serpone and E. Pelizzetti (John Wiley & Sons, New York, 1989).
- [58] B. Kasemo and J. Gold, "Implant Surfaces and Interface Processes", *Adv. Dent. Res.* **13**, 8 (1999).
- [59] A. Fujishima, T. N. Rao, and A. D. Tryk, "Titanium dioxide photocatalysis", *J. Photochem. Photobiol. C: Photochem. Rev.* **1**, 1 (2000).
- [60] H. K. Pulker, G. Paesold, and E. Ritter, "Refractive-Indexes of TiO₂ Films Produced by Reactive Evaporation of Various Titanium-Oxygen Phases", *Applied Optics* **15**, 2986 (1976).
- [61] A. Heller, "Chemistry and Applications of Photocatalytic Oxidation of Thin Organic Films", *Acc. Chem. Res.* **28**, 503 (1995).
- [62] U. Gesenhues and T. Rentschler, "Crystal growth and defect structure of Al³⁺-doped rutile", *Journal of Solid State Chemistry* **143**, 210 (1999).
- [63] NASA, "National Aeronautics and Space Administration", <http://www.nasa.gov>.
- [64] R. W. G. Wyckoff, *Crystal Structures*, 2 ed. (John Wiley and Sons Ltd., Chichester, New York, 1963), Vol. 1.
- [65] K. M. Glassford and J. R. Chelikowsky, "Structural and Electronic-Properties of Titanium-Dioxide", *Phys. Rev. B* **46**, 1284 (1992).
- [66] S. Munnix and M. Schmeits, "Electronic structure of ideal TiO₂(110), TiO₂(001), and TiO₂(100) surfaces", *Phys. Rev. B* **30**, 2207 (1984).

- [67] U. Diebold, M. Li, O. Dulub, E. L. D. Hebenstreit, and W. Hebenstreit, “The relationship between bulk and surface properties of rutile $\text{TiO}_2(110)$ ”, *Surf. Rev. Lett.* **7**, 613 (2000).
- [68] D. C. Cronemeyer, “Electrical and Optical Properties of Rutile Single Crystals”, *Phys. Rev.* **87**, 876 (1952).
- [69] R. B. Breckenridge and W. R. Hosler, “Electrical properties of titanium dioxide semiconductors”, *Phys. Rev.* **91**, 793 (1953).
- [70] J. H. Becker and W. R. Hosler, “Multiple-Band Conduction in n-type rutile (TiO_2)”, *Phys. Rev.* **137**, A1972 (1965).
- [71] N. W. Ashcroft and N. D. Mermin, *Solid State Physics* (Saunders College Publishing, New York, 1976).
- [72] E. Yagi, R. R. Hasiguti, and M. Aono, “Electronic conduction above 4 K of slightly reduced oxygen-deficient rutile TiO_{2-x} ”, *Phys. Rev. B* **54**, 7945 (1996).
- [73] N. C. Yu and J. W. Halley, “Electronic-Structure of Point-Defects in Rutile TiO_2 ”, *Phys. Rev. B* **51**, 4768 (1995).
- [74] M. Ramamoorthy, R. D. King-Smith, and D. Vanderbilt, “Defects on $\text{TiO}_2(110)$ surfaces”, *Phys. Rev. B* **49**, 7709 (1994).
- [75] U. Diebold, J. Lehman, T. Mahmoud, M. Kuhn, G. Leonardelli, W. Hebenstreit, M. Schmid, and P. Varga, “Intrinsic defects on a $\text{TiO}_2(110)(1\times 1)$ surface and their reaction with oxygen: a scanning tunneling microscopy study”, *Surf. Sci.* **411**, 137 (1998).
- [76] A. Zangwill, *Physics at surfaces* (Cambridge University Press, Cambridge, 1988).
- [77] G. Charlton, P. B. Howes, C. L. Nicklin, P. Steadman, J. S. G. Taylor, C. A. Muryn, S. P. Harte, J. Mercer, R. McGrath, D. Norman, T. S. Turner, and G. Thornton, “Relaxation of $\text{TiO}_2(110)-(1\times 1)$ Using Surface X-Ray Diffraction”, *Phys. Rev. Lett.* **78**, 495 (1997).
- [78] P. Stone, R. A. Bennett, and M. Bowker, “Reactive re-oxidation of reduced $\text{TiO}_2(110)$ surfaces demonstrated by high temperature STM movies”, *New J. Phys.* **1**, 8 (1999).
- [79] G. S. Rohrer, V. E. Henrich, and D. A. Bonnell, “Structure of the Reduced $\text{TiO}_2(110)$ Surface Determined by Scanning Tunneling Microscopy”, *Science* **250**, 1239 (1990).
- [80] D. Novak, E. Garfunkel, and T. Gustafsson, “Scanning-tunneling-microscopy study of the atomic-scale structure of $\text{TiO}_2(110)-(1\times 1)$ ”, *Phys. Rev. B* **50**, 5000 (1994).
- [81] U. Diebold, J. F. Anderson, K.-O. Ng, and D. Vanderbilt, “Evidence for the Tunneling Site on Transition-Metal Oxides: $\text{TiO}_2(110)$ ”, *Phys. Rev. Lett.* **77**, 1322 (1996).
- [82] W. Kohn, “Nobel Lecture: Electronic structure of matter — wave functions and density functionals”, *Rev. Mod. Phys.* **71**, 1253 (1999).
- [83] M. Springborg, *Density-Functional Methods in Chemistry and Materials Science* (John Wiley and Sons Ltd., Chichester, New York, 1997).
- [84] S. Holloway and J. Nørskov, *Bonding at Surfaces* (University of Liverpool Press, Liverpool, UK, 1991).
- [85] S. P. Bates, G. Kresse, and M. J. Gillan, “A systematic study of the surface energetics and structure of $\text{TiO}_2(110)$ by first-principles calculations”, *Surf. Sci.* **385**, 386 (1997).
- [86] M. D. Rasmussen, L. Molina, and B. Hammer, “Adsorption, diffusion and dissociation of molecular oxygen at defected $\text{TiO}_2(110)$ – a DFT study”, *In Preparation* (2003).
- [87] A. Vijay, G. Mills, and H. Metiu, “Adsorption of gold on stoichiometric and reduced rutile $\text{TiO}_2(110)$ surfaces”, *J. Chem. Phys.* **118**, 6536 (2003).
- [88] S. D. Elliott and S. P. Bates, “Energetically accessible reconstructions along interstitial rows on the rutile (110) surface”, *Phys. Chem. Chem. Phys.* **3**, 1954 (2001).
- [89] A. T. Paxton and L. Thiên-Nga, “Electronic structure of reduced titanium dioxide”, *Phys. Rev. B* **57**, 1579 (1998).
- [90] D. Vogtenhuber, R. Podloucky, A. Neckel, S. G. Steinemann, and A. J. Freeman, “Electronic structure and relaxed geometry of the TiO_2 rutile (110) surface”, *Phys. Rev. B* **49**, 2099 (1994).

- [91] P. J. D. Lindan, N. M. Harrison, M. J. Gillan, and J. A. White, "First-principles spin-polarized calculations on the reduced and reconstructed TiO₂(110) surface", *Phys. Rev. B* **55**, 15919 (1997).
- [92] S. Suzuki, K. Fukui, H. Onishi, and Y. Iwasawa, "Hydrogen Adatoms on TiO₂(110)-(1×1) Characterized by Scanning Tunneling Microscopy and Electron Stimulated Desorption", *Phys. Rev. Lett.* **84**, 2156 (2000).
- [93] V. E. Henrich and R. L. Kurtz, "Surface Electronic-Structure of TiO₂ - Atomic Geometry, Ligand Coordination, and the Effect of Adsorbed Hydrogen", *Phys. Rev. B* **23**, 6280 (1981).
- [94] J. Leconte, A. Markovits, M. K. Skalli, C. Minot, and A. Belmajdoub, "Periodic ab initio study of the hydrogenated rutile TiO₂(110) surface", *Surf. Sci.* **497**, 194 (2002).
- [95] M. Menetrey, A. Markovits, and C. Minot, "Reactivity of a reduced metal oxide surface: hydrogen, water and carbon monoxide adsorption on oxygen defective rutile TiO₂(110)", *Surf. Sci.* **524**, 49 (2003).
- [96] C. Wöll, Unpublished, 2003.
- [97] T. Fujino, M. Katayama, K. Inudzuka, T. Okuno, K. Oura, and T. Hirao, "Surface hydroxyl formation on vacuum-annealed TiO₂(110)", *Appl. Phys. Lett.* **79**, 2716 (2001).
- [98] R. Schaub and M. Vestergaard, Unpublished, 2003.
- [99] O. W. Johnson, S. H. Paek, and J. W. Deford, "Diffusion of H and D in TiO₂ - Suppression of Internal Fields by Isotope-Exchange", *J. Appl. Phys.* **46**, 1026 (1975).
- [100] J. B. Bates, J. C. Wang, and R. A. Perkins, "Mechanisms for Hydrogen Diffusion in TiO₂", *Phys. Rev. B* **19**, 4130 (1979).
- [101] R. L. Kurtz, R. Stockbauer, T. E. Madey, E. Román, and J. L. de Segovia, "Synchrotron radiation studies of H₂O adsorption on TiO₂(110)", *Surf. Sci.* **218**, 178 (1989).
- [102] M. P. de Lara-Castells and J. L. Krause, "Theoretical study of the interaction of molecular oxygen with a reduced TiO₂ surface", *Chem. Phys. Lett.* **354**, 483 (2002).
- [103] M. A. Henderson, "The interaction of water with solid surfaces: fundamental aspects revisited", *Surf. Sci. Rep.* **46**, 1 (2002).
- [104] M. B. Hugenschmidt, L. Gamble, and C. T. Campbell, "The interaction of H₂O with a TiO₂(110) surface", *Surf. Sci.* **302**, 329 (1994).
- [105] D. Brinkley, M. Dietrich, T. Engel, P. Farrall, G. Gantner, A. Schafer, and A. Szuchmacher, "A modulated molecular beam study of the extent of H₂O dissociation on TiO₂(110)", *Surf. Sci.* **395**, 292 (1998).
- [106] V. E. Henrich, G. Dresselhaus, and H. J. Zeiger, "Chemisorbed phases of H₂O on TiO₂ and SrTiO₃", *Solid State Commun.* **24**, 623 (1977).
- [107] G. A. Somorjai, *Surface Chemistry and Catalysis* (Wiley, New York, 1994).
- [108] J. Carrey, J.-L. Maurice, F. Petroff, and A. Vaurès, "Growth of Au Clusters on Amorphous Al₂O₃: Evidence of Cluster Mobility above a Critical Size", *Phys. Rev. Lett.* **86**, 4600 (2001).
- [109] S. Gan, Y. Liang, D. R. Baer, and A. W. Grant, "Effects of titania surface structure on the nucleation and growth of Pt nanoclusters on rutile TiO₂(110)", *Surf. Sci.* **475**, 159 (2001).
- [110] N. Spiridis, J. Haber, and J. Korecki, "STM studies of Au nano-clusters on TiO₂(110)", *Vacuum* **63**, 99 (2001).
- [111] H. S. Taylor, "A Theory of the Catalytic Surface", *Proc. R. Soc. London, Ser. A* **108**, 105 (1925).
- [112] G. R. Bamwenda, S. Tsubota, T. Nakamura, and M. Haruta, "The influence of the preparation methods on the catalytic activity of platinum and gold supported on TiO₂ for CO oxidation", *Catal. Lett.* **44**, 83 (1997).
- [113] V. E. Henrich, "Metal-oxide surfaces", *Prog. Surf. Sci.* **50**, 77 (1995).
- [114] S. Horch, H. T. Lorenzen, S. Helveg, E. Lægsgaard, I. Stensgaard, K. W. Jacobsen, J. K. Nørskov, and F. Besenbacher, "Enhancement of surface self-diffusion of platinum atoms by adsorbed hydrogen", *Nature* **398**, 134 (1999).

- [115] R. v. Gastel, E. Somfai, S. B. v. Albada, W. v. Saarloos, and J. W. M. Frenken, "Nothing Moves a Surface: Vacancy Mediated Surface Diffusion", *Phys. Rev. Lett.* **86**, 1562 (2001).
- [116] R. Schaub, E. Wahlström, A. Rønnau, E. Lægsgaard, I. Stensgaard, and F. Besenbacher, "Oxygen-Mediated Diffusion of Oxygen Vacancies on the TiO₂(110) Surface.", <http://www.phys.au.dk/camp/hot0027.htm>, online material is supporting material for Paper I.
- [117] U. Diebold, Personal communications, 2003.
- [118] R. Schaub, E. Wahlström, A. Rønnau, E. Lægsgaard, I. Stensgaard, and F. Besenbacher, "Oxygen-Mediated Diffusion of Oxygen Vacancies on the TiO₂(110) Surface", *Science* **299**, 377 (2003).
- [119] L. Österlund, M. . Pedersen, I. Stensgaard, E. Lægsgaard, and F. Besenbacher, "Quantitative Determination of Adsorbate-Adsorbate Interactions", *Phys. Rev. Lett.* **83**, 4812 (1999).
- [120] T. T. Tsong, "Field-Ion Microscope Observations of Indirect Interaction between Adatoms on Metal-Surfaces", *Phys. Rev. Lett.* **31**, 1207 (1973).
- [121] J. Trost, T. Zambelli, J. Winterlin, and G. Ertl, "Adsorbate-adsorbate interactions from statistical analysis of STM images: N/Ru(0001)", *Phys. Rev. B* **54**, 17850 (1996).
- [122] A. J. Mayne, F. Rose, C. Bolis, and G. Dujardin, "An scanning tunnelling microscopy study of the diffusion of a single or a pair of atomic vacancies", *Surf. Sci.* **486**, 226 (2001).
- [123] F. A. Grant, "Properties of Rutile (Titanium Dioxide)", *Rev. Mod. Phys.* **31**, 646 (1959).
- [124] J. Repp, F. Moresco, G. Meyer, K.-H. Rieder, P. Hyldgaard, and M. Persson, "Substrate Mediated Long-Range Oscillatory Interaction between Adatoms: Cu/Cu(111)", *Phys. Rev. Lett.* **85**, 2981 (2000).
- [125] T. L. Hill, *Statistical Mechanics* (McGraw-Hill Book Company, New York, 1956).
- [126] D. P. Landau and K. Binder, *A Guide to Monte Carlo Simulations in Statistical Physics* (Cambridge University Press, Cambridge, 2000).
- [127] N. Metropolis, A. W. Rosenbluth, M. N. Rosenbluth, A. H. Teller, and E. Teller, "Equation of State Calculations by Fast Computing Machines", *J. Chem. Phys.* **21**, 1087 (1953).
- [128] P. Stoltze, *Simulation Methods in Atomic-scale Materials Physics* (Polyteknisk Forlag, Lyngby, Denmark, 1997).
- [129] J. N. Israelachvili, *Intermolecular and surface forces*, 2 ed. (Academic Press, London, 1994).
- [130] K. H. Lau and W. Kohn, "Elastic Interaction of 2 Atoms Adsorbed on a Solid-Surface", *Surf. Sci.* **65**, 607 (1977).
- [131] N. M. Harrison, X.-G. Wang, J. Muscat, and M. Scheffler, "The influence of soft vibrational modes on our understanding of oxide surface structure", *Faraday Discuss.* **114**, 305 (1999).
- [132] J. Oviedo and M. J. Gillan, "The energetics and structure of oxygen vacancies on the SnO₂(110) surface", *Surf. Sci.* **467**, 35 (2000).
- [133] M. Valden, S. Pak, X. Lai, and D. W. Goodman, "Structure sensitivity of CO oxidation over model Au/TiO₂ catalysts", *J. Catal.* **56**, 7 (1998).
- [134] M. Okumura, S. Nakamura, S. Tsubota, T. Nakamura, M. Azuma, and M. Haruta, "Chemical vapor deposition of gold on Al₂O₃, SiO₂, and TiO₂ for the oxidation of CO and of H₂", *Catal. Lett.* **51**, 53 (1998).
- [135] F. Bocuzzi, A. Chiorino, and M. Manzoli, "Au/TiO₂ nanostructured catalyst: pressure and temperature effects on the FTIR spectra of CO adsorbed at 90 K", *Surf. Sci.* **502-503**, 513 (2002).
- [136] M. A. Bollinger and M. A. Vannice, "A kinetic and DRIFTS study of low temperature carbon monoxide oxidation over Au-TiO₂ catalysts", *Appl. Catal. B* **8**, 417 (1996).
- [137] Z. M. Liu and M. A. Vannice, "CO and O₂ adsorption on model Au-TiO₂ systems", *Catal. Lett.* **43**, 51 (1997).
- [138] J. Jacobsen, B. Hammer, K. W. Jacobsen, and J. K. Nørskov, "Electronic structure, total energies, and STM images of clean and oxygen-covered Al(111)", *Phys. Rev. B* **52**, 14954 (1995).

- [139] N. Lopez and J. K. Nørskov, "Theoretical study of the Au/TiO₂(110) interface", *Surf. Sci.* **515**, 175 (2002).
- [140] A. Sanchez, S. Abbet, U. Heiz, W.-D. Schneider, H. Häkkinen, R. N. Barnett, and U. Landman, "When Gold Is Not Noble: Nanoscale Gold Catalysts", *J. Phys. Chem. A* **103**, 9573 (1999).
- [141] F. Cosandey and T. E. Madey, "Growth, morphology, interfacial effects and catalytic properties of Au on TiO₂", *Surf. Rev. Lett.* **8**, 73 (2001).
- [142] S. C. Parker, A. W. Grant, V. A. Bondzie, and C. T. Campbell, "Island growth kinetics during the vapor deposition of gold onto TiO₂(110)", *Surf. Sci.* **441**, 10 (1999).
- [143] G. Ehrlich and F. G. Hudda, "Atomic View of Surface Self-Diffusion: Tungsten on Tungsten", *J. Chem. Phys.* **44**, 1036 (1966).
- [144] E. L. D. Hebenstreit, W. Hebenstreit, H. Geisler, C. A. V. Jr., P. T. Sprunger, and U. Diebold, "Bulk-defect dependent adsorption on a metal oxide surface: S/TiO₂(110)", *Surf. Sci.* **486**, L467 (2001).
- [145] A. Yamakata, T. Ishibashi, and H. Onishi, "Water- and Oxygen-Induced Decay Kinetics of Photogenerated Electrons in TiO₂ and Pt/TiO₂: A Time-Resolved Infrared Absorption Study", *J. Phys. Chem. B* **105**, 7258 (2001).
- [146] N.-Y. Topsøe, *Infrared Spectroscopy Investigations of Environmental DeNOx and Hydrotreating Catalysts* (Haldor Topsøe Research Laboratories, Lyngby, Denmark, 1998).
- [147] W. Hebenstreit, N. Ruzycki, G. S. Herman, Y. Gao, and U. Diebold, "Scanning tunneling microscopy investigation of the TiO₂ anatase (101) surface", *Phys. Rev. B* **62**, R16334 (2000).
- [148] J. Biener, M. Bäumer, J. Wang, and R. J. Madix, "Electronic structure and growth of vanadium on TiO₂(110)", *Surf. Sci.* **450**, 12 (2000).
- [149] N. J. Price, J. B. Reitz, R. J. Madix, and E. I. Solomon, "A synchrotron XPS study of the vanadia-titania system as a model for monolayer oxide catalysts", *J. Electr. Spectr. Rel. Phenom.* **99**, 257 (1999).
- [150] M. D. Negra, M. Sambi, and G. Granozzi, "Ultrathin VO_x/TiO₂(110) ($x \approx 1$) film preparation by controlled oxidation of metal deposits", *Surf. Sci.* **436**, 227 (1999).
- [151] M. Sambi, M. D. Negra, and G. Granozzi, "The structure of vanadia ultrathin films grown on TiO₂(110) in an oxygen ambient", *Surf. Sci.* **470**, L116 (2000).
- [152] Q. Guo, S. Lee, and D. W. Goodman, "Vanadium oxides thin films grown on rutile TiO₂(110)-(1 × 1) and (1 × 2) surfaces", *Surf. Sci.* **437**, 38 (1999).
- [153] G. S. Wong, M. R. Concepcion, and J. M. Vohs, "Reactivity of monolayer V₂O₅ films on TiO₂(110) produced via the oxidation of vapor-deposited vanadium", *Surf. Sci.* **526**, 211 (2003).
- [154] J. Biener, J. Wang, and R. J. Madix, "Direct observation of the growth of vanadium on TiO₂(110)-(1 × 2)", *Surf. Sci.* **442**, 47 (1999).
- [155] M. Sambi, M. D. Negra, G. Granozzi, Z. S. Li, J. H. Jorgensen, and P. J. Moller, "An ARPEFS study of the structure of an epitaxial VO₂ monolayer at the TiO₂ (110) surface", *Appl. Surf. Sci.* **142**, 146 (1999).
- [156] P. J. Moller, Z. S. Li, T. Egebjerg, M. Sambi, and G. Granozzi, "Synchrotron-radiation-induced photoemission study of VO₂ ultrathin films deposited on TiO₂(110)", *Surf. Sci.* **404**, 719 (1998).
- [157] M. D. Negra, M. Sambi, and G. Granozzi, "The structure of an ultrathin VO_x ($x \approx 1$) film grown epitaxially on TiO₂ (110)", *Surf. Sci.* **461**, 118 (2000).
- [158] S. Surnev, L. Vitali, M. G. Ramsey, F. P. Netzer, G. Kresse, and J. Hafner, "Growth and structure of ultrathin vanadium oxide layers on Pd(111)", *Phys. Rev. B* **61**, 13945 (2000).
- [159] S. Surnev, G. Kresse, M. G. Ramsey, and F. P. Netzer, "Novel interface-mediated metastable oxide phases: Vanadium oxides on Pd(111)", *Phys. Rev. Lett.* **87**, 086102 (2001).
- [160] M. Sambi, M. Petukhov, B. Domenichini, G. A. Rizzi, S. Surnev, G. Kresse, F. P. Netzer, and G. Granozzi, "A photoelectron diffraction study of the surface-V₂O₃ (2 × 2) layer on Pd(111)", *Surf. Sci.* **529**, L234 (2003).

- [161] F. P. Leisenberger, S. Surnev, L. Vitali, M. G. Ramsey, and F. P. Netzer, "Nature, growth, and stability of vanadium oxides on Pd(111)", *J. Vac. Sci. Technol. A* **17**, 1743 (1999).
- [162] S. Surnev, G. Kresse, M. Sock, M. G. Ramsey, and F. P. Netzer, "Surface structures of ultrathin vanadium oxide films on Pd(111)", *Surf. Sci.* **495**, 91 (2001).
- [163] G. Kresse, S. Surnev, M. G. Ramsey, and F. P. Netzer, "First-principles calculations for V_xO_y grown on Pd(111)", *Surf. Sci.* **492**, 329 (2001).
- [164] B. Hammer and J. K. Nørskov, "Electronic factors determining the reactivity of metal surfaces", *Surf. Sci.* **343**, 211 (1995).
- [165] H. Hannemann, C. A. Ventrice, T. Bertrams, A. Brodde, and H. Neddermeyer, "Scanning-Tunneling Microscopy on the Growth of Ordered NiO Layers on Au(111)", *Phys. Stat. Sol. (a)* **146**, 289 (1994).
- [166] C. A. Ventrice, T. Bertrams, H. Hannemann, A. Brodde, and H. Neddermeyer, "Stable Reconstruction of the Polar (111) Surface of NiO on Au(111)", *Phys. Rev. B* **49**, 5773 (1994).
- [167] I. Sebastian, M. Heiler, K. Meinel, and H. Neddermeyer, "Growth of epitaxial layers of Co and CoO on Au(111)", *Appl. Phys. A* **66**, S525 (1998).
- [168] A. Rønnaug, "STM Studies of MoS₂ Nanocrystals on the Au(111) Surface", Bachelor of Physics Report, 2003.
- [169] S. Helveg, J. V. Lauritsen, E. Lægsgaard, I. Stensgaard, J. K. Nørskov, B. S. Clausen, H. Topsøe, and F. Besenbacher, "Atomic-Scale Structure of Single-Layer MoS₂ Nanoclusters", *Phys. Rev. Lett.* **84**, 951 (2000).
- [170] J. V. Lauritsen, S. Helveg, E. Lægsgaard, I. Stensgaard, B. S. Clausen, H. Topsøe, and F. Besenbacher, "Atomic-Scale Structure of Co-Mo-S Nanoclusters in Hydrotreating Catalysts", *J. Catal.* **197**, 1 (2001).
- [171] M. V. Bollinger, J. V. Lauritsen, K. W. Jacobsen, J. K. Nørskov, S. Helveg, and F. Besenbacher, "One-Dimensional Metallic Edge States in MoS₂", *Phys. Rev. Lett.* **87**, 196803 (2001).
- [172] K.-M. Ho and K. P. Bohnen, "Stability of the missing-row reconstruction on fcc (110) transition-metal surfaces", *Phys. Rev. Lett.* **59**, 1833 (1987).
- [173] V. Fiorentini, M. Methfessel, and M. Scheffler, "Reconstruction Mechanism of fcc Transition Metal (001) Surfaces", *Phys. Rev. Lett.* **71**, 1051 (1993).
- [174] J. V. Barth, H. Brune, G. Ertl, and R. J. Behm, "Scanning tunneling microscopy observations on the reconstructed Au(111) surface: Atomic structure, long-range superstructure, rotational domains, and surface defects", *Phys. Rev. B* **42**, 9307 (1990).
- [175] D. D. Chambliss, R. J. Wilson, and S. Chiang, "Nucleation of Ordered Ni Island Arrays on Au(111) by Surface-Lattice-Dislocations", *Phys. Rev. Lett.* **66**, 1721 (1991).
- [176] S. Narasimhan and D. Vanderbilt, "Elastic Stress Domains and the Herringbone Reconstruction on Au(111)", *Phys. Rev. Lett.* **69**, 1564 (1992).
- [177] B. Voigtländer, G. Meyer, and N. M. Amer, "Epitaxial-Growth of Thin Magnetic Cobalt Films on Au(111) Studied by Scanning Tunneling Microscopy", *Phys. Rev. B* **44**, 10354 (1991).
- [178] E. Kopatzki, I. D. Baikie, R. J. Behm, and J. A. Meyer, "Preferential island nucleation at the elbows of the Au(111) herringbone reconstruction through place exchange", *Surf. Sci. Lett.* **365**, L647 (1996).
- [179] M. Böhringer, K. Morgenstern, W.-D. Schneider, R. Berndt, F. Mauri, A. D. Vita, and R. Car, "Two-Dimensional Self-Assembly of Supramolecular Clusters and Chains", *Phys. Rev. Lett.* **83**, 324 (1999).
- [180] D. D. Chambliss, R. J. Wilson, and S. Chiang, "Ordered Nucleation of Ni and Au Islands on Au(111) Studied by Scanning Tunneling Microscopy", *J. Vac. Sci. Technol. B* **9**, 933 (1991).
- [181] J. A. Stroscio, D. T. Pierce, R. A. Dragoset, and P. N. First, "Microscopic Aspects of the Initial Growth of Metastable Fcc-Iron on Au(111)", *J. Vac. Sci. Technol. A* **10**, 1981 (1992).
- [182] C. Tölkes, P. Zeppenfeld, M. A. Krzyzowski, R. David, and G. Comsa, "Preparation of well-ordered cobalt nanostructures on Au(111)", *Phys. Rev. B* **55**, 13932 (1997).
- [183] A. W. Stephenson, C. J. Baddeley, M. S. Tikhov, and R. M. Lambert, "Nucleation and growth of catalytically active Pd islands on Au(111)-22 \times $\sqrt{3}$ studied by scanning tunnelling microscopy", *Surf. Sci.* **398**, 172 (1998).

- [184] S. Strbac, O. M. Magnussen, and R. J. Behm, "Nanoscale pattern formation during electrodeposition: Ru on reconstructed Au(111)", *Phys. Rev. Lett.* **83**, 3246 (1999).
- [185] C. A. Lang, M. M. Dovek, J. Nogami, and C. F. Quate, "Au(111) Autoepitaxy Studied by Scanning Tunneling Microscopy", *Surf. Sci.* **224**, L947 (1989).
- [186] B. Fischer, J. V. Barth, A. Fricke, L. Nedelmann, and K. Kern, "Growth and surface alloying of Al on Au(111) at room temperature", *Surf. Sci.* **389**, 366 (1997).
- [187] A. Christensen, A. V. Ruban, P. Stoltze, K. W. Jacobsen, H. L. Skriver, J. K. Nørskov, and F. Besenbacher, "Phase diagrams for surface alloys", *Phys. Rev. B* **56**, 5822 (1997).
- [188] K. B. Lewis, S. T. Oyama, and G. A. Somorjai, "The Preparation and Reactivity of Thin, Ordered Films of Vanadium-Oxide on Au(111)", *Surf. Sci.* **233**, 75 (1990).
- [189] J. V. Barth, R. J. Behm, and G. Ertl, "Mesoscopic structural transformations of the Au(111) surface induced by alkali metal adsorption", *Surf. Sci.* **302**, L319 (1994).
- [190] J. V. Lauritsen, M. Nyberg, R. T. Vang, M. V. Bollinger, B. S. Clausen, H. T. e, K. W. Jacobsen, E. L. gsgaard, J. K. N. v, and F. Besenbacher, "Chemistry of one-dimensional metallic edge states in MoS₂ nanoclusters", *Nanotech.* **14**, 385 (2003).
- [191] J. Chevrier, L. Huang, P. Zeppenfeld, and G. Comsa, "Characterization by scanning tunneling microscopy of the oxygen induced restructuring of Au(111)", *Surf. Sci.* **355**, 1 (1996).
- [192] K. B. Lewis, S. T. Oyama, and G. A. Somorjai, "Tpd Studies of Vanadium-Oxide Films Deposited on Gold", *Appl. Surf. Sci.* **52**, 241 (1991).